DOPPLER CATHETER MEASUREMENTS OF BLOOD FLOW VELOCITY IN CORONARY ARTERIES

Raimes Moraes

A thesis submitted to the University of Leicester
for the degree of Doctor of Philosophy

Division of Medical Physics,
Faculty of Medicine,
University of Leicester.

1995

ProQuest LLC
789 East Eisenhower Parkway
P.O. Box 1346
Ann Arbor, MI 48106-1346


LEICESTER UNIVERSITY LIBRARY

INDEX

ABSTRACT

Most heart disease is related to the luminal narrowing of the arteries that supply blood to the heart tissues, the coronary arteries. Coronary arteriography (CA) is regarded as the most accurate method for detecting the presence and severity of coronary disease. Nevertheless, there are some limitations associated with CA. In order to obtain further information on the severity of the stenosis many investigations have been performed with the use of a complementary technique: the intravascular Doppler catheter. Despite its growing use, there are few reported investigations of the errors introduced into velocity estimates obtained using catheter tipped transducers. Velocity estimates are used to calculate parameters which are then correlated with the haemodynamic situation under investigation.

This dissertation reports theoretical and experimental investigations carried out to assess the limitations of the technique in obtaining accurate velocity estimates. It also describes a microcomputer based system developed to obtain velocity estimates from Doppler signals sampled from coronary arteries and calculate parameters currently discussed in the literature. To calculate these parameters two other waveforms are sampled and processed: electrocardiogram and pressure. Discussion on digital techniques regarding improvement of the velocity estimates and analysis of Doppler signals is presented. Examples of clinical data obtained with the system developed and calculated parameters are given. Limitations of this technique and clinical procedures based on it are also discussed.

ACKNOWLEDGEMENTS

My thanks to Prof. D. H. Evans for accepting me under his supervision and for advice throughout this work; Prof. D. DeBono for all his support to this project, discussions and collaboration in obtaining the patient data; Dr. K. Martin for his help in performing attenuation measurements; and the Conselho Nacional de Desenvolvimento Científico e Tecnológico (CNPq - Brazil) for financial support. Thanks also to Harry Hall who assisted me during the measurements carried out *in vivo* and *in vitro*.

I am grateful to Colin Tysoe and Nizametin Aydin for the lengthy discussions on digital signal processing techniques which constituted the basis of my learning during this period.

Many thanks to Lingke Fan, Fernando Schilindwein, Ronney Panerai, John Pelmore, Mike Dunn, Glen Bush, Stephen Bentley, and Abigail Thrush for their help in many different and important ways.

I would like to thank Colin Tysoe once more for the first revision of this manuscript and, together with Mahendra Patel, for their guidance into the mysteries of the English language and British culture (Sorry for being such a bad pupil).

STATEMENT OF ORIGINALITY

The work presented in this thesis is original and, unless otherwise stated in the text or by references, has been performed by myself. Some of the material in this thesis is contained in the publication "Effects of non-uniform insonation by catheter-tipped Doppler transducers on velocity estimation" by R. Moraes and D. H. Evans, which is in press with Ultrasound in Medicine and Biology. Further material is contained in other manuscripts submitted for publication.

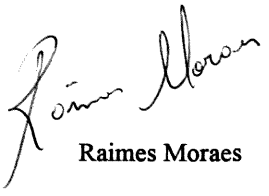

Raimes Moraes

Chapter 1 - Introduction

1.1 - Cardiovascular System and Coronary Disease

The cardiovascular system consists of a central organ, the heart, and a conduit net of different diameters named blood vessels. This system is responsible, via the blood and lymph for supplying nutrients to the body cells and transporting their metabolic waste products to the organs of excretion.

The blood vessels are classified into arteries and veins. Arteries convey blood from the heart to the organs. In general, veins transport blood back from the organs to the heart. These vessels have three layers: intima (innermost), media (intermediary) and adventitia (outermost). Fig. 1.1 depicts an overview of the arterial tree. The heart continuously pumps blood to itself and the other organs of the body through the vessels. The pumping function is vital for the organism. When the heart stops, the body collapses in seconds (Prives et al. 1985).

The heart is divided into four chambers (Fig 1.2). The two superior chambers are called atria and the inferior chambers, ventricles. There are valves between the atria and ventricles (admission valves) and also between the ventricles and output arteries (output valves). The contractile activity of the heart muscle and the opening and closure of the valves, controlled by pressure gradients, perform the pumping action. These events are further discussed in the next section. In the literature, the heart filling period is called diastole and the ejection period, systole. The ventricles are the chambers mainly responsibles for pumping blood around the lungs and systemic circulation. The heart wall also has three layers: endocardium (innermost), myocardium (intermediary) and epicardium (outermost). The myocardium is the thickest layer and is composed of muscular tissue (Burton 1977).

Heart disease is responsible for most deaths in Western countries. Most heart disease is related to the luminal narrowing of the arteries that supply blood to the

heart tissues themselves. These arteries are named coronaries. The disease is called atherosclerosis (Kannel and Thom 1986).

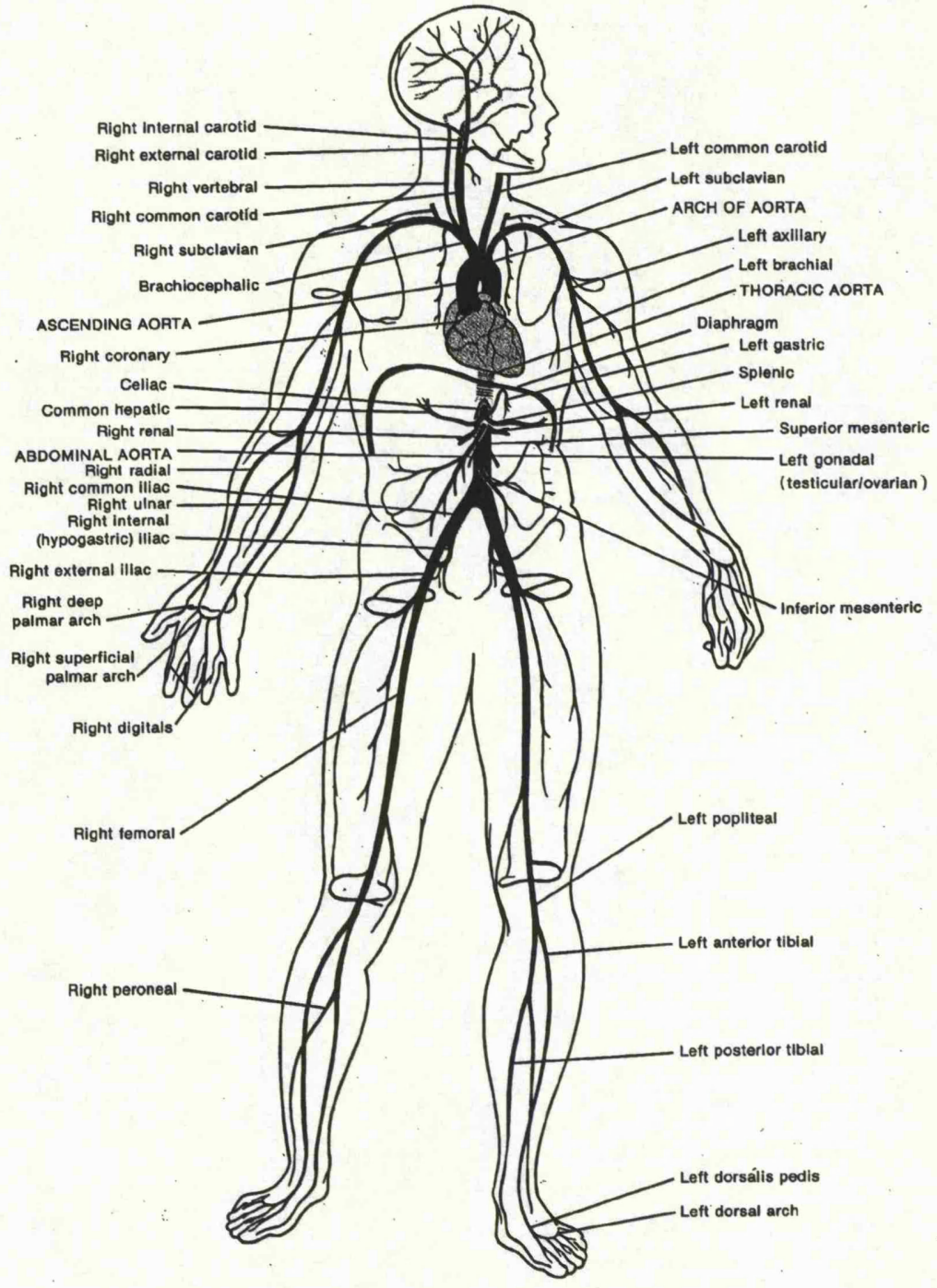

Fig. 1.1 - Diagrammatic representation of the major branches of the arterial tree (After Tortora and Anagnostakos 1990)

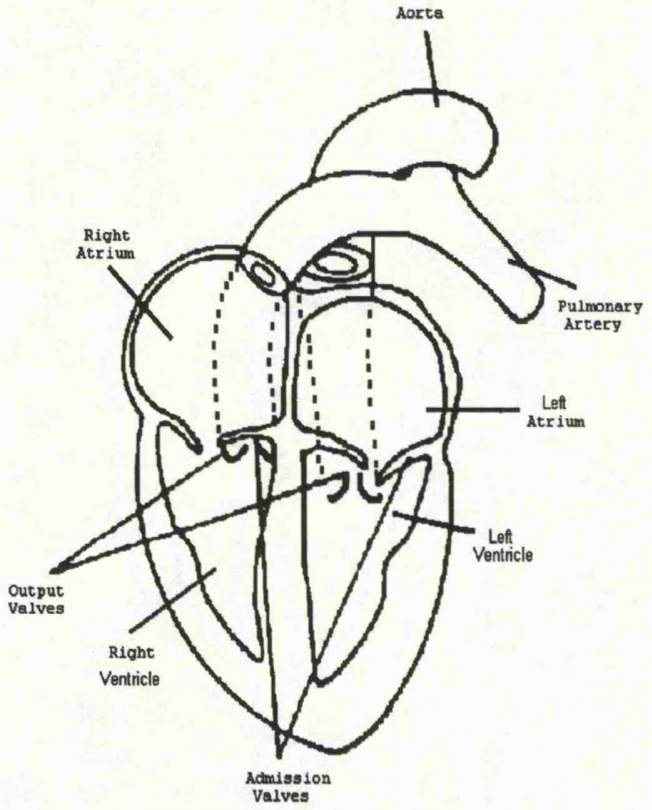

Fig. 1.2 - Outline of vertical section of the heart

The coronary arteries are medium-sized vessels (between 1.5 and 5.5 mm in diameter) which ramify from the aorta (the artery that arises from the left ventricle). They are termed right and left coronary arteries. The left one branches into two others shortly (2 to 10 mm) after its origin: the left anterior descending (LAD) and the left circumflex (LCX). The LAD supplies 40% of the heart, including the anterior wall of the left ventricle and about 2/3 of the tissue that divides the ventricles (interventricular septum). The LCX irrigates the left atrial wall and part of the left ventricle. The right coronary artery supplies the right ventricle, right atrium, part of the left ventricle and part of the interventricular septum. The right and left circumflex are linked to each other at the apex of the heart. Basically, they encircle the heart, branching into finer vessels that penetrates the myocardium. There are vascular channels called collaterals that link large coronary arteries to one another. They are small and few in number (Marcus 1983).

Atherosclerosis produces lesions that occur principally within the intima of the vessels. These lesions cause thickening of the arterial wall. If the lesion progresses sufficiently, it compromises the blood supply to the distal tissue. Atherosclerosis occurs more often in the aorta, femoral, popliteal, tibial, coronary, carotid and cerebral arteries (Bierman 1991).

For the coronaries arteries, a 75% lumen occlusion (50% of vessel diameter) will produce a deficient blood supply to a myocardial segment (myocardial ischemia) and can lead to a total interruption of the flow (myocardial infarction). The ischemia can stimulate the collateral vessels to develop into a major vascular network to provide an alternative way for the blood to irrigate the tissue distal to the lesion. The symptoms of ischemia are chest pain (angina pectoris), palpitations, breathing discomfort (acute dyspnoea) and exhaustion.

The common tests performed on patients to diagnose myocardial ischemia are physical examination, resting ECG and chest X-rays. More specific examinations may be necessary. They are: exercise ECG, long-term monitoring ECG, enzyme studies, radio nuclide imaging and arteriography (for a discussion of these methods refer to Hurst et al. 1986).

Coronary arteriography (CA) is regarded as the most accurate method for detecting the presence and severity of coronary disease. CA is indicated for patients with unexplained chest pain and whose noninvasive examinations do not exclude the possibility of coronary stenosis, or for asymptomatic patients showing exercise responses compatible with severe coronary disease (Steingart and Scheuer 1986).

The CA is obtained by inserting a catheter through the femoral artery and descending aorta up to the coronary arteries. Contrast medium is injected through the catheter and its flow behaviour is registered using a cineangiography technique.

This method produces an anatomical view of the vascular bed close to the catheter (Franch et al. 1986).

There are some limitations associated with CA. The interpretation of CA results is largely subjective. There is intraobserver and interobserver variability in judging the severity of the lesions. When atherosclerotic plaquing is diffuse, underestimation of stenosis occurs since the clinician assesses the stenosis severity by comparing its diameter with the diameter of an adjacent vessel that is assumed to be normal (Arnett el al. 1979; Wilson 1991). On the other hand, overestimation may result if spontaneous or catheter induced spasm occurs in the obstructed segment, increasing its narrowing. Since the results of CA are two dimensional images, eccentricity and asymmetry of the lesions adds difficulties to their interpretation. Overlapping vessels may also introduce errors (Marcus 1983).

The CA results are important to determine the extent of the disease and, if necessary, the surgical approach: bypass or percutaneous transluminal coronary angioplasty (PTCA). Bypass surgery uses an autogenous vein or artery to connect the aorta with the distal portion of the narrowed or occluded coronary arteries in order to re-establish the downstream blood supply. The most used graft is the reversed saphenous vein from the calf. The internal mammary artery has also been successfully used as an alternative to the saphenous vein. PTCA aims to increase the blood supply distal to the stenosis by increasing the diameter of the lumem. This is achieved by compressing the stenosis towards the vessel wall with the use of a distensible balloon in the tip of a catheter. PTCA is indicated for isolated, discrete, single-vessel stenoses (Hall and Gruentzig 1986; Jones and Hatcher 1986).

In order to obtain further information on the severity of the stenosis, assess the outcome of surgical intervention, and study the coronary circulation, many investigations have been carried out with the use of a complementary technique: the

Doppler ultrasound catheter. The following sections discuss the coronary circulation and the Doppler catheter technique.

1.2 - Coronary Circulation

The coronary circulation has a phasic pattern dictated by the balance between the driving pressure at the aortic root and the vascular impedance of the distal bed. To better understand this phasic behaviour, the temporal relationship between the aortic pressure, left ventricle pressure and the events of the heart pumping action are first discussed (Fig. 1.3). Fig. 1.4 presents the dependence of the coronary blood flow on aortic pressure.

After the filling of the ventricle (admission valve open, output valve closed), the ventricle wall starts contracting and the ventricular pressure rises. When the ventricular pressure increases above the atrial pressure the admission valve closes. The ventricular pressure continues increasing and when it exceeds the aortic pressure, the output valve opens and the blood is ejected into the aortic root increasing the pressure at that site. The contraction reaches its maximum and a period of muscle relaxation occurs. The ventricular and aortic pressures decay. The ventricular pressure falls faster than the aortic one and when the first becomes lower than the second, the output valve closes. A new filling period starts when the admission valve opens at a ventricular pressure below the one in the atrium (Burton 1977).

When the heart wall contracts, the coronary vessels are compressed, and the mechanical input impedance increases. From Fig. 1.4 it is possible to note that during diastole, when the heart muscles are relaxed, the coronary blood flow is driven by the aortic pressure. During systole, coronary flow starts to rise due to the

growing pressure in the aortic root, but falls again as the distal impedance increases. Therefore, the majority of coronary flow occurs during diastole.

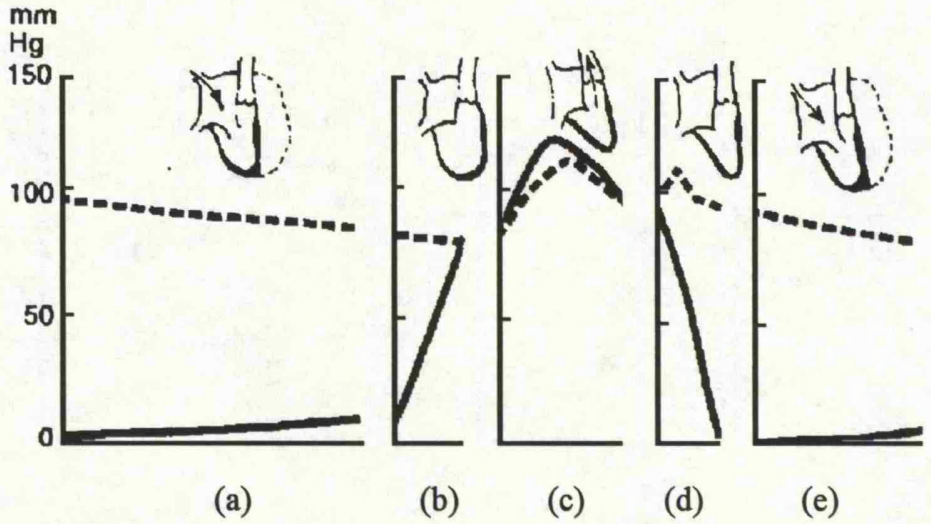

Fig. 1.3 - Temporal relation among phases of heart action, left ventricular pressure (continuous line) and aortic pressure (broken line). (b) and (c) correspond to systole. (a), (d) and (e) occur during diastole. (a) and (e) filling period (admission valve open, output valve closed). (b) isovolumetric contraction period (both valves closed). (c) ejection period (output valve open, admission valve closed). (d) isovolumetric relaxation period (both valves closed). (Modified from Burton 1977).

An interesting aspect of the coronary circulation is that an increase in the aortic mean pressure does not always produce higher flow. Experimental results show that an abrupt increase in perfusion pressure is followed by a rise in flow that, after some while, returns to its previous value. Therefore, the coronary circulation has some degree of autoregulation to adapt to different body operating conditions. This autoregulation is associated with myocardial metabolism, neural and humoral control (Factor and Bach 1994).

To assess the microcirculation autoregulation when stenosis is present in major coronary branches, Gould et al. (1974) performed experiments in dogs. LCXs of 12 animals were isolated and an electromagnetic flowmeter was implanted. Occlusion was produced distal to the transducer by a snare having its diameter controlled by a micromanipulator. The occlusion was successively increased under normal

circulation and under hyperaemia produced by vasodilator injection. Fig. 1.5 presents a typical result obtained from these experiments.

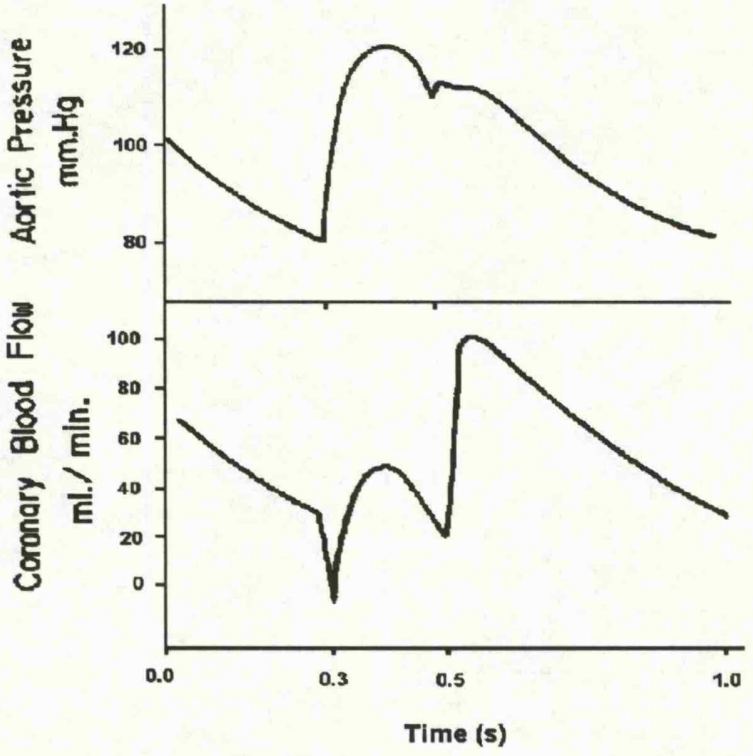

Fig. 1.4 - Temporal relation between aortic pressure and coronary blood flow. The diastolic flow is higher than the systolic one because of compression of arteries during heart contraction.

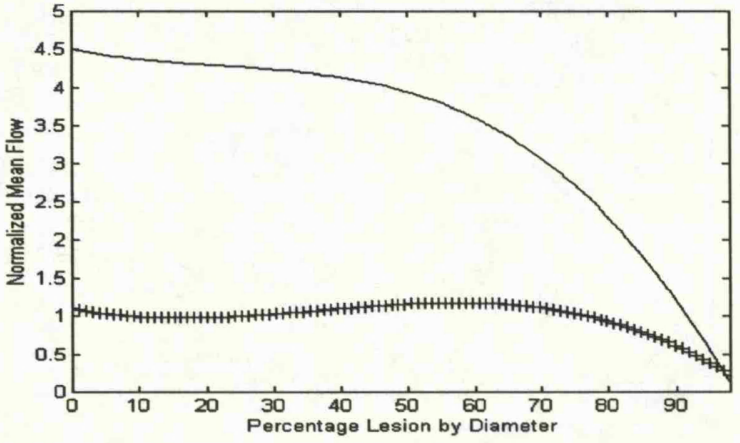

Fig. 1.5 - Effect of progressive constriction on the mean flow in LCXs of a dog at resting (+++) and at hyperaemia produced by vasodilator injection (——). Curves plotted from polynomials derived by Gould et al. (1974) to fit the experimental points.

Resting mean flow did not decrease up to an occlusion of 85% of the vessel diameter. Hyperaemic response changed more significantly after 45% of diameter constriction. The mean hyperaemic flow was four times higher than the basal one in the absence of stenoses.

This study also discussed phasic changes in the downstream flow caused by the presence of stenosis in the coronary arteries. It was observed that there is a marked reduction in diastolic flow without changes in systolic flow. This may be explained by the increased influence of the stenosis on flow during periods of low vascular resistance (diastole) as compared with that during periods of high distal vascular resistance (systole).

Kajiya et al. (1986) have shown similar phasic changes for man during cardiac surgery.

1.3 - Doppler Catheter Technique

Doppler catheters are devices that have an ultrasound transducer in their tips which allow measurements of blood flow velocity to be made inside the artery. The catheter is inserted into a coronary artery in the same way as one for arteriography. Doppler catheters have been used to evaluate the collateral circulation (Kern et al. 1993) and to quantify the severity of stenoses.

The methods developed to assess stenoses are the measurements of the coronary blood flow reserve ratio (CBFRR), diastolic/systolic velocity ratio (DSVR) and application of the continuity equation.

1.3.1 - Coronary Blood Flow Reserve Ratio

CBFRR is calculated by dividing the flow velocity measured in a hyperaemic condition by that measured in a normal perfusion state.

To produce hyperaemia, a vasodilator such as papavarine or adenosine is injected into the coronary artery. The recorded flow is considered to be the maximal one for that vascular bed.

The calculation of CBFRR is motivated by the fact that the coronary circulation has to adapt itself to different metabolic requirements of the heart. When the heart muscles require more oxygen, microvascular vasodilatation occurs to allow a higher blood perfusion. At rest, the flow is much lower than during hyperaemia. If there is a stenosis present in the vessel, there will also be vasodilatation of the vascular bed in order to allow normal blood supply to the tissue. Therefore, the CBFRR measures the capacity of the coronary system to increase the flow for a higher cardiac metabolism. If this value is small when compared with reference values obtained from healthy people, then the patient is likely to have a stenosis.

It should be noted that these assumptions are true if the vasodilatation capacity of the vascular bed distal to the stenosis responds normally to applied drugs. Since patients with history of infarction or hypertension have their microcirculation affected, CBFRR is not useful for these cases (Wilson et al. 1987). On the other hand, Wilson (1991) suggested that CBFRR can be used to detect microvascular dysfunction in patients with chest pain and normal coronary arteries.

Experimental work has show that a heart rate (HR) increase produces a flow increase in the basal condition, but the hyperaemic blood flow does not change significantly. Therefore, there is a CBFRR decrease with a HR increase (McGinn et

al. 1989; Rossen and Winniford 1993; Hongo et al. 1994). Since this precludes the comparison of results amongst different patients, McGinn et al. (1989) suggested the use of atrial pacing to perform measurements at a constant heart rate.

Wilson et al. (1987) have shown a good correlation between stenosis size and CBFRR.

1.3.2 - Diastolic/Systolic Velocity Ratio (DSVR)

Measurements of CBFRR taken immediately after angioplasty do not correlate well with the results achieved by intervention. The CBFRR may be depressed after a successful angioplasty. These findings are attributed, amongst other factors, to vasomotor tone alteration (due to angioplasty injuries of the vessel media or vasoconstrictor substances released by the tissue at the region of mechanical dilation), autoregulation malfunction related to long-term ischaemia and simultaneous increase of baseline and hyperaemic flow (Wilson et al. 1988; Segal et al. 1992).

Based on the phasic flow changes distal to the stenosis (Section 1.2), Segal et al. (1992) investigated the possibility of quantifying this behaviour by calculating distal DSVR measured before and after angioplasty (Folts at al. (1975) had previously suggested this parameter to evaluate graft surgery). According to their measurements, the distal DSVR correlated well with the outcome of angioplasty.

1.3.3 - Continuity Equation

Based on the mass conservation law, Johnson et al. (1989) proposed that an estimate of stenosis severity could be made by knowing that the flow is constant along a nonbranching tube. By measuring the velocity, area proximal to the stenosis, and the velocity in the stenotic region, determination of the stenosis area could be achieved. They developed experiments in animals obtaining good correlation between their measurements and the area of implanted stenosis.

Nakatani et al. (1992) applied this same principle in humans. To perform the velocity measurements the catheter was placed close to the stenosis and the velocity was registered at two different distances from the tip, corresponding to the pre-stenotic and stenotic region. The luminal diameters of the two segments were measured with fivefold magnified angiograms taken at the end of diastole. The authors claimed to have achieved good results when comparing the calculated and the measured stenoses diameters.

1.4 - Sources of Error in Doppler Catheter Measurements

This section discusses some aspects related to the difficulties of performing accurate blood flow velocity measurements in coronary arteries when applying the Doppler catheter technique.

Coronary arteries may be seen as branching and curved tubes. Both curves and bifurcations induce deviations from axismmetric flow. In curves, centrifugal force is strongest for the fluid elements travelling at higher velocities. This generates secondary motions, that is, faster moving fluid, originally at the centre of the vessel (for a parabolic velocity profile), will tend to be swept out towards the outside of the bend, being replaced by slower moving fluid from near walls (Fig. 1.6.a). In a bifurcation, inertial effects skew the velocity profile such that the fast moving

elements are found on the flow divider walls of the daughter vessels (Fig. 1.6.b). In consequence of this, secondary motions may also occur close to bifurcations. The pulsatile flow regime, the periodic compression of the vessel walls by the heart muscles and the presence of stenosis in the vessel add more complexity to the flow pattern developed in coronary arteries.

Considering this, the most obvious problem in performing velocity measurements with the Doppler technique is that the insertion of the catheter inside the vessel will disturb this complex blood flow pattern whose velocity is to be determined. The presence of the catheter may change the gross flow, modify the flow velocity distribution inside the vessel, and cause local turbulence introducing, therefore, errors into velocity estimates.

Movements of the artery wall and the pulsatile blood flow may change the position of the catheter inside the vessel during the cardiac cycle. Velocity estimates depend on the angle of ultrasound insonation (Eq. 2.1 - next chapter), on the degree of vessel insonation (uniform or partial) and on the position of the sample volume inside the vessel (Evans 1982; Law et al. 1991). Therefore, catheter displacements within the vessel may contribute to errors in velocity estimates.

Insonation of the artery wall by the sample volume generates artefacts which affect velocity estimates ('wall thump' - Evans et al. 1989). The introduction of filtering allows the elimination of these artefacts but it will also filter out frequency components of the real signal, adding errors to the velocity estimates.

Another difficulty is that these systems generate Doppler shift frequencies that are often too high to be simply recorded or processed by the majority of Doppler analysers. Therefore, a Doppler analyser utilised for this purpose should have some particular processing features in order to allow studies of the coronary circulation.

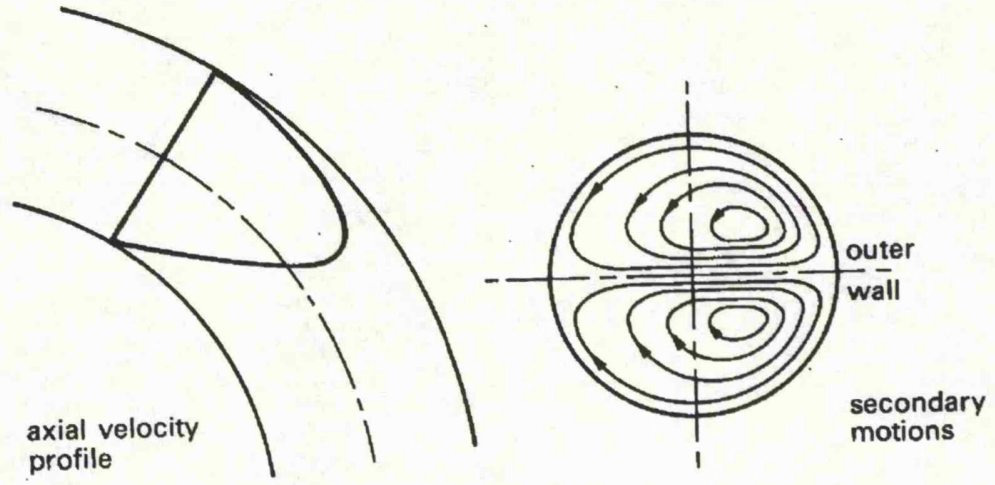

(a)

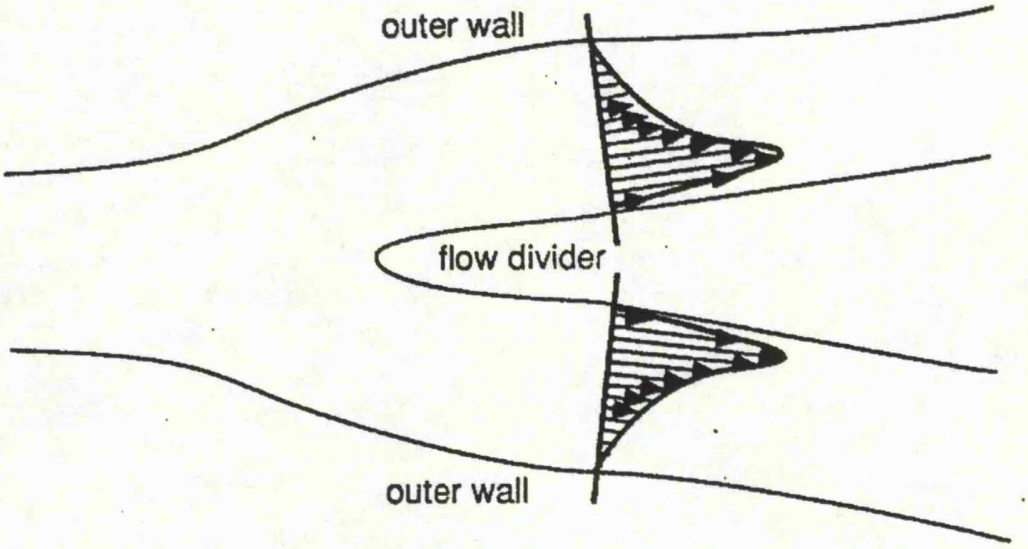

(b)

Fig. 1.6 - (a) This diagram illustrates the development of secondary motions in the flow due to vessel curvature (After Caro et al. 1978) and (b) distortion of flow profiles in a bifurcation which can also originate secondary motions (After Smedby 1992).

In spite of all these problems, Doppler catheters have been widely used to research parameters to quantify the severity of stenosis and to study the coronary circulation as mentioned in the previous section. It is our purpose in this work to address some of these aspects in order to get some insight on the potentialities of Doppler

catheters as clinical tools. For this, some measurements were performed with a Doppler catheter *in vitro*. The next section describes some of the techniques currently used to investigate *in vitro* the behaviour of blood flow in arteries and introduces the approach taken in this work.

1.5 - Techniques for Characterisation of Blood Flow in Arteries

Due to the complex interaction between the circulating blood and the arterial bed, added to the difficulties in performing measurements and observations *in vivo*, researchers have been investigating, for many years, numerical and experimental models in order to better understand various aspects of the circulation.

The use of models allows, for instance, the development of diagnostic techniques (Law et al. 1991; Keegan et al. 1994), and the study of atherogenesis (Perktold and Resch 1990).

An ideal model should take into consideration the rheological properties of the blood, the distensibility of the artery wall, the dimensions of the studied arterial segment and the pulsatile pattern of velocity waveforms present in it. Simplifications are usually adopted according to the approach chosen.

Since flowing blood develops secondary motions, numerical approaches should provide 3-D solutions for pulsatile flow in order to fully characterise the events in the real circulation. Such tools have been developed using finite element discretisation of the Navier-Stokes equations (Perktold et al. 1987; Dvinsky and Ojha 1994). In numerical approaches, the blood is usually considered to be a Newtonian fluid and the vessels are assumed to be rigid. The main difficulty with numerical modelling is the computational power required. For instance, Dvinsky

and Ojha (1994) have reported the limitations of a Sun Sparcstation 1+ with 40 Mbytes of memory, suggesting the use of a network of workstations to solve complex haemodynamic problems. Furthermore, numerical techniques to fully characterise blood flow in arteries are still subject to research. Numerical approaches should become more popular in the future when software and more powerful computers become more accessible, since they may provide more detailed information than experimental measurements (Dvinsky and Ojha 1994). Nevertheless, in spite of the fact that numerical solutions may give more information on the flow regime studied, one would wish to validate these results by comparing them with experimental measurements. Therefore, experimental techniques should be developed in parallel to developments of numerical methods.

Among experimental approaches to characterise pulsatile flow profiles in arterial models, two of the most powerful techniques are the laser Doppler velocimeter method (LDVM) and the photochromic tracer method (PTM). In these approaches, arterial models are usually scaled up to make the experiments easier and more accurate. Through the model, fluid with mechanical characteristics similar to blood is pumped. In order to reproduce waveforms similar to those present in the circulation, pulsatile waveforms are obtained by computer control of the pump driving the fluid (Ku et al. 1985; Law et al. 1987).

LDVs have a very small sample volume (length = 540 μm; diameter = 40 μm - Smedby 1992) enabling the investigation of flow profiles developed in a model by performing consecutive measurements of flow velocity in a specified radial position of the model studied during a cycle. By repeating these measurements for different radial positions, the flow profile can be determined (Ku et al. 1985; Denardo et al. 1994). This method requires a transparent arterial model and a transparent blood analogue. Computers are usually employed to depict the resulting temporal development of the flow profiles in the investigated section of the model. These flow profiles consist of 2-D representations of measured mean velocities.

Measurements in distensible models with non-Newtonian circulating fluids have been reported (Liepsch and Moravec 1984).

The PTM uses a colourless solution as a blood analogue which, when irradiated with ultra-violet light, undergoes a photochemical reaction producing a colour change. By irradiating a narrow section of the solution, perpendicular to the flow direction, and photographing the studied model at a selected time after the irradiation, the velocity profile can be visualised. Ojha et al. (1990) used this technique to visualise pulsatile flow profiles close to a modelled arterial stenoses. The ultra-violet light was generated by a pulsed N_2 laser and a set of seven convexes lenses was used to focus the laser beam at different points of the model in order to obtain a register of the spatial development of the flow profile in a same photograph. The solution used consisted of 1,3,3-trimethylindoline-6-nitrobenzospiropyran dissolved in deodorised kerosene. To compute parameters of interest in Doppler studies, such as the intensity weighted mean velocity produced by the observed flow profile insonated by an ultrasound beam with a known power distribution, the photographs obtained would need to be digitised.

The techniques described above are very powerful tools that enable the characterisation of pulsatile blood flow in arteries in similar conditions to those present in the real circulation. They would be very useful for characterising the flow profiles developed close to the Doppler catheter tip, from where the velocity measurements are taken. This would help to better evaluate the accuracy of the investigated Doppler measurements. Nevertheless, the cost involved and time necessary to build such set ups were limiting factors in this work.

Our aim in this project was to carry out some initial observations related to aspects that can affect the accuracy of the Doppler system utilised. For this, measurements for known flow conditions were performed. The use of complex flow fields similar to those present in coronary circulation would introduce difficulties in the

interpretation of the results. Therefore, we have limited our *in vitro* studies mainly to steady flow regimes. A simple technique for visualisation of steady flow close to the Doppler catheter tip was utilised to observe if the catheter introduces turbulence into the flow. Details of the experiments are provided in Chapter 8. The following sections describe the objectives of this work and the content of each chapter.

1.6 - Objectives

The aim of this work was to investigate the viability of applying Doppler catheters in the study of coronary circulation. The first step was to develop a Doppler analyser which would present the necessary features for this particular application, including the possibility of acquiring other physiological signals to calculate the parameters discussed in Section 1.3. The system developed was based on digital signal processing techniques. Some research on digital processing methods to improve the analysis of Doppler signals was also performed. The second step was to characterise the sample volume generated by the catheter employed and assess the accuracy of the measurements performed *in vitro* with the catheter and the developed Doppler analyser. Based on these measurements, discussion on the methods to characterise the severity of stenosis is presented. The final step was to perform measurements *in vivo* to validate the use of the developed Doppler analyser in clinical situations.

1.7 - Description of Contents

Chapter 2: The origin of the physiological signals of interest in this work, principles of their acquisition and the characteristics of the equipment utilised for their acquisition are described.

Chapter 3: This chapter describes the hardware and software developed to acquire and process quadrature Doppler signals, ECG and pressure waveforms. Examples of data sampled and processed with the use of the developed system are presented.

Chapter 4: Digital techniques to reduce cross-talk when processing Doppler signals are presented. A method of characterising parameters for the suggested compensation structures is also given.

Chapter 5: A developed maximum frequency follower is compared to two others in order to evaluate its performance. The method is found to present a similar performance to the other two, having as an advantage the automatic detection of the maximum frequency without any intervention of the operator.

Chapter 6: This chapter reports analytical, experimental and numerical methods utilised to characterise the sample volume produced by the Doppler catheter investigated. Based on the experimental results for the beam shape and two arbitrary flow profiles, investigation of the effects of non-uniform insonation on velocity estimates is presented.

Chapter 7: The implementation of software for off-line analysis of Doppler signals is described. This software allows the processing of Doppler signals with the use of the complex FFT and two time-frequency distributions.

Chapter 8: This chapter reports results of observations and measurements performed *in vitro* with steady and pulsatile flow. Blood and a blood analogue were utilised to carry out these measurements.

Chapter 9: Measurements *in vivo* and additional software to process sampled waveforms are described. Examples of the acquired and processed waveforms are given.

Chapter 10: This chapter summarises the work developed and discusses clinical perspectives for the use of Doppler catheters.

Chapter 2 - Signal Acquisition: Principles and Characteristics of Equipment Utilised

2.1 - Introduction

To perform studies on blood flow velocity in the coronary circulation, assessing the phasic characteristics of the flow, three different waveforms are required: Doppler signals, the electrocardiogram (ECG), and pressure.

Next section will discuss how Doppler signals allow the estimation of the blood flow velocity. Information derived from the ECG and pressure waveforms are used to discriminate between the two phases of the cardiac cycle, systole and diastole. With these data, it is possible to determine the blood flow velocity during systole and diastole, and therefore, investigate all methods discussed in the previous chapter (CBFRR, DSVR and continuity equation).

In this chapter, the origins of these signals are outlined and the technical characteristics of the devices used for their acquisition in this work are described.

2.2 - Clinical Application of the Doppler Effect

The relative movement between a wave source and an observer produces an increase or decrease of the frequency detected by the observer when compared to the emitted one. This phenomena is called the Doppler effect and the frequency difference, the Doppler shift which can be expressed as (Atkinson and Woodcock 1982):

$$f_d = f_t - f_o = \frac{2}{c} f_t v \cos\theta \qquad (2.1)$$

where:
f_d = Doppler shift frequency,
f_t = transmitted frequency,
f_o = observed frequency,
v = relative velocity,
c = velocity of the sound in the medium,
θ = angle between the directions of wave propagation and observer movement.

This principle is applied in medicine to measure the blood flow velocity in arteries. For this, a device called a Doppler system is designed to transmit ultrasound waves and process signals originating from the interaction between the blood and incident waves. The Doppler system processes electrical signals, therefore, a transducer is necessary to convert electrical into acoustic energy and vice-versa.

The following discussion will present the basic ideas involved in this conversion, the interaction of ultrasound waves and the blood, and Doppler systems.

2.2.1 - Ultrasound Transducers

Transducers used by Doppler systems are built with piezoelectric crystals. Piezoelectric material, when mechanically strained, generates an electrical potential that is proportional to the applied force. Conversely, the application of an electrical field to the crystal produces dimensional changes in the material.

Under resonant operation, the piezoelectric crystal, excited by a continuous sinusoidal waveform or pulses of very narrow frequency spectrum, can be represented by a lumped-element circuit. This circuit is shown in Fig. 2.1 where L_m, C_m and R_m model a mechanical resonator (Redwood 1964).

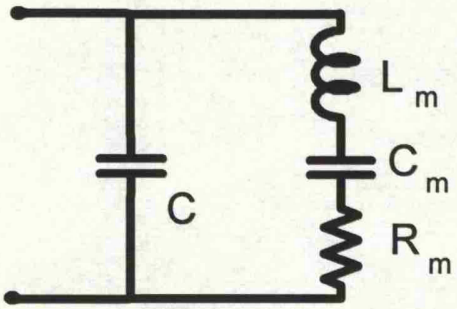

Fig. 2.1 - Lumped equivalent circuit of piezoelectric transducer valid at frequencies near resonance. C is the transducer capacitance. L_m ,C_m and R_m represent the mechanical system.

Under the application of an electrical pulse, the crystal vibrates. Its mechanical interaction with the surrounding medium produces acoustic waves that propagate into the tissue. Fig. 2.2 illustrates the relation between the electrical pulse and the resultant acoustic wave.

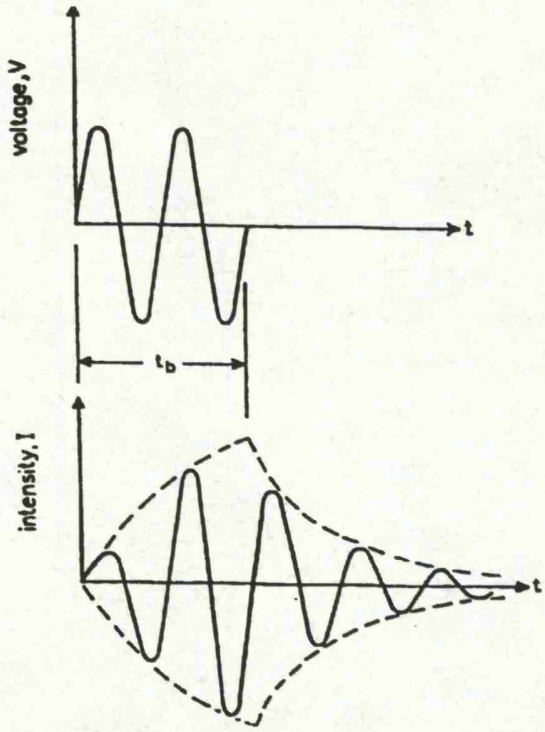

Fig. 2.2 - (b) Piezoelectric transducer response to (a) a short electrical pulse (After Jorgensen et al. 1973).

Fig. 2.1 aids the understanding of the events of Fig. 2.2. During step pulse application, the crystal stores energy and vibrates. When the pulse ceases, the crystal rings during the energy decay, increasing the length of the acoustic pulse. The beam pulse shown in Fig. 2.2 is usually called a 'teardrop' in the literature.

Therefore, the pulse shape produced by an ultrasound transducer depends on the characteristics of the electric pulse applied and the electromechanical properties of the crystal used. The most common piezoeletric elements used are made of ceramics, e.g. lead zirconate titanate, and plastics, e.g. polyvinylidene difluoride (Evans et al. 1989).

2.2.2 - Interaction of Blood and Ultrasound

Blood is a non homogenous medium consisting of plasma, erythrocytes (red blood cells), leukocytes (white blood cells) and platelets (small particles vital for the clotting process).

The plasma occupies about 54% of the total blood volume and is composed of water (90%), protein (7%) and other substances such as salt and glucose. The erythrocytes have a biconcave disc shape with an average diameter of 8.1 μm and an average volume of 95 μm^3, representing approximately 45% of the blood volume. They have a larger volume and are more numerous than the platelets (≈ 20:1). The red cells are also more numerous than the leukocytes (≈600:1 - Burton 1977).

When ultrasound waves are propagating in any inhomogeneous medium, they are attenuated by two mechanisms: absorption and deflection (reflection, refraction and scattering). Absorption converts acoustic energy into thermal energy. Scattering occurs when acoustic waves encounter obstacles that are much smaller than their

wavelength, being then partially deflected from their original course and re-radiated in all directions. For frequencies up to 15 MHz,. the majority of attenuation in blood is due to absorption alone since the scattered power by blood is very low (Shung et al. 1976). Fig. 2.3.a shows experimental measurements of attenuation for whole blood up to 10 MHz (Kikuchi et al. 1972 cited by Goss et al. 1978). Fig. 2.3.b displays the data shown in Fig. 2.3.a together with data obtained by Lockwood et al. (1991) for attenuation of blood between 30 and 57.5 MHz (44% haematocrit).

Experiments have shown that the erythrocytes are mainly responsible for the scattering (Reid et al. 1969) and that for frequencies up to 30 MHz, blood (6% haematocrit) scatters ultrasound waves with a power that is proportional to the fourth power of the incident frequency (Kuo and Shung 1994). Blood scattering is also dependent on blood flow rate since at low flow rates, blood forms red cell aggregates (Yuan and Shung 1989), and for high flow rates, turbulence seems to introduces changes in the red cells distribution (Shung et al. 1984). Lockwwod et al. (1991) have found that, for frequencies above 35 MHz, the frequency dependence of blood scattering is lower than that found by Shung et al. (1976) ranging between the power of 1.3 and 1.4. Fig. 2.4.a shows data obtained by Shung et al. (1976) on scattering for blood red cells suspended in saline at two different haematocrits (hmct): 8% and 26% (flow rate: 4 ml/s). Fig. 2.4.b shows data obtained by Lockwood et al. (1991) for blood scattering between 35 and 65 MHz (38% haematocrit). In Fig. 2.4.b, an experimental measurement performed by Shung et al. (1976) is also shown for comparison.

For the frequency of interest in this work, 20 MHz, blood scattering measured for porcine blood in saline (6% haematocrit) is approximately 19×10^{-4}/Sr.cm (Kuo and Shung 1994). From the data available (Fig. 2.3.b), the attenuation of the whole blood at this frequency should be between 5 and 9 dB/cm.

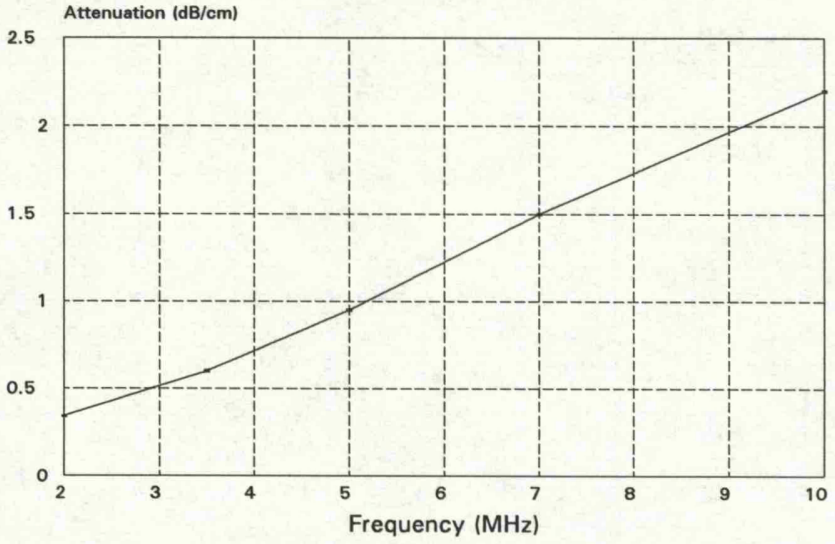

(a)

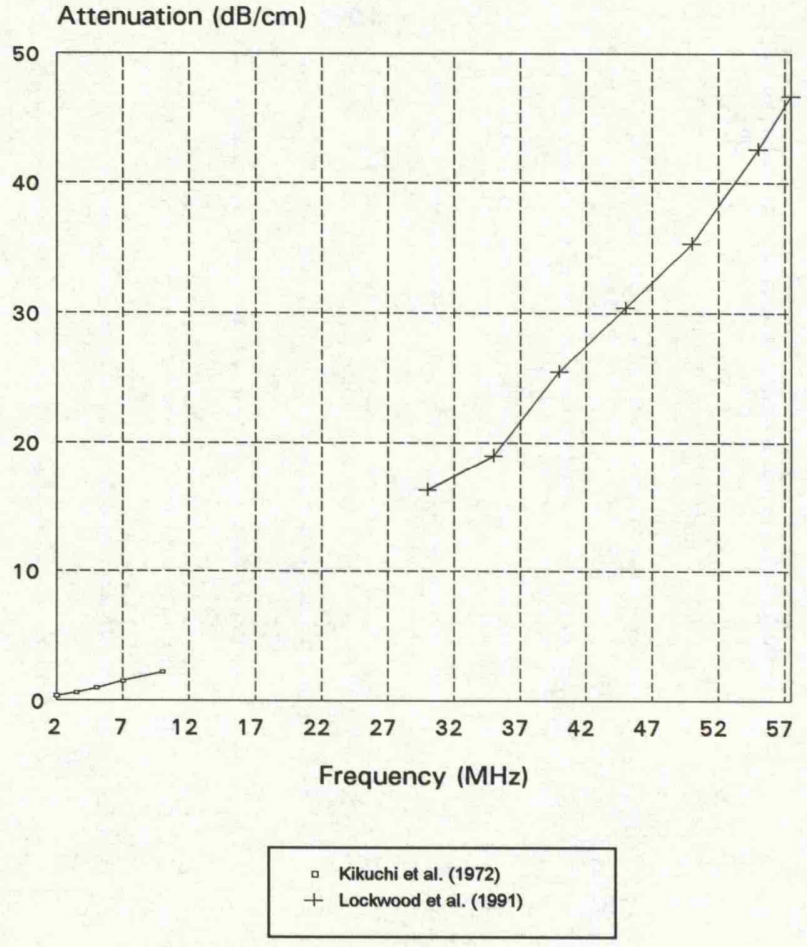

(b)

Fig. 2.3 - Experimental data on blood attenuation obtained by (a) Kikuchi et al. (1972) that are also plotted in (b) together with data obtained by Lockwood et al. (1991).

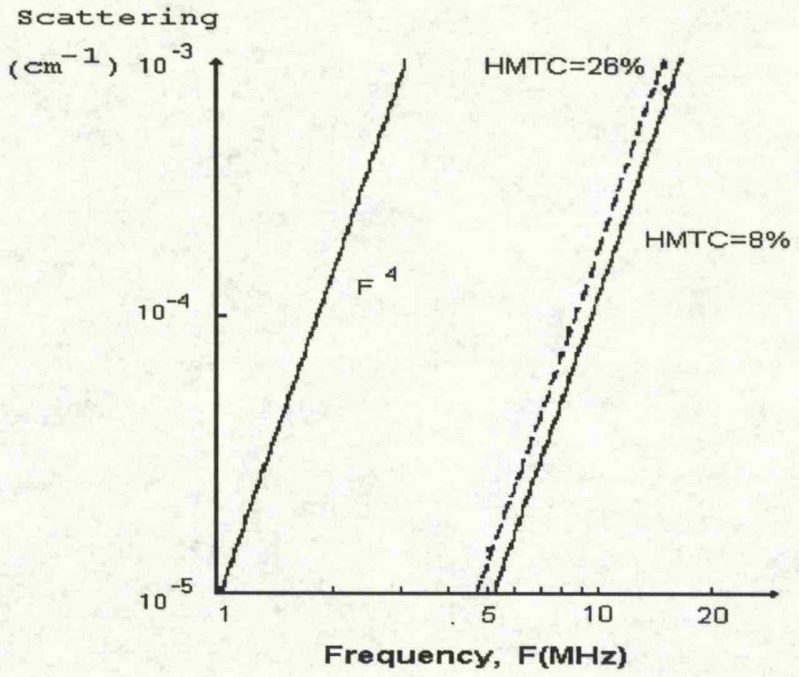

(a)

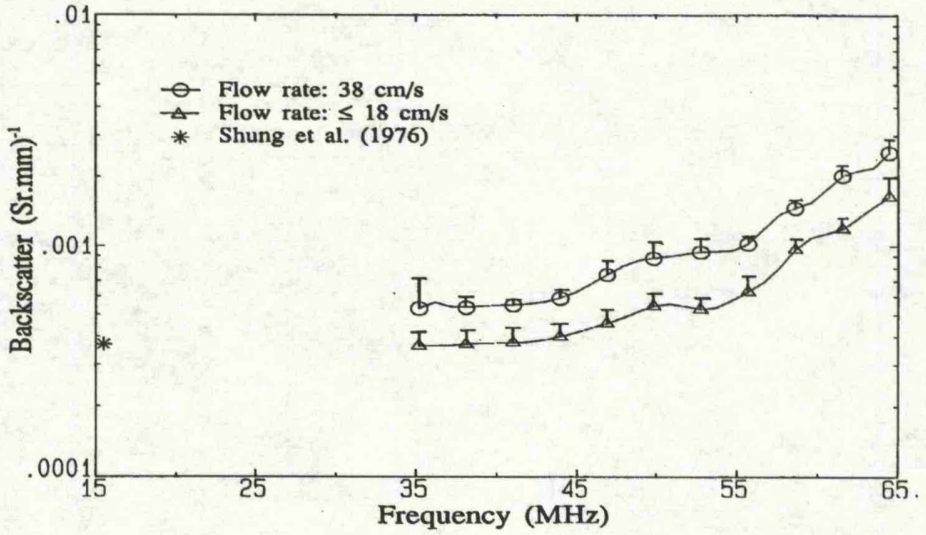

(b)

Fig. 2.4 - Experimental measurements of ultrasound scattering by blood reproduced from (a) Shung et al. (1976) and (b) Lockwood et al. (1991). The measurements by Shung et al. (1976) were carried out for two different haematocrits (hmct: 8% and 26%) at the flow rate of 4 ml/s. The fourth power of the frequency is plotted for comparison. The measurements performed by Lockwood et al. (1991) at flow velocities below 18 cm/s did not present much difference. Data obtained at the flow velocity of 38 cm/s is also shown. The standard deviation is presented for 5 measurements performed.

2.2.3 - Pulsed Doppler Systems

A block diagram of a pulsed Doppler system is depicted in Fig. 2.5. The master oscillator produces a sinusoidal signal at the resonant frequency of the transducer. This signal is modulated by a pulse repetition frequency (PRF) generator, producing a train of pulses that are amplified and applied to the transducer (Fig 2.6).

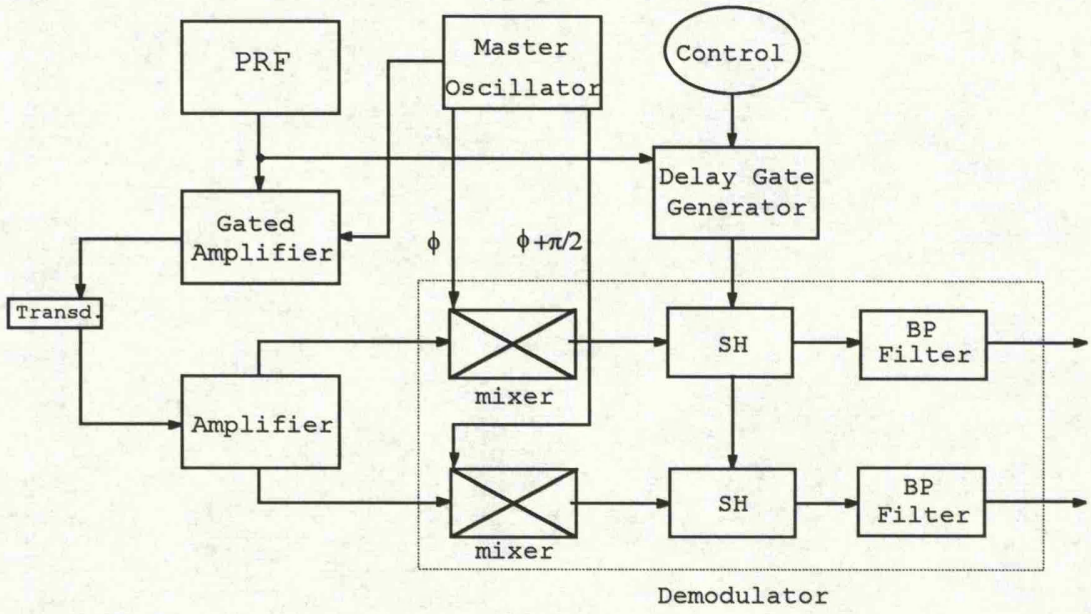

Fig. 2.5 - Block diagram of a pulsed Doppler system

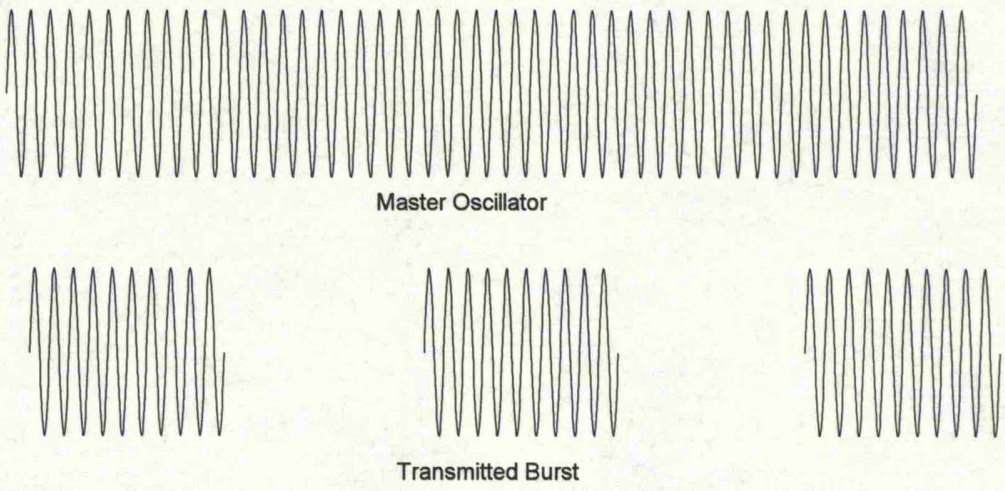

Fig. 2.6 - Modulated master signal that is applied to the transducer.

The signals scattered by the blood propagate back to the transducer where they are converted to electrical signals. These signals are amplified and demodulated. To discriminate among signals arising from different vessels or sections of a vessel, the demodulated signals are sampled for a short time interval, using sample and hold circuits (SH). The opening of this time window is established by a delay gate generator. This delay can be adjusted by the operator and can be calibrated in terms of distance, since the time between the pulse emission and echo reception is proportional to the distance between the transducer and the depth of the insonated region.

The sampled signals are then filtered by band-pass (BP) filters whose lower cut-off frequency is usually defined between 200-400 Hz in order to eliminate high amplitude and low frequency signals originating from the vessel wall movements ('wall thump'). The higher cut-off frequency is dictated by the Nyquist criteria. This limits the maximum Doppler frequency that can be discriminated without aliasing to half of the PRF.

The demodulator diagram presented by Fig. 2.5 depicts the so-called quadrature phase detector (QPD). This is the most widely used directional demodulator. Some other techniques have been discussed by Coghlan and Taylor (1976).

The QPD makes use of signals that are in-phase and 90° phase shifted with respect to the master oscillator. These are multiplied by the incoming signals to provide the demodulation. To illustrate this, let the incoming signal be represented by the sum of signals scattered by three different targets: one stationary, one moving away from the transducer and the other in the opposite direction. Due to the Doppler effect, this sum is given by:

$$r(t) = A_0 \cos(w_o t + \phi) + A_f \cos(w_o t + w_f t + \phi_f) + A_r \cos(w_o t - w_r t + \phi_r)$$

where:
w_o = carrier frequency
w_f = Doppler shift due to the target moving away from the transducer,
w_r = Doppler shift due to the target moving towards the transducer,
A = amplitude of the component specified by the index.

The multiplication of this equation by $\cos(w_o t)$ and $\cos(w_o t\text{-}90°)$ yields, after filtering out the DC and the components above half of the PRF frequency, respectively:

$$i(t) = \frac{A_f}{2}\cos(w_f t + \phi_f) + \frac{A_r}{2}\cos(w_r t - \phi_r) \qquad (2.2)$$

$$q(t) = \frac{-A_f}{2}\sin(w_f t + \phi_f) + \frac{A_r}{2}\sin(w_r t - \phi_r) \qquad (2.3)$$

After the processing described, the only components remaining are those related to forward and reverse velocities, since w_f and w_r are proportional to them.

Both signals described by Eqs. 2.2 and 2.3 contain information on forward and reverse flow. Further processing allows the separation of the directional components.

One of the techniques used for this separation is the phase domain processing illustrated in Fig. 2.7 (Coghlan and Taylor 1976).

A phase shift of 90° applied to the in-phase signal (Eq. 2.2) yields :

$$si(t) = \frac{A_f}{2}\cos(w_f t + \phi_f + 90°) + \frac{A_r}{2}\cos(w_r t - \phi_r + 90°) \qquad (2.4)$$

Summing Eq. 2.3 to Eq. 2.4, we have:

$$fw(t) = -A_f \sin(w_f t + \phi_f)$$

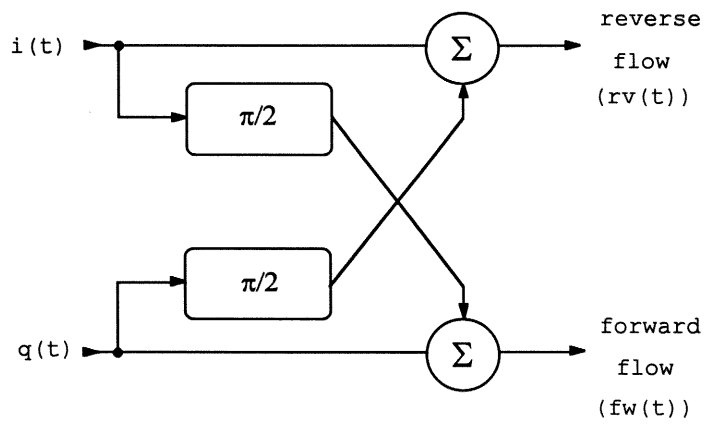

Fig. 2.7 - Directional separation of forward and reverse flow components by phase domain processing.

The addition of Eq. 2.3 phase shifted by 90° to Eq. 2.2 produces:

$$rv(t) = A_r \cos(w_r t - \phi_r)$$

Another technique to separate forward and reverse flow is discussed in the next chapter.

2.2.4 - Technical Specification of the Catheter Tipped Doppler Transducer and System

The Doppler catheters used during this project are produced by Schneider (Zurich, Autria). They consist of an annular piezoelectric crystal with outer and inner diameters of 0.8 mm and 0.5 mm respectively. The central lumen allows the catheter to be placed into the coronary arteries with the use of a guide wire.

The crystal is mounted on the tip of a 3F intracoronary catheter and two leads for the electrical connection are soldered to its surfaces, one to the top and another to the bottom. The transducer is then covered with a layer of epoxy resulting in a final outer diameter of 1 mm and a lumen of 0.4 mm.

The catheter is connected to a Doppler system produced by Millar Instruments (Houston, USA). The model is the MDV-20 velocimeter whose characteristics are show in Table 2.1.

Master Frequency	20 MHz
PRF	62.5 kHz
Pulse Width	0.4 μs
Variable Range Gate	1-10 mm
Output Filters Specifications	----------
Low Cut-Off Frequency	0.3 kHz
High Cut-Off Frequency	30 kHz

Table 2.1 - Characteristics of the Doppler system used

2.3 - Acquisition of Pressure

The pressure waveform depends on the volume and velocity of the ventricular blood ejection, the peripheral resistance to flow, the distensibility of the arterial wall and the blood viscosity (O'Rourke 1986). It also exhibits different shapes at different sites due to the transit time and wave reflections along the arterial tree (Nichols and O'Rourke 1990). The pressure waveform of the great arteries may also be used as a diagnostic tool (Franch et al. 1986).

The frequency content of the pressure signal extends from dc to 30 Hz, but the components above 20 Hz are not very significant (Nichols and O'Rourke 1990).

Considering the pressure waveform at the aorta root (Fig. 1.4), the beginning of the diastole can be identified by the dicrotic notch since it denotes the closure of the output valve between the left ventricle and aorta (aortic valve).

In this work, the pressure waveform is recorded by a catheter tipped transducer placed into the aortic root through the femoral artery. The following sections discuss the principles upon which the transducer is based, and the characteristics of the system used.

2.3.1 - Pressure Transducer

To understand the physical principles involved in the conversion of pressure to an electrical signal, consider the resistance of a metal wire that is given by:

$$R = \frac{\rho l}{A}$$

where:
ρ = resistivity of the material,
l = length,
A = cross sectional area.

If the wire is strained, the ratio of change in its resistance is (Peura and Webster 1978):

$$\frac{\Delta R}{R} = (1+2\mu)\frac{\Delta l}{l} + \frac{\Delta \rho}{\rho}$$

where μ = Poisson's ratio.

The first term of the right hand side is a function of the dimensional changes of the wire (dimensional effect) and the second term shows that the strain also affects the resistivity of the material (piezoresistive effect).

There are alloys and semiconductors that present a comparatively large alteration of their resistance under strain. These materials are used to produce transducers called strain gauges consisting of compacted wound wire, etched foil or vacuum-deposited film.

The measurement of their resistance is usually made with a Wheatstone-bridge circuit. Displacements of the order of a nanometer can be detected (Peura and Webster 1978).

The transducer used in this work is formed by a metal diaphragm where thin film strain gauges are deposited. The diaphragm is deformed by the blood pressure and the detected changes in their resistance are scaled in terms of the applied pressure.

The diaphragm is located on the side of the catheter to avoid artefacts in the measurements produced by the kinetic energy of the blood which may occur when the transducer is not at right angles to the flow (Cobbold 1974).

2.3.2 - Technical Aspects of the Pressure System Utilised

The catheter tipped pressure transducer used was produced by Gaeltec Ltd (Isle of Skye, Scotland). The diaphragm is housed in a surgical steel body mounted on a woven dacron catheter. The diameter of the transducer is 2 mm (6F). It has a sensitivity of 5 μV/mmHg and is linear for the range of 0-300 mmHg.

The amplifier unit utilised is also produced by Gaeltec Ltd (model S12). This device allows the user to control the gain, adjust the null point of the bridge circuit and provides an output signal whose frequency content ranges from DC to 1.4 kHz. This high frequency response allows the recording of the cardiovascular sounds related to different events of the pumping action, but they are not of interest in this work. The device also has a mean pressure output.

For this work the gain of the pressure unit was kept fixed. The relationship between the applied pressure and voltage output was measured for the catheters utilised. This allowed the setting of a proper scale for the pressure signals being displayed as described in the next chapter. It is advisable, nevertheless, to make periodic checks on the conversion of pressure to voltage, since performance may change with time, and also verify the scale for new catheters.

2.4 - Acquisition of ECG

The heart beat is an intrinsic action resulting from the interaction of the cardiac cells. The nervous system is only able to control its pace, for example, in response to the oxygen demands of the body. There are two kinds of heart cells: contractile and specialised. The former have periods of contraction that are triggered by electrical impulses. The cardiac cells, when stimulated, exchange ions with the extracellular medium producing a transmembrane potential that constitutes the electrical impulse. This impulse propagates along the cell membrane and is communicated to the neighbouring cells, spreading the contractile action through the heart wall.

The specialised cells are characterised by a faster conduction velocity of the electrical impulse. These cells form the conduction system that generates and

distributes the electrical impulses. This system is composed of the sino-atrial (SA) node, the atrioventricular (AV) node, bundles and the Purkinje network (Fig. 2.8).

The SA node is a pencil-tip-sized region located on the right atrium wall, close to the vena cava, composed of self-excitatory cells. These cells produce spontaneous and rhythmic ion changes through their membrane, generating electrical impulses that activate the heart beat. Therefore, the SA node acts as the cardiac pacemaker.

The impulses generated by the SA node travel along the atrial wall to arrive to the AV node located at the base of the atrial septum. This node ramifies into bundles at the interventricular septum. These bundles branch off further, eventually forming the Purkinje fibres that thread through the ventricles.

Due to the disposition of the conduction system, the electrical excitation, and therefore the contraction, spreads sequentially through the atria, interventricular septum and simultaneously through right and left ventricles. From the ends of the conduction system, the impulse propagates through the contractile cells. This activation pattern establishes a very well co-ordinated and efficient contraction of the heart.

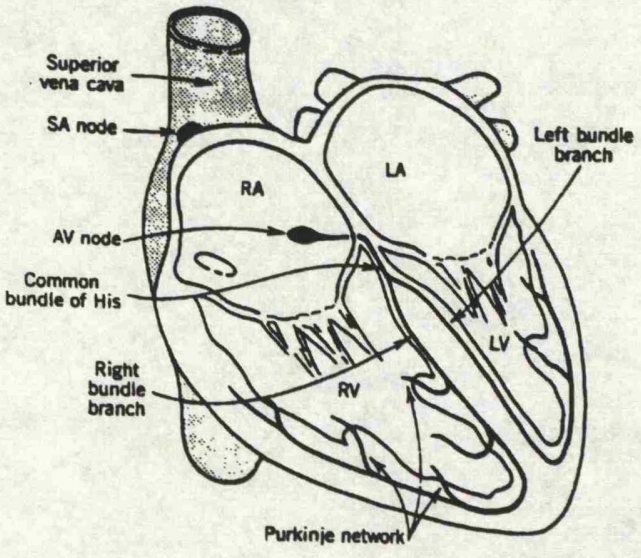

Fig. 2.8 - Structural diagram of the conduction system of the heart (After Webster 1988).

The electrical activity of the heart produces potentials that can be detected on the body surface with amplitudes that vary from 0.5 mv to 4 mv (Olson 1978). These potentials are detected by placing electrodes on the body and measuring the voltage difference between them. This signal is called the electrocardiogram (ECG).

The shape of the ECG waveform depends on the position of the electrodes on the body. Fig. 2.9 shown a typical and normal ECG obtained with electrodes located on the left leg, right arm and a third one on the right leg that is used as a reference (lead II). The first deflection, called the P wave, is associated with the atrial activation. The second feature of the ECG, the QRS complex, is related to the activation of the ventricles and the third deflection, the T wave, corresponds to the return of the ventricle cells to their resting state. Because of the temporal and spatial relation between electrical and muscle activities, the ECG is used as a tool to assess the heart functions. For instance, ischaemia modifies the T wave and the different morphologies that it assumes, are related to the location of the affected area of the heart (Orlov 1988).

The ECG is used in this work only to determine the beginning of systole since the QRS complex denotes ventricular excitation. It should be noted though, that mechanical contraction of the ventricle starts about 50 ms after the QRS complex (Milnor 1980).

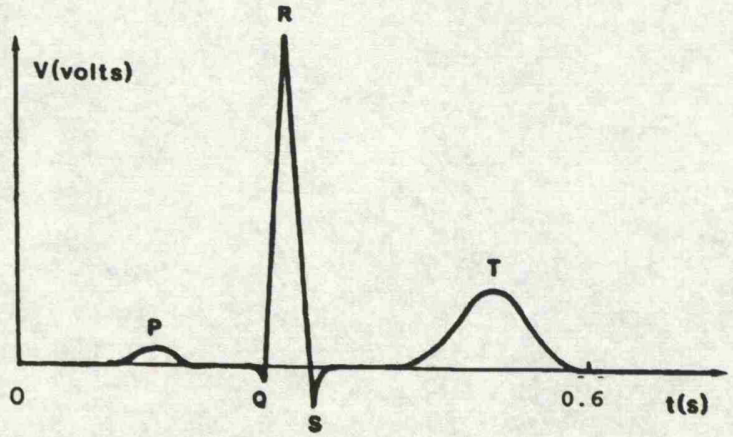

Fig. 2.9 - Typical ECG waveform obtained with the lead II and the conventional designation of its deflections.

The frequency content of the ECG is between 0.01 and 250 Hz, but devices for general diagnosis work within the range of 0.05-100 Hz and monitoring equipment, 0.5-50 Hz. The QRS complex that is used to detect the start of systole is usually processed in a range of 10-20 Hz (Webster 1988).

In this work, the ECG signals are acquired from systems used by medical staff to monitor the patient during catheterization. As different equipment is utilised in different catheter rooms, specific data are not given. Basically, an ECG amplifier has a differential configuration and includes an isolation circuit to protect the patient from dangerous currents that could be generated in the equipment. The ECG amplifier also has devices to protect the equipment from high voltages that may appear between the electrodes due to defibrillator discharges (Neuman 1978).

2.5 - Summary

This chapter has introduced the principles of acquisition of Doppler signals, ECG and pressure waveforms. The concepts and terminology presented, and the characteristics of the equipment described are refered in the remaining of this text.

Chapter 3 - Description of the System Developed to Process Doppler, ECG and Pressure Signals

3.1 - Introduction

The system developed to sample and process the data provided by the devices discussed in the previous chapter is based on an IBM compatible 486 PC. Into this, a digital signal processing (DSP) board and an analog-to-digital (A/D) conversion board are inserted.

The DSP board is produced by Loughborough Sound Images Ltd. (Loughborough, UK) and has a DSP processor, 160 kbytes of memory, a timer and two A/D channels containing fourth order lowpass Butterworth filters and A/D converters. The cut-off frequency of the Butterworth filters are programmable with the use of external components.

The DSP processor is the WE DSP32C manufactured by AT&T. This contains a 32 bit floating point arithmetic units, 6 kbytes of internal memory, direct memory access facilities (DMA [1]) and can perform up to 12.5 million instructions per second.

The A/D converters of the DSP board are 16-bit precision, working in a range of ± 2.5V. They are utilised to acquire the ECG and pressure signals. To sample the Doppler signals, an A/D conversion board was developed. Section 3.2 discusses the technical requirements for this board, and its design is described in Section 3.3. The A/D board is interfaced to the DSP board and the PC.

Section 3.4 describes the software developed to carry out the sampling and processing of the signals.

[1]Data transfer from and to the memory without necessity of program intervention.

The application of the system described in the following sections for the acquisition of clinical data is reported in Chapter 9.

3.2 - Technical Requirements for the A/D Board

There is clinical interest in recording and measuring blood flow velocity in stenotic coronary vessels before and after angioplasty.

Before angioplasty, the flow velocity is usually low since the stenosis hampers the flow depending on its severity. It has also been observed that, after angioplasty, the flow velocity is higher than that expected in a resting condition. This finding is attributed to the inability of the distal vasculature to autoregulate immediately after long term abnormal flow perfusion (Wilson et al. 1988). Consequently, the flow velocity changes dramatically between these two haemodynamic situations.

According to the Nyquist sampling theorem, a signal should be sampled at a rate at least twice that of its maximum frequency component to have its frequency spectrum preserved (Carlson 1986).

The use of a constant sampling rate, high enough to properly sample the Doppler signals during hyperaemic flow post-angioplasty, would produce a poor frequency resolution for the data obtained before the intervention (if the same data length is processed, as discussed later on). Beyond this, the flow velocity is also variable among the population. Therefore, it is desirable to be able to sample the Doppler signals at different rates.

To meet the Nyquist criteria, low pass filters, called anti-aliasing filters, are used to limit the frequency content of the signal (and noise) to half of the sampling

frequency. Since we are interested in sampling Doppler signals at different rates, they need to be programmable.

Another important requirement, as mentioned in Chapter 2, is to filter out the artefacts due to the wall movements ('wall thump'). 'Wall thump' filters are included in the Doppler system used. However, during our clinical measurements it was realised that they were not able to eliminate satisfactorily the artefacts because their cut-off frequency (300 Hz) were lower than the frequency content of the 'wall thump'. As their presence depend on the anatomical site and position of the catheter within the vessel, programmable 'wall thump' filters were incorporated in the A/D board designed.

3.3 - Description of the Implemented A/D Conversion Board

Fig. 3.1, 3.2 and 3.3 depict the circuit implemented to carry out the sampling of the quadrature Doppler signals. It has the following characteristics: programmable amplifiers, programmable 'wall thump' filters, programmable anti-aliasing filters, programmable sampling rates, simultaneous sampling of the quadrature signals and direct interface to the DSP processor.

The analog inputs of the circuit are voltage clipped to 4.0 V by Zener diodes. This avoids damage to the components connected to the inputs if a high voltage is accidentally applied to them.

The input signals may be amplified up to 24 dB by the programmable amplifiers SC11310 (Sierra Semiconductor Ltd.). These integrated circuits (IC) are controlled by a binary word that selects the gain in steps of 0.1 dB. This word is sent by software running in the PC, according to the operator settings established during

the use of the system. The PC selects the SC11310, as other IC's on the board, through an address decoder consisting of the IC's 74LS688 and 74LS139. Amplification of the input signals allows the A/D converters to achieve a better performance in terms of digital resolution for signals of different amplitudes (obtained from different patients and clinical situations) and gives flexibility for the system to be used with various Doppler systems that may present different gains in their quadrature outputs.

The 'wall thump' filters are Butterworth of second order implemented using state-variable active filter IC's produced by Burr-Brown (UAF42). The cut-off frequencies of these high pass filters (one for each channel) are simultaneously changed using a quad digital to analog converter (D/A - MP7628) and 4 auxiliary operational amplifiers, two of them being contained in the UAF42 IC's. By writing digital words to the D/A's through the PC, it is possible to program the cut-off frequencies of the 'wall thump' filters between 300 to 6375 Hz in steps of 25 Hz.

The IC's used for anti-aliasing filtering are integrated 8th order elliptic filters made by Linear Technology (LTC 1064-4). They operate up to a maximum cut-off frequency of 100 kHz. The cut-off frequencies are determined by 1/50 of the frequency of a clock applied to pin 11 of each device. The clock is generated by a programmable interval timer (8254-2 - Intel Co.), thus allowing the anti-aliasing filters to be programmed. The filter output is connected to a circuit recommended by Linear to act as a buffer and eliminate clock feedthrough.

The 8254-2 has three programmable counters with independent inputs. Routines running in the PC send command words to the 8254-2 that define the cut-off frequency of the anti-aliasing filters. The other two counters of the 8254-2 are used to determine the conversion rate of the A/D IC. The PC selects the 8254-2 through the same IC's used to select the SC11310.

The A/D IC is the DSP102 manufactured by Burr-Brown. It has two converters with analog full-scale ranges of ±2.75 V. The two channels are simultaneously sampled and converted to 16-bit words that are transmitted in cascade as a 32 bit word over a single serial line. The IC also contains logic circuitry to allow these data to be interfaced to the DSP processor. The choice of the serial transmission was due to the fact that the DSP processor is able to receive the data and convert them to parallel format in a serial buffer automatically without consuming any processing time. The transfer of the data from the serial buffer of the DSP processor to the memory in the board is carried out by a DMA operation which is computationally more efficient than the use of interruptions. This approach is also more cost efficient.

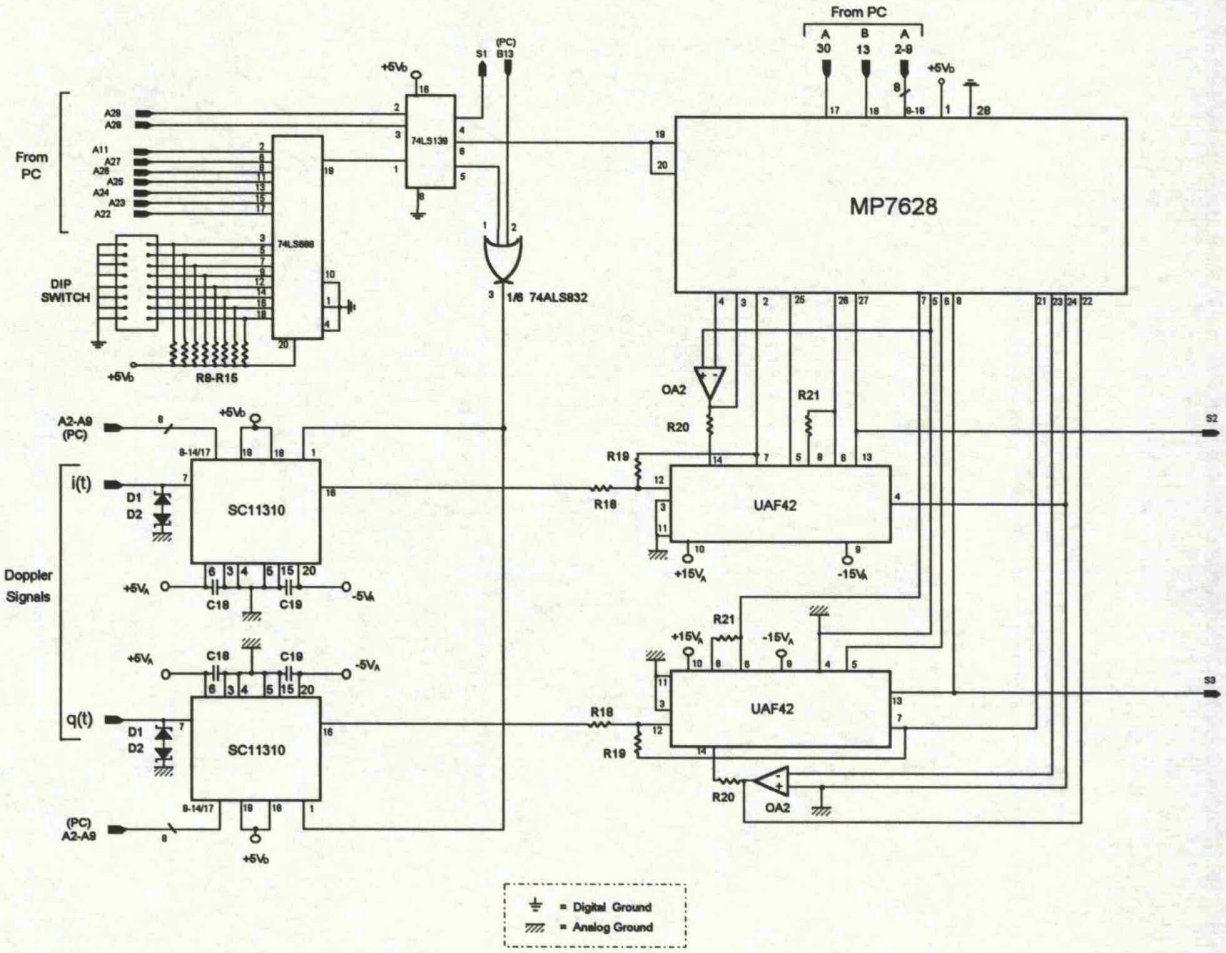

Fig. 3.1 - Partial diagram of the A/D board. This section shows the logic to enable the IC's for communication with the PC, the programmable amplifiers and the programmable 'wall thump' filters.

The DSP102 can achieve sampling rates of up to 200 kHz. The sampling and conversion is initialised by a signal generated by one of the counters of the 8254-2 programmed through routines implemented in the PC. The third counter of the 8254-2 establishes the serial data transfer rate between the DSP32C and the DSP102. The input of this counter is obtained from a clock available on the PC bus that has a frequency of 14.31818 MHz. This signal is first divided by two, with the use of a D type flip-flop, because the 8254-2 does not work with frequencies above 10 MHz. The other two counter inputs of the 8254-2 are derived from a clock generated by the DSP102. This arrangement is necessary to achieve the timing requirements of the DSP102. The output signals of the board transmitted to the DSP32C are buffered to protect the more expensive IC's with the use of available OR gates.

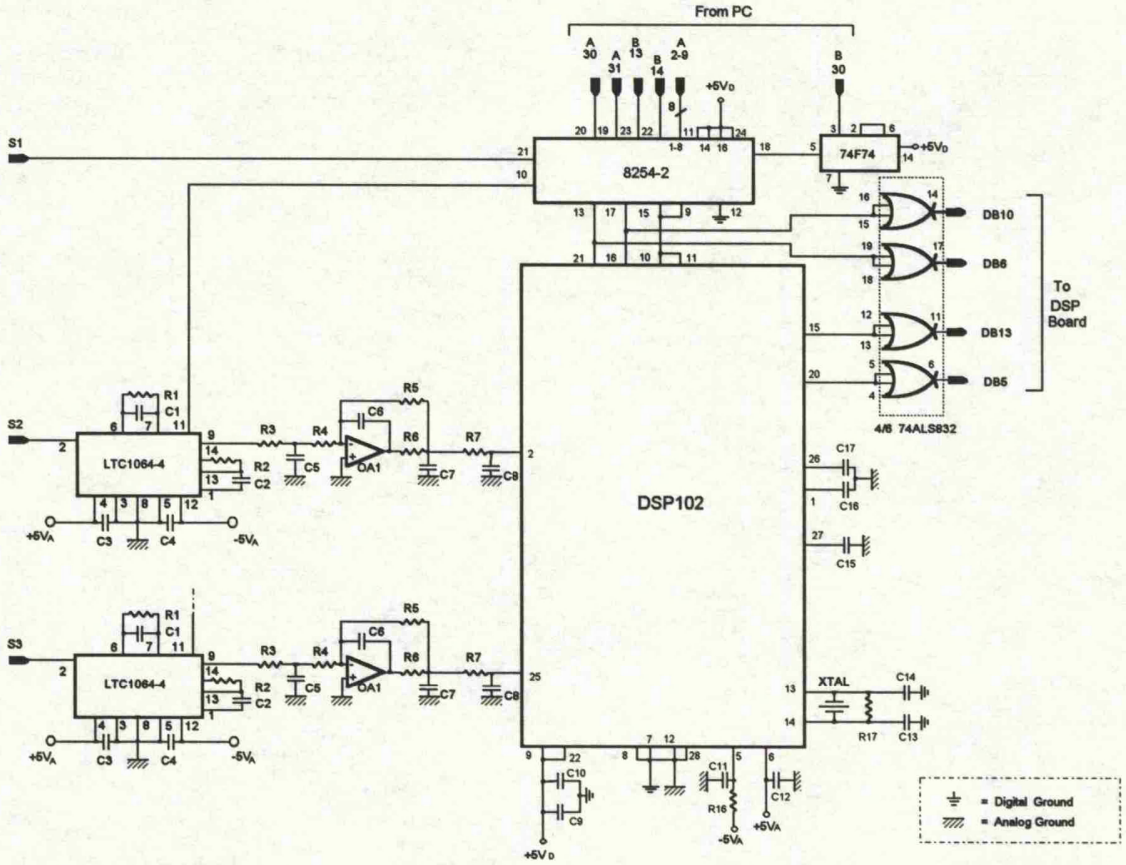

Fig. 3.2 - Partial diagram of the A/D board. This section shows the programmable timer (8254-2) which determines the cut-off frequency of the anti-aliasing filters (LTC1064-4), the A/D converters and its interface to the DSP board.

The DSP102 needs stabilised power supplies to obtain a more accurate reference for the conversions being made since the digital supply is quite noisy because of circuit switching. To provide these voltages from the PC circuits, a DC-DC converter produced by Burr-Brown (PWR5904) is used. This component also provides the power supply for the anti-aliasing filters and amplifiers. A second DC-DC converter (PWR021215 - Burr-Brown) supplies a higher voltage (15 V) to the components of the 'wall thump' filters.

The next section discusses how the sampled signals are processed to obtain a description of their frequency content. If the A/D channels are converting signals whose amplitudes exceed their maximum range, there is distortion of the sampled waveforms, and therefore, distortion of their frequency content. To alert the system user to this, the amplitude of the signals at the inputs of the A/D converters are compared to a reference of 2.75V (Fig. 3.3). If the maximum amplitude of any of the signals is higher than the reference, an interrupt is generated to the PC hardware. This interrupt prompts the execution of a routine that displays a warning message on the PC screen. The comparators have a Schmitt-trigger configuration to produce a more stable output (Millman 1979).

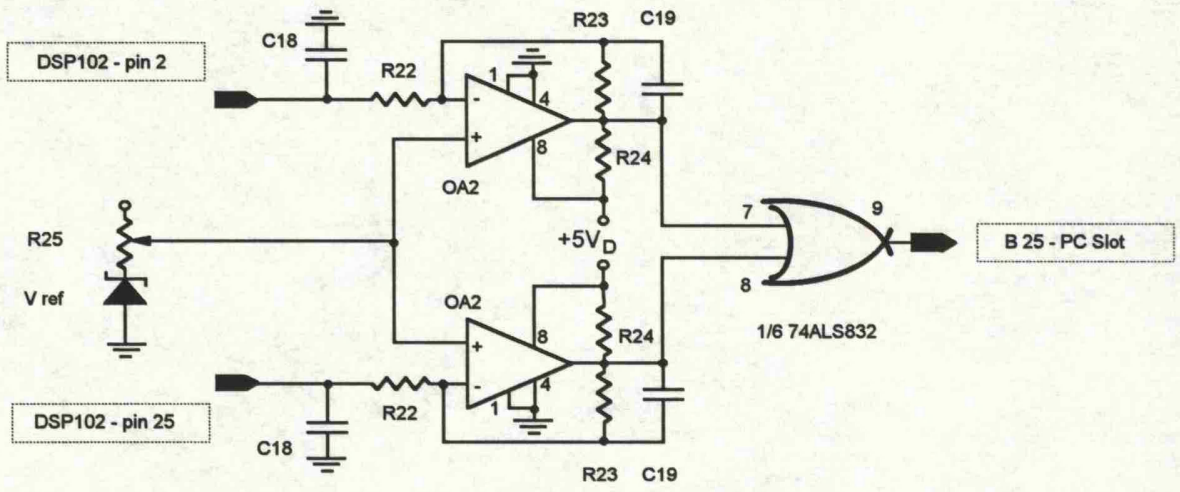

Fig. 3.3 - Circuit used in the A/D board to generate an interrupt to the PC hardware in case of detecting amplitude above the range of conversion of the A/D's.

The programmable characteristics of the board are summarised in the Table 3.1.

Function	Frequency (kHz)			
Sampling Frequency	20.48	40.96	54.62	81.92
Anti-aliasing Cut-off Frequency	10.24	20.48	27.31	40.96

Function	Minimum Value	Increment	Maximum Value
'Wall thump' Cut-Off Frequency	300 Hz	25 Hz	6375 Hz
Amplifiers Gain	0 dB	0.1 dB	24 dB

Table 3.1 - Summary of programmable characteristics of A/D board that can be changed by the user on line at the time of the signal acquisition. The sampling rate and anti-aliasing filters cut-off frequency are changed simultaneously through a common command.

3.4 - Description of the Implemented Software

The main tasks of the software described in this section are the processing of the Doppler, ECG and pressure signals, and the display of the results obtained on the PC screen.

The sub-sections below discuss aspects concerned with the ECG and pressure signal conditioning and the concepts applied to the Doppler signal processing. Descriptions of the routines developed to support the main functions are also presented.

3.4.1 - Processing of the Quadrature Doppler Signals

Blood flow in the arteries is pulsatile, presenting different velocity distributions during the cardiac cycle (Nichols and O'Rourke 1990).

Eq. 2.1 shows that the Doppler frequency is proportional to blood flow velocity. Since the sample volume insonates flow laminae having different velocities, the Doppler signal consists of the sum of several components of frequency. It is a common technique to process the Doppler signal to determine its frequency components and their relative intensities.

As the velocity distribution of the flow laminae is changing, the Doppler signal contains a variable frequency content or spectrum. The presentation of the Doppler spectrum at consecutive time intervals during the cardiac cycle is called a sonogram. The spectra are shown on axes of time and frequency, with the relative intensities of the frequency components displayed in a colour-coded mode (Fig. 3.4).

The mathematical tool used to obtain the spectrum of a Doppler signal is the Fourier transform (FT) given by (Carlson 1986):

$$F\{x(t)\} = X(f) = \int_{-\infty}^{\infty} x(t)e^{-j2\pi f}dt \qquad (3.1)$$

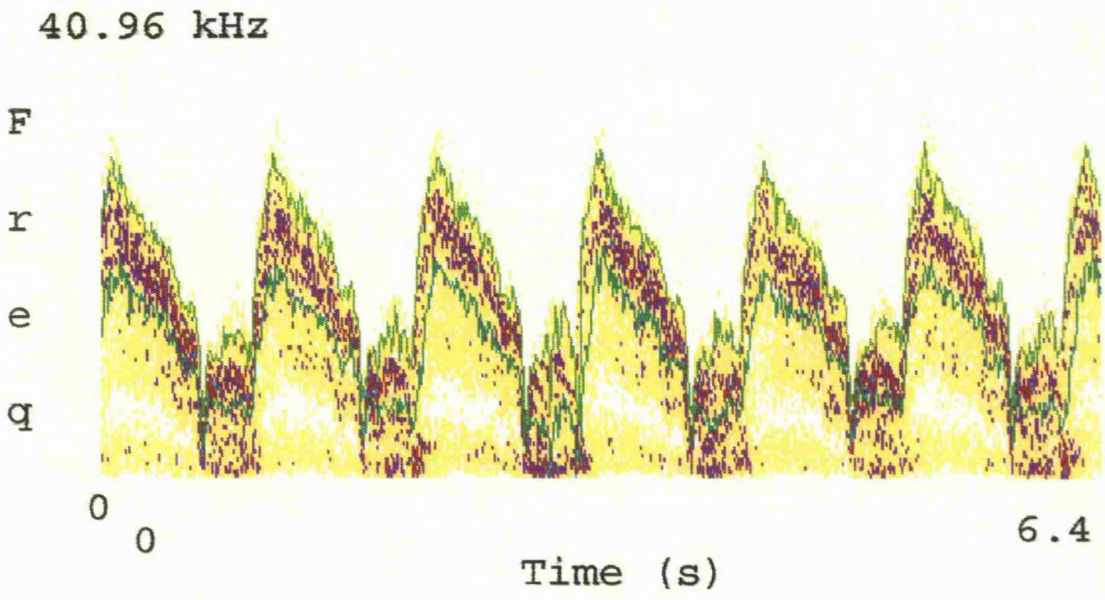

Fig. 3.4 -Example of sonogram obtained from a coronary artery.

The FT defines a continuous function in the frequency domain from a signal described in the time domain. As an example, the FT of sine and cosine functions are given by (Brigham 1974):

$$F\{A\sin(2\pi ft)\} = \frac{jA}{2}[\delta(f+f_o)-\delta(f-f_o)] \tag{3.2}$$

$$F\{A\cos(2\pi ft)\} = \frac{A}{2}[\delta(f-f_o)+\delta(f+f_o)] \tag{3.3}$$

Considering the composition of the quadrature Doppler signals, defined by Eqs. 2.2 and 2.3, as:

$$c(t) = i(t) + jq(t) \tag{3.4}$$

its description in the frequency domain can be found by calculating its FT:

$$F\{c(t)\} =$$

$$\int_{-\infty}^{\infty} \frac{A_f}{2}\{\cos\phi_f \cos(w_f t) - \sin\phi_f \sin(w_f t) - j[\cos\phi_f \sin(w_f t) + \sin\phi_f \cos(w_f t)]\}e^{-jwt}dt +$$

$$\int_{-\infty}^{\infty} \frac{A_r}{2}\{\cos\phi_r \cos(w_r t) + \sin\phi_r \sin(w_r t) + j[\cos\phi_r \sin(w_r t) - \sin\phi_r \cos(w_r t)]\}e^{-jwt}dt$$

$\therefore$

$$F\{c(t)\} =$$

$$\int_{-\infty}^{\infty} \frac{A_f}{2}\{\cos\phi_f[\cos(w_f t) - j\sin(w_f t)] - \sin\phi_f[\sin(w_f t) + j\cos(w_f t)]\}e^{-jwt}dt +$$

$$\int_{-\infty}^{\infty} \frac{A_r}{2}\{\cos\phi_r[\cos(w_r t) + j\sin(w_r t)] + \sin\phi_r[\sin(w_r t) - j\cos(w_r t)]\}e^{-jwt}dt$$

Using Eq. 3.2 and Eq. 3.3, the result is given by:

$$F\{c(t)\} = C(f) = \frac{A_f}{2}\delta(f + f_f)\{\cos\phi_f - j\sin\phi_f\} + \frac{Ar}{2}\delta(f - f_r)\{\cos\phi_r - j\sin\phi_r\}$$

The magnitude of *C(f)* is determined for two frequency components:

$$|C(-f_f)| = \frac{A_f}{2}$$

$$|C(f_r)| = \frac{A_r}{2}$$

Therefore, the FT of the complex signal given by Eq. 3.4 maps the reverse and forward components of flow onto different sides of the spectrum, positive and negative, providing an efficient technique for directional separation.

For computational purposes, the FT needs to be calculated for signals sampled during a short time interval. This implies the use of the discrete Fourier Transform (DFT) defined as (Oppenheim and Schaffer 1975):

$$X(k) = \frac{1}{N}\sum_{n=0}^{N-1} x(n) e^{\frac{-j2\pi nk}{N}} \qquad (3.5)$$

where:
n = index for the array of sampled data;
N = number of data points analysed;
k = frequency bin.

There are very efficient algorithms described in the literature to calculate Eq. 3.5. These are called fast Fourier Transforms (FFT - Oppenheim and Schaffer 1975).

The results of Eq. 3.5 describe the frequency content of the analysed signal in N discrete points spaced by Fs/N in the frequency domain, where Fs is the sampling frequency. A better frequency resolution is achieved by limiting Fs to its minimum value imposed by the Nyquist criteria. Another option is to increase the interval of observation (larger N) which results in a poorer time resolution.

Another aspect of the computational applications is that the separation of a finite length sequence from the continuous time description of the signal by the sampling procedure introduces discontinuities at its boundaries. The discontinuities produce components of frequency that were not present in the original signal. To reduce this effect, called spectral leakage, weighting functions or windows are applied to the sequence in order to smooth the boundaries. In this work, the Hann window is utilised (Harris 1978).

From the spectrum of the Doppler signal it is possible to extract two useful parameters: the maximum frequency and the intensity weighted mean frequency (IWMF). These are proportional to the maximum and mean velocity, respectively. They are largely applied to assess arterial flow dynamics (Evans et al. 1989).

A study of methods developed to detect the maximum frequency is presented in Chapter 5.

The IWMF is defined by (Evans et al. 1989):

$$IWMF = \frac{\int_f P(f) f df}{\int_f P(f) df} \tag{3.6}$$

where P(f) is the power distribution of the Doppler signal as a function of frequency. The IWMF is numerically evaluated in this work where P(f) is obtained using the FFT.

This process can be summarised in the following steps carried out by the software to display the sonogram, and the mean and maximum frequencies on the screen:

a - N pairs of quadrature Doppler samples are acquired and stored.
b - A complex Hann window is applied to the array of N complex data points where the real and imaginary values correspond to the in-phase signal samples and quadrature signal samples, respectively.
c - A FFT is performed on the windowed complex data (complex FFT - CFFT) to obtain the spectrum separated into components of forward and reverse flow.
d - The IWMF is calculated.

e - The maximum frequency is detected (Chapter 5).
f - The results of the CFFT are displayed on the screen along with the IWMF results and the detected maximum frequency.

Routines written in 'C' language for the PC program the A/D board (setting the sampling rate, amplifier gains and cut-off frequencies of the filters), load the software into the DSP board, perform step 'f' described above and reconfigure the system according to the current user settings. Routines written for the DSP32C in assembly language perform the other tasks. The exchange of data between the DSP board and the PC is achieved using library functions provided by the board manufacturer.

512 columns of Doppler spectra are presented on the PC screen. After the display of the first frame, the previous results are overwritten to present the new ones. The time interval between the presentation of the consecutive columns of the sonogram is 12.5 ms. This interval was mainly defined by the relatively low speed of the video interface and the necessity to plot a considerable number of points related to the frequency content of the analysed signal. 12.5 ms is sufficient for the PC routines to import data from the memory of the DSP board, display a column of the sonogram and carry out the other tasks.

The user can choose amongst 4 sampling rates: 20.48, 40.96, 54.62 and 81.92 kHz. This choice is made via the keyboard and routines are called to initialise the A/D board for the new mode. To show the sonogram with the same timebase for all four sampling rates, the sampled data are processed in different ways. For all of them, the CFFT is calculated for 256 pairs of samples.

For the 20.48 kHz sampling rate, 128 pairs of data are sampled and overlapped with the previous 128 sampled pairs. Therefore, a CFFT is calculated at intervals of 6.25 ms. Two CFFT results are averaged and shown on the screen.

For the sampling rate of 40.98 kHz, 256 pairs of data are sampled and the CFFT is calculated for the array. The presentation of a column of the sonogram is made after averaging two CFFT results. Each CFFT is calculated in a 6.25 ms interval.

When the 54.62 kHz sampling rate is used, 341 pairs of samples are obtained which corresponds to an interval close to 6.25 ms. 85 sampled pairs are discarded and the CFFT is calculated. The results of two CFFTs are averaged and displayed. This procedure was necessary to show the data with the same time scale as for the other rates but introduces discontinuities. Nevertheless, these discontinuities do not produce any significant error in the calculated IWMV and detected maximum velocity when compared to the results obtained for the other sampling frequencies. This has been confirmed with experiments *in vitro* in which the velocity of blood in steady flow was measured at different sampling rates.

For the highest sampling rate, 256 pairs of data are sampled. The CFFT results of 4 consecutive 256 complex arrays are averaged and the result presented. CFFTs are calculated at 3.125 ms intervals. A summary of the sampling and processing regimes is given in Table 3.2.

The averaging procedure has as advantages the reduction of spectral variance (Welch 1967) and the improvement of SNR.

For the sonogram displayed, the colour of each frequency component is set according to its amplitude and a pre-defined scale. The software offers the user 15 different options of scales to achieve a satisfactory presentation of the sonogram on the screen. The relative amplitudes, from the lowest to the highest, are coded in 16 colours: black, blue, green, cyan, red, magenta, brown, white, dark grey, light blue, light green, light cyan, light red, light magenta, yellow and bright white. In this text, the colour scale described was reversed to allow a better presentation of the sonogram print out.

Sampling Frequency (kHz)	Number of sampled pairs	Discarded sampled pairs	Overlap (%)	FFT size	Averaged FFT results
20.48	128	0	50	256	2
40.96	256	0	0	256	2
54.62	341	85	0	256	2
81.92	256	0	0	256	4

Table 3.2 - Organisation of the DSP software to generate a column of the sonogram every 12.5 ms irrespective of sampling frequencies.

3.4.2 - Processing of the ECG and Blood Pressure Signals

To present the ECG and pressure on the same time axis as the sonogram, they have to be sampled at 12.5 ms (80 Hz). The Nyquist criteria is achieved by setting the cut-off frequency of the DSP anti-aliasing filters to 40 Hz. In view of the frequency content of these signals (Chapter 2), this is a suitable value for pressure and also for ECG, since the feature of interest is the QRS complex.

To avoid fluctuations of the base line, allowing proper presentation of the ECG on the screen, a digital highpass filter (FIR - finite impulse response) is used, having a cut-off frequency of 0.7 Hz. The stopband attenuation is -25dB. This approach does not produce low frequency distortions of the ECG according to Van Alste and Schilder (1985) who pointed out that a cut-off frequency higher than 0.05 Hz can be used without distortion if linear phase filters are used, suggesting a value of 0.8 Hz for patients with heart rates as low as 48 bpm.

The pressure signal is sampled at 160 Hz. The even samples are high pass filtered, before their presentation on the screen, to eliminate base line fluctuation due to changes of the mean value during catheterization. For this, a filter with the same specifications as that for the ECG is applied. The application of a similar filter guarantees an equal time delay for both signals simplifying the storage arrangements in memory as discussed in Section 3.4.3. To track the mean pressure, the odd samples of the signal are filtered by a low-pass FIR filter with a cut-off frequency of 0.3 Hz (following the specifications of the analogue filter present in the mean pressure output of the amplifier unit used). The stopband attenuation of this filter is also -25 dB. The current mean pressure value is shown on the screen when the signals acquisition procedure is finished by the user.

Due to the biological variability of the ECG and pressure, and also because several types of equipment are utilised to acquire the ECG, it is not possible to define an absolute scale for their best presentation on screen. The software offers an option that, based on the maximum and minimum values of the data being sampled, automatically defines scaling factors for the signals. These are used to multiply the data before their display, optimising the presentation.

3.4.3 - Synchronisation of Sonogram, ECG and Pressure

Each time that 12.5 ms of Doppler signals are sampled, the system also samples the ECG and pressure. These signals are filtered before their presentation on the screen. The use of a digital filter introduces a time delay, that is, the first filtered sample is available after a given number of realisations of the filter routine supplied with consecutive samples of the signal. This delay is the same for all subsequent samples. For a FIR filter, this time delay (***TD***), in terms of the number of samples, is given by:

$$TD = \frac{T-1}{2}$$

where T is the number of filter taps (Oppenheim and Schaffer 1975).

Owing to this, the filtered samples and the column of the sonogram corresponding to an arbitrary instant t are not simultaneously available for presentation by the system.

It is necessary to store TD columns of the sonogram while the sampled ECG and pressure are being filtered. When the first results of the filtering procedure are obtained, the PC imports the first column of the sonogram and shows all the results on screen, maintaining their synchronism. The first stored column is then overwritten by the most recent CFFT results. This procedure continues in a circular mode.

For the filter with the characteristics specified in Section 3.4.2, the number of taps required is 70. Therefore, the processing results are presented 0.875s (70*12.5ms) after the acquisition of the signals.

As mentioned previously, the application of the same filter for the ECG and pressure signals simplifies the software. It is not necessary to create a second buffer to store intermediate results for a different filtering procedure as would be necessary if a filter with a different number of taps, or a different time delay, were used for the pressure.

3.4.4 - Additional Characteristics of the Implemented Software

The software was designed to provide a friendly interface to the user, allowing its utilisation in the catheter room by a technician following a minimum period of training. A description of all its functions can be found in Appendix A. Some of its characteristics are highlighted here.

Ideal software should inform the operator about the system settings and present all useful information on the system screen. The physical size of the presented data is also important to allow, in this particular work, the doctors to follow the data acquisition procedure from a more remote position.

It was not possible to achieve all these requirements in this work because of the amount of data to be shown and the limitations of the video interface. The screen is configured for 640x350 pixels since the use of a higher resolution would result in slower speeds and dimensional compression of the sonogram and other curves.

The data may be displayed in two alternative modes together with the system settings: (a) sonogram of forward and reverse flow components or (b) sonogram of forward flow, ECG and pressure waveforms. The operator can at any moment switch between these two display modes. This methodology was chosen because reverse flow is not very often observed in coronary circulation.

The sampling frequency, gain of the amplifiers, cut-off frequency of anti-aliasing filters and 'wall thump' filters can be changed by the operator at any time during the signal acquisition, through the keyboard. The current settings are shown on the acquisition screen to keep the user informed about them. The sampling frequency and the cut-off frequency of the anti-aliasing filters are simultaneously changed by the same command to obey Nyquist criteria.

The software offers the possibility of storing the processed signals on disk files to form a data bank. This allows the testing of new hypotheses with the data available,

reducing research time and costs. The routines implemented for this purpose do not allow the files to be accidentally overwritten, verifying if there is already any stored file with the name given to the new one. It also checks if the disk is full or damaged. Appropriated warning information is displayed in all these cases. These functions were felt necessary to assure that data obtained with considerable effort could not be lost by improper use of the system. Another option allows the data files to be instantly recalled.

There are three kinds of data that can be stored: the frequency envelopes together with curves of pressure and ECG, the sonogram, or the raw Doppler signals. For each of these options, data about the patient are saved at the beginning of the file, allowing identification of the stored files. This information must be introduced by the user through the keyboard before data acquisition. The patient data are retained in memory and saved in all subsequent stored files. If any file is retrieved for verification, the current patient data in memory are overwritten by the retrieved data. This information is deleted from the memory when the file is closed and means that current patient data must be re-entered, but avoids storing data of one patient under the name of another. Information on the sampling rate used is also stored. The arrangement of the data in these files is described in Appendix B. When the user selects the option of storing envelopes, the curves of maximum and mean velocity, ECG, mean pressure and pulsatile pressure are loaded into the memory for a period of 6 minutes. The software automatically stops when the buffer is full and the maximum velocity, mean velocity, ECG and pulsatile pressure waveforms can be inspected and also copied to a file on disk. The user can interrupt the procedure at any time and save the data already in the memory into a disk file. These files are stored with the extension *.STR. Fig. 3.5 shows an example of data read from one of these files. The values of mean pressure are not currently used, but stored for further investigation.

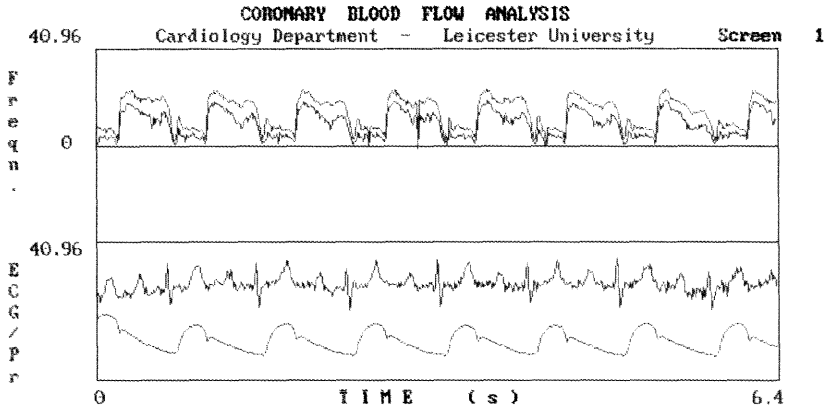

Fig. 3.5 - Example of stored file containing the maximum frequency envelope of the sonogram, the calculated IWMF, ECG and pressure waveforms.

This is the most important data storing option since these files can be used to calculate the parameters discussed in the introductory chapter. Software implemented to carry out their calculation is discussed in Chapter 9.

To have a better idea of the quality of the maximum and mean velocity estimations, it is useful to keep a hard copy of the sonogram with the display of these curves. The software allows the user to produce a print out of the current screen together with the patient data as shown in Appendix A.

Optionally, these data can be stored on disk files. The ECG and pressure are stored even if they are not shown on the screen. If reverse flow is not present, it is advisable to switch the presentation mode to show the ECG and pressure. The stored files for this option are smaller because the information on reverse flow is not saved. These files are stored with the extension *.DOC. An example of data retrieved from this type of files is shown in Fig. 3.6.

Quadrature Doppler signals are not properly stored by tape recorders since this medium introduces significant phase and amplitude errors to the recorded data. The source of these errors in Digital Audio Recorders (DAT) are the non simultaneous sampling of the quadrature channels and the imbalance of recording levels between the two channels used (Bush and Evans 1993). These problems are overcome by the A/D board described in Section 3.3.

The interest in storing Doppler signals is to allow their off-line investigation (Chapter 7). Up to 640 kbytes of quadrature Doppler signals can be recorded. They can be sampled at any of the available rates. It was mentioned in Section 3.4.2 that for the sampling rate of 54.62 kHz, 85 pairs of samples are discarded before CFFT calculation. Nevertheless, they are stored to avoid discontinues in their off-line analysis.

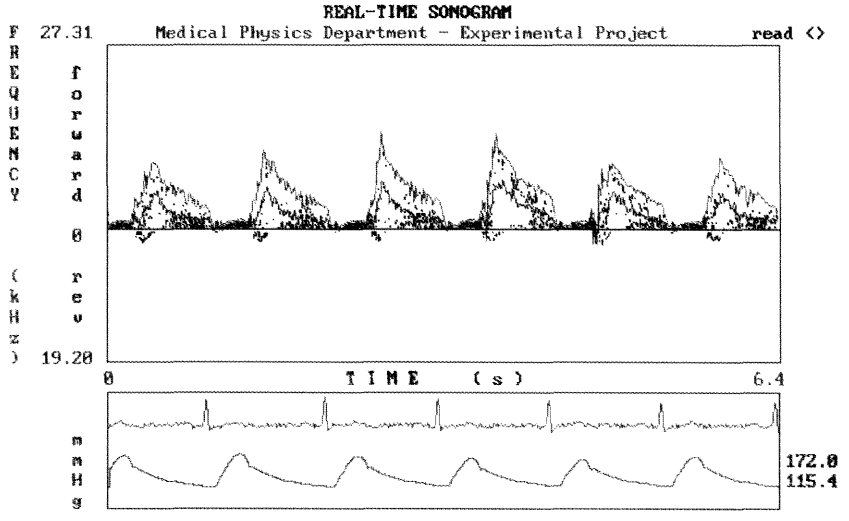

Fig. 3.6 - Example of stored file containing copy of screen showing the sonogram, the detected maximum frequency envelope, the calculated IWMF, ECG and pressure waveforms.

3.5 - Summary

This chapter has described the hardware and the software implemented to sample and process Doppler signals for performing measurements of coronary blood flow velocity and to observe its phasic pattern based on sampled curves of ECG and pressure. The system allows the sampled and processed signals to be stored in files for future examination or further processing off-line.

Chapter 4 - Assessment and Compensation of Phase and Amplitude Imbalance in Quadrature Doppler Signals

4.1 - Introduction

As mentioned in Chapter 2, the output signals of the commonest Doppler systems are generated by quadrature phase demodulators (QPD). If the sampled vessel has blood flowing in only one direction, the QPD outputs should present equal amplitudes and a 90 degree phase difference. If that is not the case, there is a phase and/or amplitude imbalance between the two channels which produces an image response at frequencies negative to those that constitute the actual signal. This effect is called cross-talk. Cross-talk introduces errors into the IWM velocity estimation and may create difficulties for the interpretation of the sonograms.

The level of cross-talk generated by the amplitude and phase imbalance can, respectively, be calculated by (Taylor 1984):

$$C_A(dB) = -\left|20\log\left(\frac{1-\delta}{1+\delta}\right)\right|$$

$$C_P(dB) = -\left|20\log\left(\tan\left(\frac{\phi}{2}\right)\right)\right|$$

where:
δ = ratio of in-phase (I) and quadrature (Q) signal amplitudes;
ϕ = phase imbalance ||arg(I) - arg(Q)|-90°|.

Figs. 4.1.a and 4.1.b show the degree of cross-talk that occurs as a function of amplitude and phase imbalance derived from the equations above.

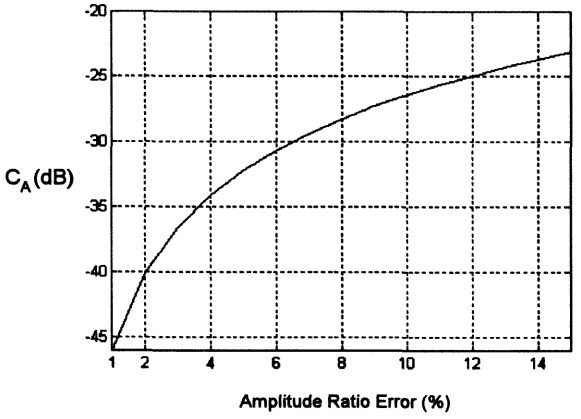

(a)

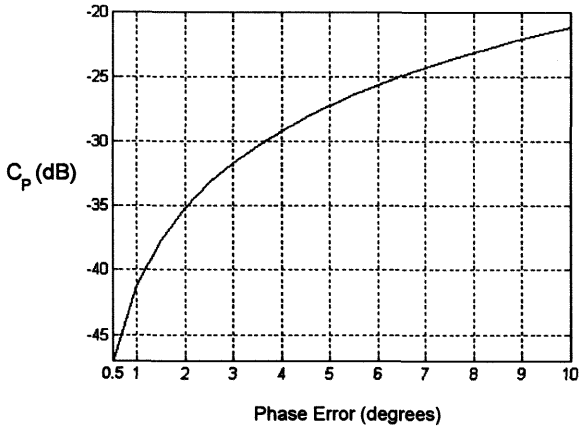

(b)

Fig. 4.1 - Cross-talk plotted as a function of the quadrature signals amplitude ratio (a) and phase error (b).

4.2 - Assessment of Phase and Amplitude Imbalance for the Intravascular Doppler System

In order to characterise the performance of the Doppler system used in this work, the phase and amplitude imbalance present in its outputs were investigated.

For this purpose, two intravascular transducers (described in Chapter 2) were immersed in a coupling medium and placed face to face. One of the transducers was connected to the Doppler system, whilst the other was driven by a function generator producing a sinusoid. The frequency of the generated signal was decreased in steps, below the carrier frequency of 20 MHz, to cover the bandwidth of the acquisition, (Fs/2), where Fs is 20.48 kHz. The peak-to-peak voltage applied to the transducer was kept low (30 mV) to avoid waveform distortion in the receiver system. Following this, measurements were repeated increasing the generated signal above the carrier frequency so as to simulate flow towards the transducer.

At each excitation frequency, the Doppler signals were sampled and stored on disk by the system developed (Chapter 3). These signals were later analysed using commercial software. A 256 point real FFT was obtained for each of the quadrature signals, I (in-phase) and Q (quadrature), and the magnitudes and phases of these two components compared to each other, to determine the magnitude ratio and phase imbalance. For each data file, the results obtained from 3 frames were averaged. The results for the simulated flow away from the catheter are presented in Fig. 4.2. Similar results were obtained for the simulated reverse flow.

It is possible to see from Fig. 4.2 that, close to the cut-off frequency of the anti-aliasing filters (10.24 kHz), the values of the gain and phase imbalance vary dramatically. For the range in which they present more stable behaviour (up to 9.5 kHz), the averaged gain imbalance was 3.35% and the average phase imbalance, 5.99 degrees.

Modern Doppler units employ integrated circuit filters after the demodulator ensuring good matching of the phase characteristics of these devices. It is therefore assumed that the phase imbalance observed is mainly due to the demodulation process. Both the symmetry of the phase errors experienced by frequencies above and below the carrier, and the success of the compensation methods used, confirm this assumption.

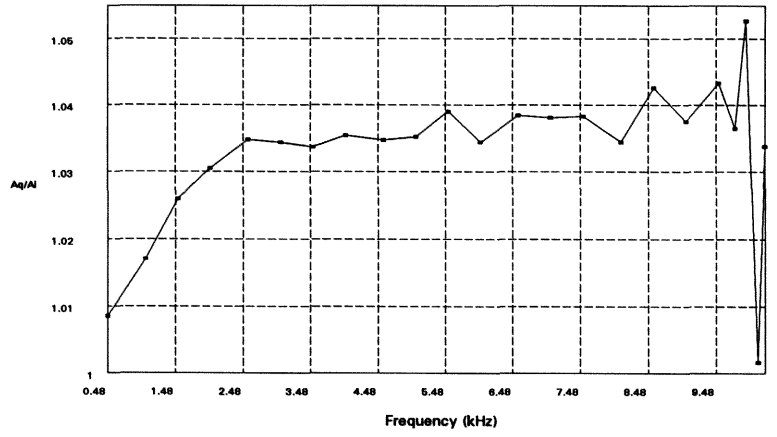

(a)

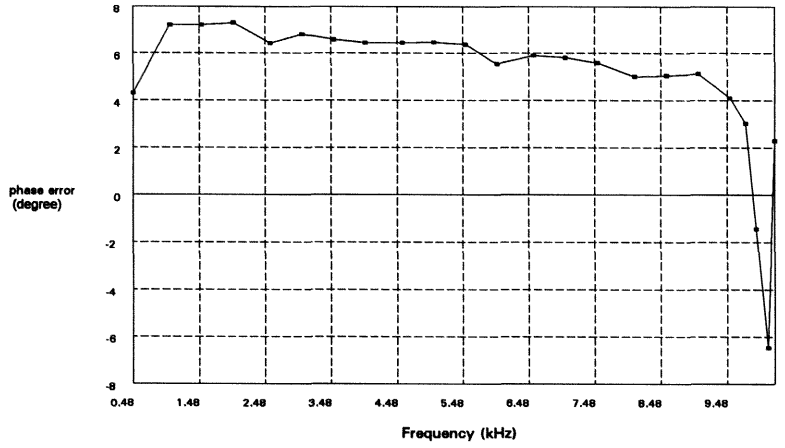

(b)

Fig. 4.2 - Measured gain (a) and phase imbalance (b) as a function of frequency for the Millar Doppler system.

4.3 - Compensation for Phase and Amplitude Imbalance

In presence of phase imbalance generated by the demodulator, Eqs. 2.2 and 2.3 should be rewritten as:

$$i(t) = \frac{A_f}{2}\cos\left(w_f t + \phi_f + \phi_x\right) + \frac{A_r}{2}\cos\left(w_r t - \phi_r - \phi_x\right) \tag{4.1}$$

$$q(t) = \frac{A_f}{2}\cos\left(w_f t + \phi_f + 90^\circ\right) + \frac{A_r}{2}\cos\left(w_r t - \phi_r - 90^\circ\right) \tag{4.2}$$

where:
ϕ_x = phase imbalance produced by the quadrature demodulator.

Recently, Aydin and Evans (1994) have reviewed digital techniques to derive directional information from quadrature Doppler signals. In this section we discuss how modifications can be introduced in two of these digital techniques to compensate phase and gain imbalance while obtaining directional information. These techniques are the phase domain method and the Weaver receiver method.

4.3.1 - Phase Domain Technique

This procedure was discussed in Section 2.2.3. For its digital implementation, Hilbert transformers are used to produce a phase shift of 90° (Aydin and Evans 1994). Fig. 4.3 reproduces Fig. 2.7 with the modifications introduced for the intended compensation. As shown below, the generation of modified phase shifts can compensate for the phase imbalance in *i(t)* and *q(t)*. To complement this section, the development of a digital phase shifter based on the work of Darlington (1950) is presented and an example of its implementation given.

From Eq. 4.1, a phase shift of (90° + ϕ_x) for *i(t)* yields:

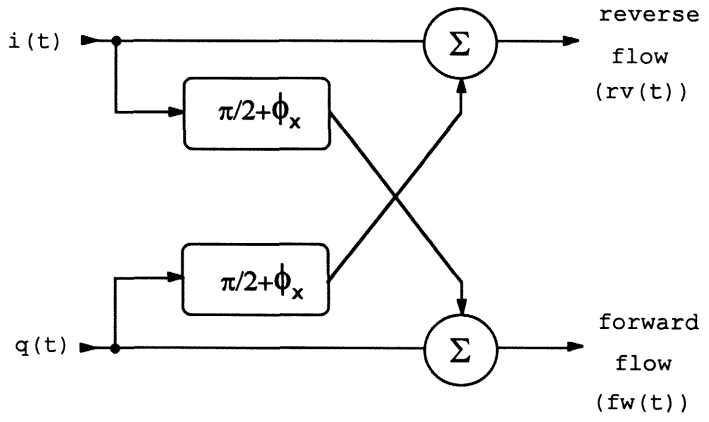

Fig. 4.3 - Block diagram of phase domain technique modified to compensate phase imbalance.

$$si(t) = \frac{A_f}{2}\cos(w_f t + \phi_f + 90^\circ + 2\phi_x) + \frac{A_r}{2}\cos(w_r t - \phi_r + 90^\circ) \qquad (4.3)$$

Summing Eq. 4.2 to Eq. 4.3, we have:

$$fw(t) = \frac{A_f}{2}\left[\cos(w_f t + \phi_f + 90^\circ) + \cos(w_f t + \phi_f + 90^\circ + 2\phi_x)\right]$$

therefore: $fw(t) = A_f \cos\phi_x \cos(w_f t + \phi_f + 90^0 + \phi_x)$.

A phase shift of $(90^\circ + \phi_x)$ for ***q(t)*** yields:

$$sq(t) = \frac{A_f}{2}\cos(w_f t + \phi_f + 180^\circ + \phi_x) + \frac{A_r}{2}\cos(w_r t - \phi_r + \phi_x) \qquad (4.4)$$

Summing Eq. 4.1 to Eq. 4.4, we have:

$$rv(t) = \frac{A_r}{2}\left[\cos(w_r t - \phi_r + \phi_x) + \cos(w_r t - \phi_r - \phi_x)\right]$$

therefore: $rv(t) = A_r \cos\phi_x \cos(w_r t - \phi_r)$.

To produce sonograms, FFT can be applied for each of the resultant signals. As can be seen, the two signals are scaled down by a same constant ($\cos\phi_x$) which will not introduce errors in the calculated intensity weighted mean velocity (Evans et al. 1989). To compensate for gain imbalance the samples of either in-phase or quadrature channel should be multiplied by a constant obtained from experimental observations so as to equalise their amplitude.

Phase Shifter Filter

An arbitrary phase shifter, as required for the phase domain compensating configuration, can be generated by digital filters. Fig. 4.4 illustrates the filter structure used for this purpose. In the *s* plane, the transfer functions of the all-pass filters of Fig. 4.4 are given by:

$$H_1(s) = C_1 \prod_{l=0}^{m} \frac{(s-a_l)}{(s+a_l)} = \frac{A_1 - sB_1}{A_1 + sB_1}; \qquad (4.5.a)$$

$$H_2(s) = C_2 \prod_{l=1}^{m} \frac{(s+a_l)}{(s-a_l)} = \frac{A_2 + sB_2}{A_2 - sB_2}; \qquad (4.5.b)$$

where:
C = gain;
a_l = the poles of the functions;
$s = j\Omega$;
Ω = analogue frequency.

The phase difference β generated by the phase shift network is:

$$\beta = \beta_2 - \beta_1 = \arg(H_1 H_2) = \arg\left(\frac{A+Bs}{A-Bs}\right)$$

From this, it is possible to note that the roots of (A - Bs) are those of $\left(1 - j\tan\frac{\beta}{2}\right)$.

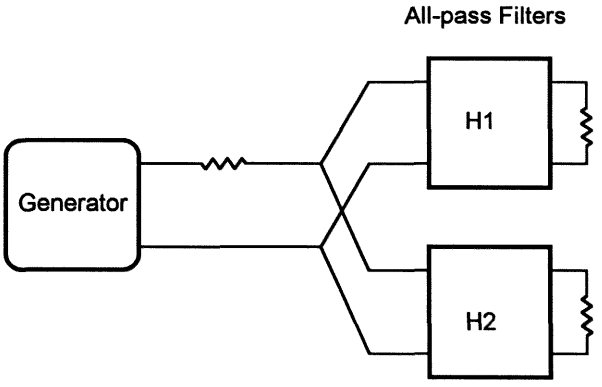

Fig. 4.4 - Diagram of a phase shifting network to produce an approximately constant phase difference.

To obtain a Chebyshev approximation for tan(β/2) between Ω_1 and Ω_2, where Ω_1 and Ω_2 are, respectively, the inferior and superior limits of the frequency range of interest, the following parametric equations in u were proposed (Darlington 1950):

$$\tan\left(\frac{\beta}{2}\right) = \tan\left(\frac{\beta_a + \varepsilon}{2}\right) \mathrm{dn}\left(\frac{nuK_1}{K}, k_1\right); \tag{4.6}$$

$$\Omega = \Omega_2 \, \mathrm{dn}(u,k); \tag{4.7}$$

where:
dn = a Jacobian elliptic function;
K = complete elliptic integral of k;
K_1 = complete elliptic integral of k_1;
β_a = average phase difference for the range of approximation;
ε = maximum error;

$$k = \sqrt{1 - \left(\frac{\Omega_1}{\Omega_2}\right)^2}; \tag{4.8}$$

$$k_1 = \sqrt{1 - \left[\frac{1}{U}\left(\frac{U - \tan\varepsilon}{1 + U\tan\varepsilon}\right)\right]^2}; \tag{4.9}$$

$U \cong \tan\left(\frac{\beta_a}{2}\right)$ for small ε (when compared to β_a);

$$n = \left(\frac{K(k)K'(k_1)}{K'(k)K(k_1)}\right); \tag{4.10}$$

$K'(k)$ = complete elliptic integral of $\sqrt{1-k^2}$;
$K'(k_1)$ = complete elliptic integral of $\sqrt{1-k_1^2}$.

For real values of the parameter u, Ω oscillates between Ω_1 and Ω_2 while $\tan(\beta/2)$ oscillates n times more frequently between $\tan\left(\frac{\beta_a+\varepsilon}{2}\right)$ and $\tan\left(\frac{\beta_a-\varepsilon}{2}\right)$, presenting the desired behaviour (Fig. 4.5).

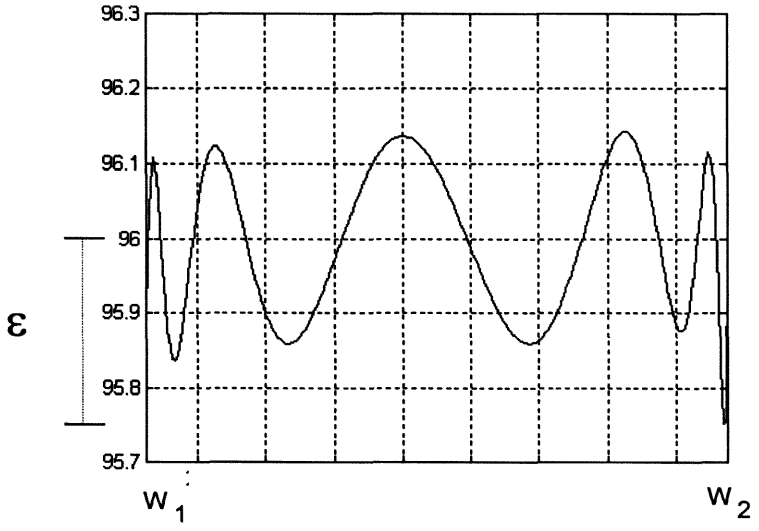

Fig. 4.5 - Example of phase difference generated by the approach described (this curve was obtained with the use of digital filters where the design specifications were $\beta_a = 96°$, $w_1 = 5°$, $w_2 = 175°$and $\varepsilon = 0.22°$. w = digital frequency).

With the use of the parametric equations above, the roots of $\left(1-j\tan\frac{\beta}{2}\right)$ in the s plane are found to be given by (Darlington 1950):

$$a_q = \Omega_2\left(\frac{\mathrm{cn}\left(\frac{2qK}{n}+u_0\right)}{\mathrm{sn}\left(\frac{2qK}{n}+u_0\right)}\right), \quad \text{q=0,...,(n-1).} \tag{4.11}$$

where:

$u_0 = \frac{K\beta_a}{n\pi}$ (β_a in radians);

cn, sn = Jacobian elliptic functions.

To achieve a physically realisable phase shifter, the resultant polynomials should have their poles on the left side of the s plane, therefore, the positive poles of $(A - Bs)$ or $\left(1-j\tan\frac{\beta}{2}\right)$ are assigned to Eq. 4.5.a and the others, to Eq. 4.5.b (Darlington 1950).

All pass filters are IIR filters that can be designed with few taps, allowing their digital implementation for real time applications. The number of taps will depend on the specification of the design, namely w_1, w_2 and ε, where w_1 and w_2 are digital frequencies which correspond to their analogue counterparts Ω_1 and Ω_2 defined above (Fig. 4.5).

To obtain the poles in the z plane, a bilinear transform is applied to the above equations (Oppenheim and Schafer 1975), making:

$$\Omega = \tan(w/2); \tag{4.12}$$

$$s=\left(\frac{z-1}{z+1}\right); \tag{4.13}$$

Tan(w/2) replaces Ω in Eq. 4.8 and Eq. 4.11. Substituting Eq. 4.13 in Eq. 4.15, the transfer functions for the z plane are given by:

$$H_1(z)=C_1\prod_{l=1}^{m}\frac{\left[z\left(\frac{1-a_l}{1+a_l}\right)-1\right]}{\left[z-\left(\frac{1-a_l}{1+a_l}\right)\right]}; \tag{4.14.a}$$

$$H_2(z)=C_2\prod_{l=1}^{m}\frac{\left[z\left(\frac{1+a_l}{1-a_l}\right)-1\right]}{\left[z-\left(\frac{1+a_l}{1-a_l}\right)\right]}; \tag{4.14.b}$$

The phase shift of the all-pass filters are negative for $0<w<\pi$ (Oppenheim and Schafer 1975). The multiplication of Eq. 4.14.a by e^{j180} will allow the filtered signals to be in phase with the input signals.

Filter Implementation

Based on the figures obtained during the characterisation of phase imbalance of the Doppler system, all-pass filters were designed with the following specifications: β_a = 96°, w_1 = 5°, w_2 = 175°and ε = 0.22°. As an example of the procedure, all steps to design these particular filters are given below. The solutions of the equations containing Jacobian elliptic functions and integrals were obtained with standard routines in a commercial software package (Matlab, The MathWorks Inc., USA).

a) Determination of k, k_1 and n.

$$k = \sqrt{1-\left(\frac{\tan(w_1/2)}{\tan(w_2/2)}\right)^2} = 0.99999818;$$

$$k_1 = \sqrt{1-\left[\frac{1}{\tan\left(\frac{\beta_a}{2}\right)}\left(\frac{\tan\left(\frac{\beta_a}{2}\right)-\tan\varepsilon}{1+\tan\left(\frac{\beta_a}{2}\right)\tan\varepsilon}\right)\right]^2} = 0.12376944;$$

$$n = \left(\frac{K(k)K(\sqrt{1-k_1^2})}{K(\sqrt{1-k^2})K(k_1)}\right) = 11.99177680;$$

b) Determination of u_0 and a_q.

Making n equal to 12, the closest integer number:

$$u_0 = \frac{K(k)\beta_a}{n\pi} = 0.35535437;$$

And solving:

$$a_q = \tan(w_2/2)\left(\frac{cn\left(\frac{2qK}{n}+u_0\right)}{sn\left(\frac{2qK}{n}+u_0\right)}\right), \quad q=0,...,11.$$

The roots of $\left(1-j\tan\frac{\beta}{2}\right)$ are given by:

$a(q)$ = [63.116537 8.769669 2.239543 0.589099 0.153952 0.035206 -0.011203 -0.080631 -0.315737 -1.200320 -4.593030 -20.084696];

c) Determination of the poles in the *z* plane.

For the positive values of the array *a*(q), the poles of $H_1(z)$ are equal to:

$$p1_l = \left(\frac{1-a_l}{1+a_l}\right);$$

And their values are:

$p1$ = [-0.968807 -0.795285 -0.382629 0.258575 0.733174 0.931982];

For the negative values of the array a(l), the poles of $H_2(z)$ can be calculated as:

$$p2_l = \left(\frac{1+a_l}{1-a_l}\right);$$

And the results are

$p2$ = [0.977842 0.850771 0.520060 -0.091041 -0.642412 -0.905144];

d) Determination of transfer functions.

Expressing the general form of a transfer function as:

$$H(z) = C\left(\frac{b(1)+b(2)z^{-1}+\ldots+b(nb+1)z^{-nb}}{a(1)+a(2)z^{-1}+\ldots+a(na+1)z^{-na}}\right);$$

$H_1(z)$ and $H_2(z)$, considering the multiplication by e^{j180}, may be written as:

$$H_1(z) = -1.0 * \left(\frac{-0.052088 + 0.072984z^{-1} + 0.663646z^{-2} - 0.271400z^{-3} - 1.570371z^{-4} + 0.222989z^{-5} + z^{-6}}{1.0 + 0.222989z^{-1} - 1.570371z^{-2} - 0.271400z^{-3} + 0.663646z^{-4} + 0.072984z^{-5} - 0.052088z^{-6}} \right);$$

$$H_2(z) = \left(\frac{-0.022904 - 0.218147z^{-1} + 0.454643z^{-2} + 0.845155z^{-3} - 1.343255z^{-4} - 0.710075z^{-5} + z^{-6}}{1.0 - 0.710075z^{-1} - 1.343255z^{-2} + 0.845155z^{-3} + 0.454643z^{-4} - 0.218147z^{-5} - 0.022904z^{-6}} \right);$$

The curve obtained for the phase-shift difference generated for these filters is that presented in Fig. 4.5. To save computational time, the amplitude imbalance can be compensated by the filters if two sets with same coefficients but different gains C are used such that: $H1_i = \frac{A_q}{A_i} H1_q$ and $H2_i = \frac{A_q}{A_i} H2_q$, where $H1_i$ and $H2_i$ constitute the pair of filters to produce the phase shift for ***i(t)***, $H1_q$ and $H2_q$ constitute the pair of filters to generate the phase shift for ***q(t)*** and $\frac{A_q}{A_i}$ is the ratio of amplitude imbalance between the quadrature and in-phase channel respectively.

4.3.2 - Weaver Receiver Technique

Fig. 4.6 shows the block diagram for this method (Evans et al. 1989). Sampled in-phase and quadrature Doppler signals are multiplied by sampled $\cos(w_p t)$ and $\sin(w_p t)$, respectively, where w_p is the angular frequency of a pilot oscillator. The results of the product are summed to generate a signal whose forward and reverse components are disposed above and below the pilot frequency, respectively. The digitally generated sinusoidal quadrature curves should be stored in look-up tables of the FFT size for a more efficient implementation. Compensation of phase imbalance may be obtained by multiplying Eq. 4.1 by $\cos(w_p t + \phi_x)$ instead of $\cos(w_p t)$:

$$S1(t) = \frac{A_f}{4}\left[\cos(w_p t - w_f t - \phi_f - \phi_x + \phi_x) + \cos(w_p t + w_f t + \phi_f + 2\phi_x)\right] + \\ + \frac{A_r}{4}\left[\cos(w_p t - w_r t + \phi_r + 2\phi_x) + \cos(w_p t + w_r t - \phi_r - \phi_x + \phi_x)\right] \quad (4.15)$$

Multiplying Eq. 4.2 by $\sin(w_p t)$:

$$S2(t) = \frac{A_f}{4}\left[-\cos(w_p t - w_f t - \phi_f) + \cos(w_p t + w_f t + \phi_f)\right] + \\ + \frac{A_r}{4}\left[\cos(w_p t - w_r t + \phi_r) - \cos(w_p t + w_r t - \phi_r)\right] \quad (4.16)$$

Adding Eqs. 4.15 and 4.16:

$$S3(t) = \frac{A_f}{4}\left[\cos(w_p t + w_f t + \phi_f) + \cos(w_p t + w_f t + \phi_f + 2\phi_x)\right] + \\ + \frac{A_r}{4}\left[\cos(w_p t - w_r t + \phi_r) + \cos(w_p t - w_r t + \phi_r + 2\phi_x)\right]$$

Therefore:

$$S3(t) = m\left[A_f \cos(w_p t + w_f t + \phi_f + \phi_x) + A_r \cos(w_p t - w_r t + \phi_r + \phi_x)\right]$$ where:

$m = \left(\frac{\cos\phi_x}{2}\right)$, scales all frequency components by a same value.

To obtain sonograms, it is necessary to apply a real FFT to S3(t) and the spectrum corresponding to the forward and reverse flows are presented around the pilot frequency. For compensating gain imbalance the samples of either in-phase or quadrature channel should be multiplied by a constant obtained from experimental observations in order to equalise their amplitude. To save computational time, one of the look up tables can incorporate this constant, for instance, generating the

sinusoidal look up table as $\frac{A_i}{A_q}\sin(w_p)$, where $\frac{A_i}{A_q}$ is the ratio of amplitude imbalance between the in-phase and quadrature channels.

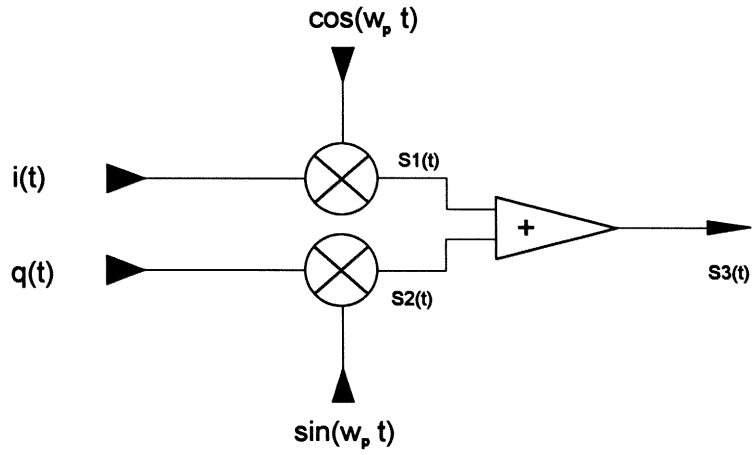

Fig. 4.6 - Block diagram of Weaver receiver technique for directional separation of quadrature Doppler signals.

4.4 - Results

This section presents results obtained for the compensating structures discussed above when applied to quadrature Doppler signals sampled from the outputs of the Doppler system investigated. They were implemented using a commercial software package (Matlab, The MathWorks Inc., USA).

Figs. 4.7 and 4.8 show comparisons of results obtained for the phase domain technique without (Fig. 4.7.a and Fig. 4.8.a) and with compensation (Fig. 4.7.b and Fig. 4.8.b). Fig. 4.7 presents the results of 256 points FFTs for the demodulated signals resulting of a simple tone (generated as explained in Section 4.2). Fig. 4.8

shows a similar comparison to that given in Fig. 4.7 in which data sampled from a coronary artery were used. It can be seen that the cross-talk of the signal peak magnitude, present in the reverse flow side, is 22 dB below the actual signal peak, but comparable with the level of other signals in the forward flow channel. The compensation reduces the cross-talk to the level of the noise. Each of these figures consist of the real spectrum of two FFTs as should be composed to produce a sonogram displaying forward and reverse flow.

The results obtained for the Weaver receiver technique are presented in Figs. 4.9 and 4.10 for the same signals shown in Figs 4.7 and 4.8. Figs. 4.9.a and 4.10.a show the results without compensation for a single tone and data sampled from a coronary artery. The results with compensation are shown in Fig. 4.9.b and 4.10.b. Each of these results display the real spectrum of a 256 points FFT. The pilot frequency corresponds to $-\pi/2$.

For all results presented in this section, the FFTs were calculated after application of Hanning windows to the data.

4.5 - Discussion and Conclusion

As the results have shown, in spite of not correcting phase distortions precisely at each frequency, the methods of compensation suggested allow good separation to be achieved. Both the phasing-filter technique and the Weaver receiver technique when combined with phase compensation improve directional separation.

For the phasing-filter technique, it should be noted that the filters do not have the desired behaviour below w_1 and above w_2. Care must therefore be taken to ensure that w_1 is below the cut-off frequency of the 'wall-thump' filters and w_2 is above the highest frequency present in the Doppler signals.

The Weaver receiver and phasing-filter techniques have been previously implemented in this laboratory for real time applications (Aydin and Evans 1994). As discussed by Aydin and Evans (1994), the Weaver receiver technique is faster than the phasing-filter technique, but in order to avoid aliasing due to the frequency shift around the pilot frequency, a higher sampling frequency may be necessary which results in lower spectral resolution. Compensation for phase imbalance is remarkably straight-forward using the modified Weaver method described here since it is only necessary to use a different look up table for one of the digital mixers, not adding extra computational time. The implementation of the phasing-technique in real time was achieved with a FIR Hilbert transformer. The proposed modifications for compensating phase and gain imbalance employ IIR phase shifters with a small number of taps allowing even a faster implementation and ensuring its viability for real time applications.

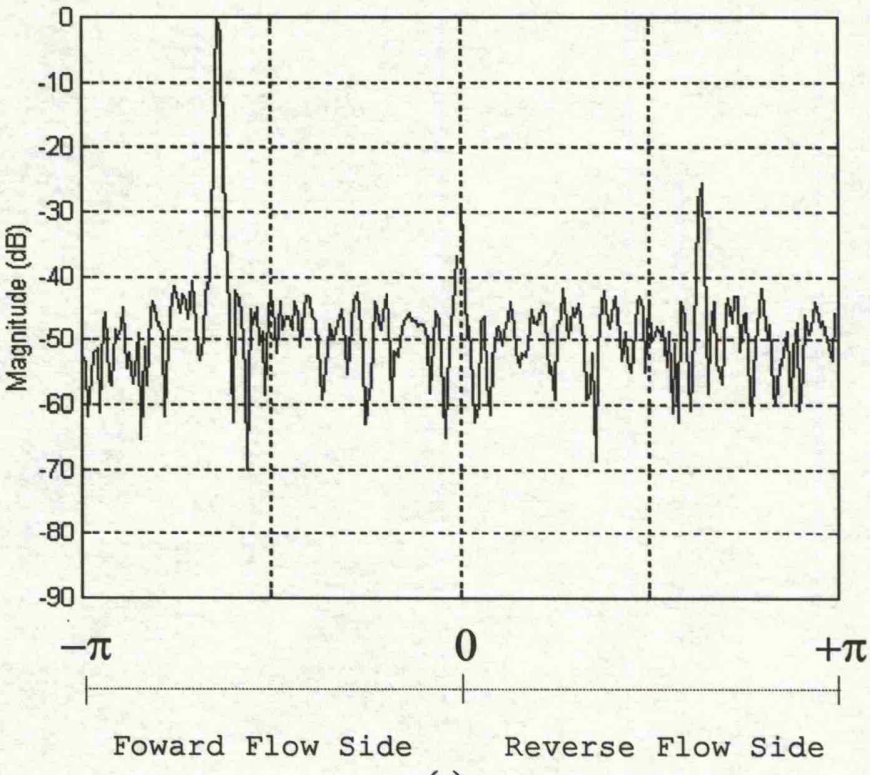

(a)

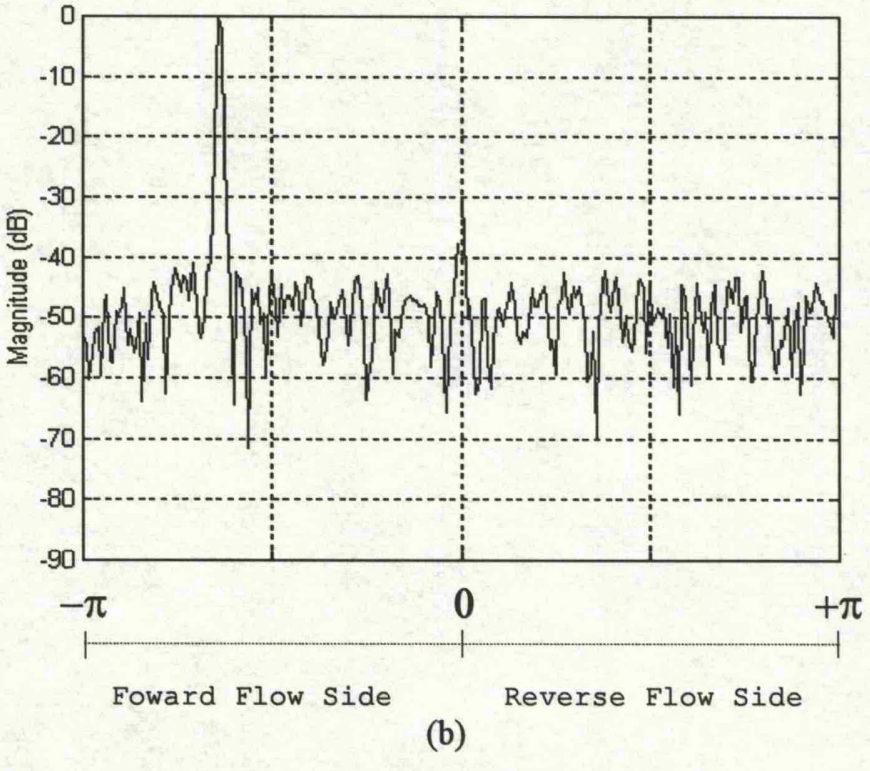

(b)

Fig. 4.7 - FFT results of directional Doppler signals generated by simple tone before (a) and after (b) compensation of phase and gain imbalance by phase domain technique. The cross-talk can clearly be seen in (a).

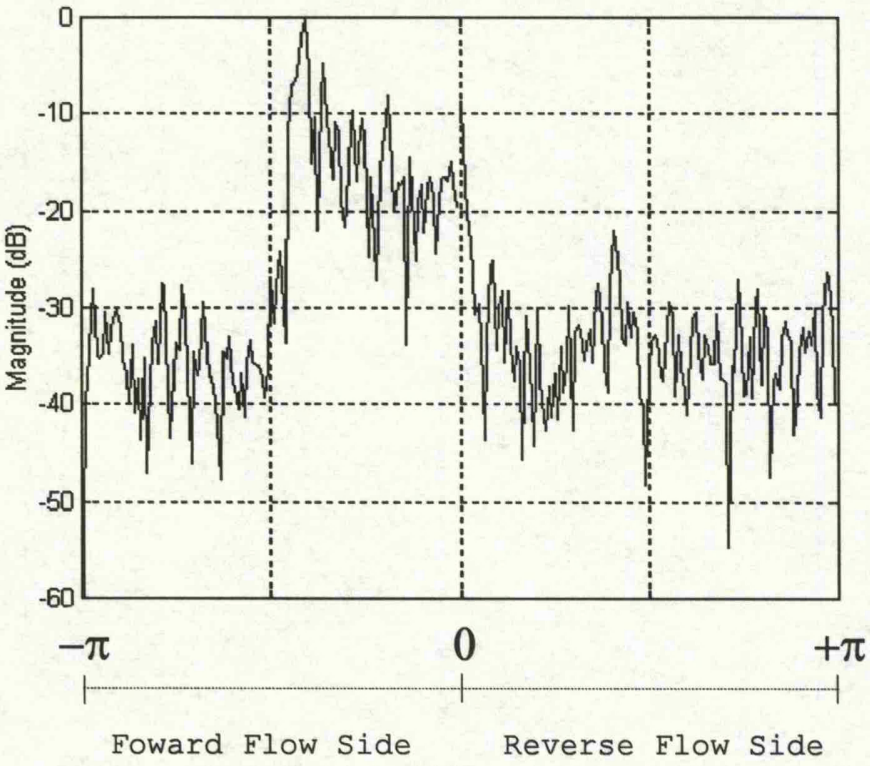

(a)

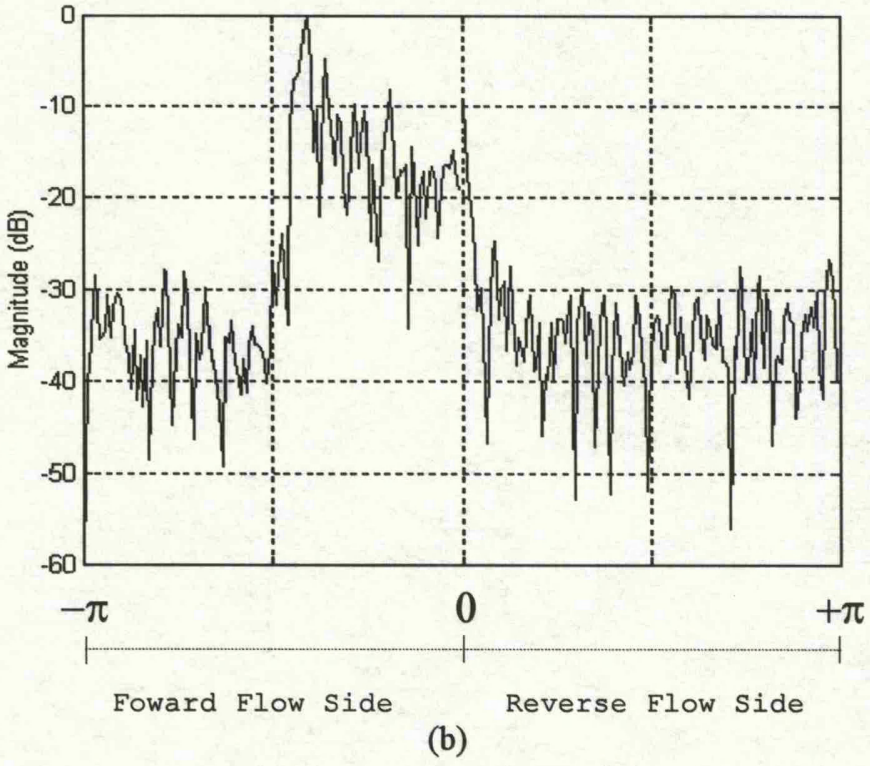

(b)

Fig. 4.8 - FFT results of directional Doppler signals sampled from a coronary artery before (a) and after (b) compensation of phase and gain imbalance by phase domain technique.

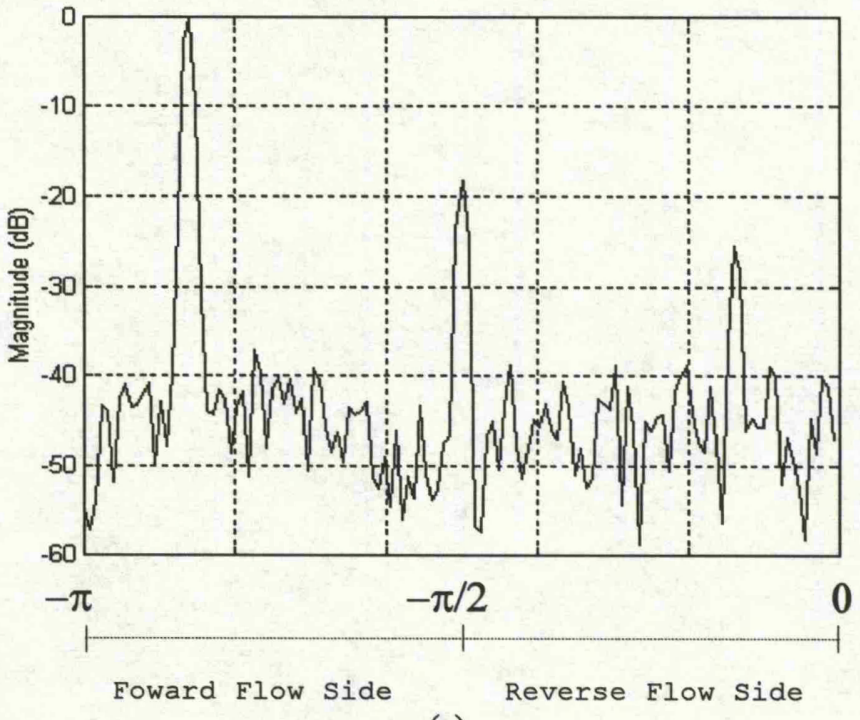

(a)

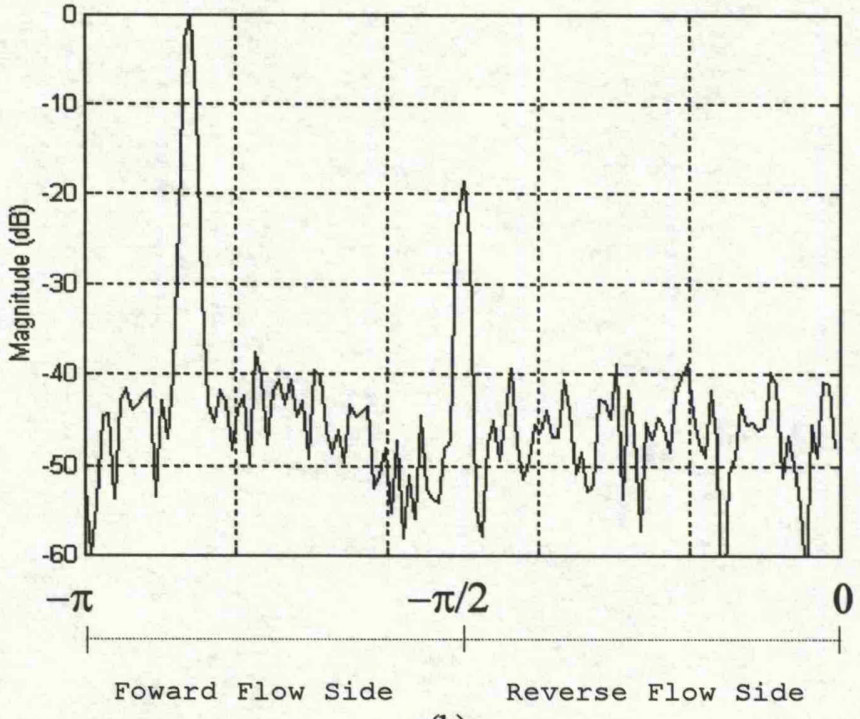

(b)

Fig. 4.9 - FFT results of Doppler signals generated by simple tone before (a) and after (b) compensation of phase and gain imbalance by Weaver receiver technique. The pilot frequency is at -π/2.

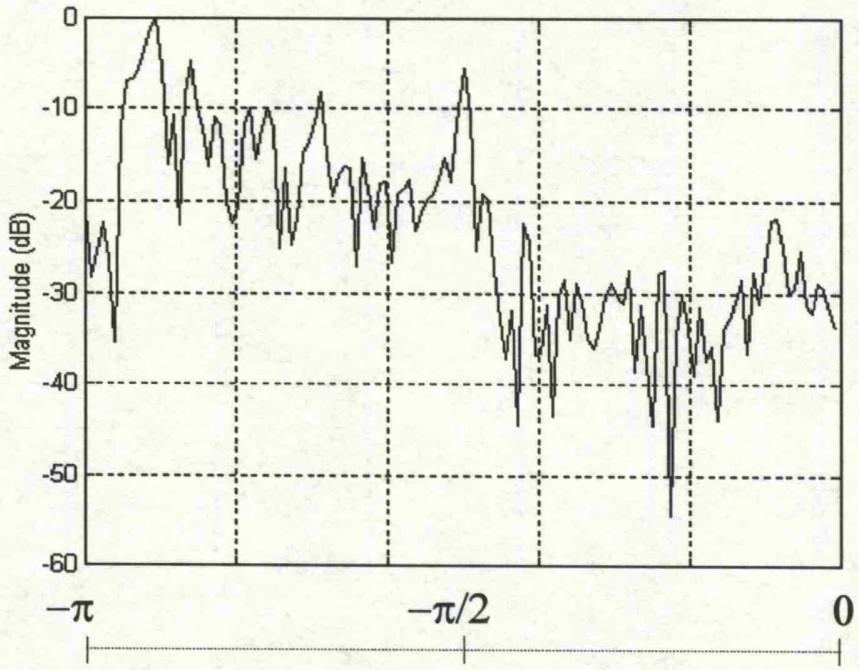

(a)

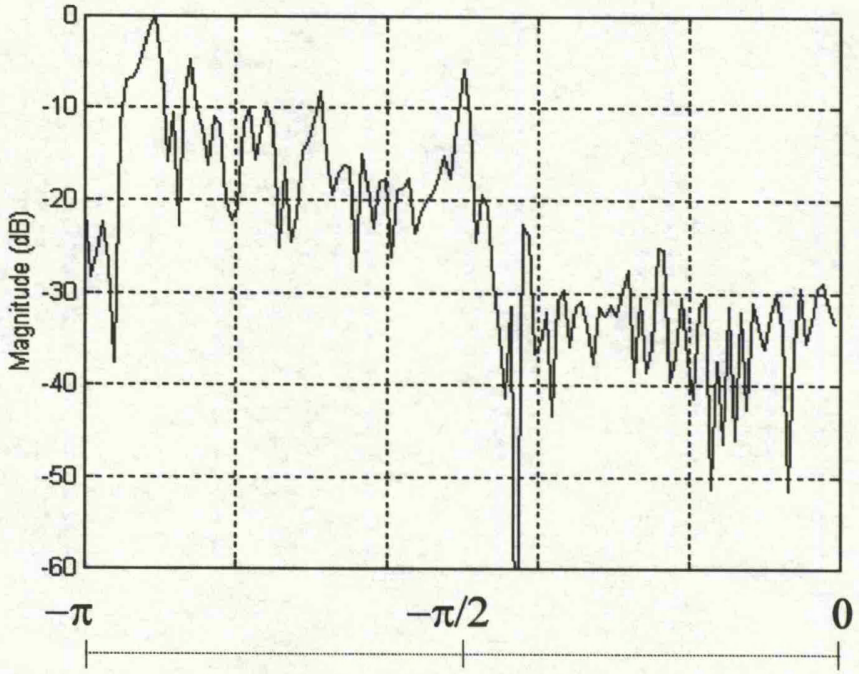

(b)

Fig. 4.10 - FFT results of Doppler signals sampled from a coronary artery before (a) and after (b) compensation of phase and gain imbalance by Weaver receiver technique. The pilot frequency is at -π/2.

Chapter 5 - Study on Maximum Velocity Envelope Detectors

5.1 - Introduction

Interest in obtaining the maximum frequency envelope (MFE) from Doppler sonograms first appeared in the work of Gosling et al. (1969, 1971). These authors were interested in circumventing artefacts present in zero-crossing detectors for a better estimation of pulsatility index. Their method was carried out off-line in a semi-automatic way.

Nowadays, several workers use intensity-weighted mean frequency for a better estimation of mean velocity (Arts and Roevros 1972; Schlindwein et al. 1988), surmounting some of the problems discussed in the literature on the zero-crossing method (Lunt 1975). Nevertheless, clinical observations and applications have established the use of MFE (Kassam et al. 1985; Nakatani et al. 1992). There are also some advantages of the MFE when compared with other frequency followers since its output is not significantly influenced by ultrasonic beam shape, it is less affected by the wall thump filters and it has higher noise immunity (Evans et al. 1989).

Several approaches have been suggested in the literature to carry out MFE detection (Sainz et al. 1976; Johnston et al. 1978). Algorithms using digital techniques have also been proposed (D'Alessio 1985; Mo et al. 1988). Mo et al. (1988) evaluated four different digital methods for this purpose. According to their study, the modified threshold crossing method (MTCM) shows a better performance than the percentile and the D'Alessio methods, and produces similar results to a fourth method (hybrid method) of higher complexity.

Recently, Marasek and Nowicki (1994) have proposed a new MFE detector, the Geometric Method (GM), comparing its performance with the percentile and the modified threshold crossing methods for different spectral estimators.

In this chapter, the aim is to compare the MTCM recommended by Mo et al. (1988) with the simple threshold method (STM) where the threshold is subjectively set by the operator (Gibbons et al. 1981), and a modified version of the recently proposed GM.

The following sections describe the investigated techniques, the experimental procedure used for their comparison, results and the choice made. Clinical results are also discussed.

5.2 - Description of the Maximum Frequency Envelope Detection Methods

Fig. 5.1 illustrates a typical spectrum of a short Doppler signal segment obtained from a carotid artery using both a rectangular window and a Hanning window. They give information about the intensity of the combined signal and noise components. MFE detectors have to find the transition level between the signal and the noise regions that corresponds to highest frequency present in the signal. The rationales behind the methods investigated in this chapter are discussed below.

5.2.1 - Simple Threshold Method (STM)

Gibbons et al. (1981) proposed the use of an arbitrary threshold to detect the transition mentioned above. This threshold is increased or decreased by the user through the computer keyboard according to his/her evaluation of the quality of the resulting MFE. Having found the threshold that produces the best performance this is kept constant within a particular segment of the signal.

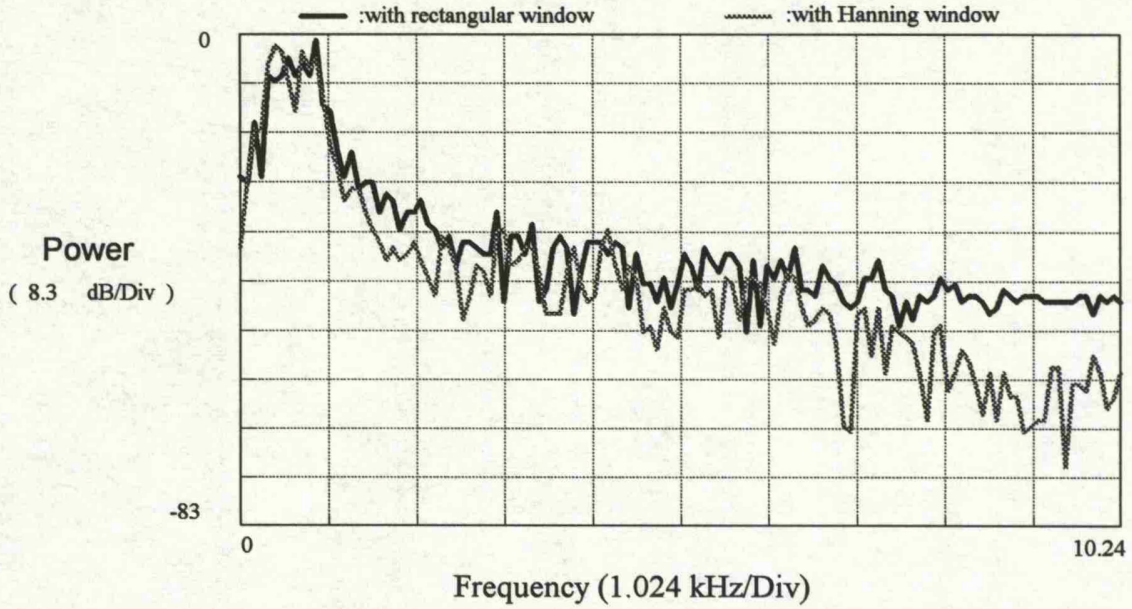

Fig. 5.1 Doppler signal spectrum obtained from a carotid artery using rectangular and Hanning windows.

5.2.2 - Modified Threshold Crossing Method (MTCM)

This method is based on D'Alessio's algorithm (1985). D'Alessio (1985) considers that the tail of the Doppler spectrum gives information on the level of the noise present in the signal since white noise is spread over all frequencies. An estimation of the noise made in the tail of the spectrum is then used for setting a threshold. The magnitude of each bin of the spectrum (scanning from the upper to the lower frequency bins) is compared with the threshold and when the magnitudes of two successive bins are larger than the threshold, the first bin is labelled as the maximum frequency bin. The application of this method for each column of the sonogram allows the determination of a threshold that dynamically adapts to the SNR. This method assumes that rectangular window is applied to the Doppler signal. However this window introduces large side-lobes (Harris 1978) and therefore is not frequently used.

When other windows are applied to the sampled Doppler signal, there is a smoothing of the noise present in the tail of the spectra (Fig. 5.1 - Hanning window) and based on its level, a higher threshold needs to be set for the MFE detection. To determine this threshold, the noise estimation is multiplied by a constant that is empirically chosen for the system in use (Mo et al. 1988). It should be noted that in either situation, the noise level at the tail of the spectra estimation is also affected by the anti-aliasing filter characteristics.

With the MTCM the signal must not be present in the tail of the spectra where the noise magnitude is estimated. This can cause difficulties with fixed length FFT systems because the Doppler spectrum must be confined to the lower part of the spectrum, requiring the use of a higher sampling frequency. This implies a poorer resolution that will give less accuracy to the maximum velocity estimation.

5.2.3 - Modified Geometric Method (MGM)

Marasek and Nowicki (1994) proposed a method in which the maximum frequency for each column of the sonogram is estimated on the basis of the shape of its integrated spectrum curve (ISC). This curve is calculated by:

$$ISC(f) = \sum_{i=0}^{f} P(i)$$

where P(i) is the estimated power for each frequency component of the Doppler spectrum. The ISC characteristic shape is given by a steep slope, representing the incremental power sum of signal and noise, and then a smoother slope that occurs for the region of the spectrum where only noise is present.

Fig. 5.2 shows a typical Doppler spectrum and its ISC given by the curve GED. The maximum frequency of the spectrum is assumed to correspond to the point where the perpendicular distance between the ISC and a reference line is maximum ('f_B' - Fig. 5.2). The reference line (|CD| - Fig. 5.2) is drawn from the end of the ISC to the point corresponding to the frequency which has the maximum magnitude of the spectrum ('f_{MC}').

In our implementation of this algorithm three modifications were made. When the blood flow is changing direction, it is possible to have some columns of the sonogram in which no flow is detected. In this case, the ISC will be formed only by the noise power. Application of the geometric method in this case will produce a spike. To prevent this, we have introduced a minimum threshold to be compared to the total power of the spectrum. If the power is smaller than the threshold, it is assumed that no flow is present. The result of this has proved to be quite satisfactory, but again, the use of an empirical criteria is necessary.

A second problem with the method is that it depends on the position of the absolute maximum magnitude in the spectrum which can fluctuate quite markedly due to the variance of the spectral estimator, and may also be influenced by noise spikes. The modified implementation uses a reference line which links the first to the last point of the ISC (|GD| - Fig. 5.2) and therefore is unaffected by the variation of the estimator.

Marasek and Nowicki (1994) used the projection of the maximum distance between the reference line and the ISC on the frequency axis, making the maximum frequency detection susceptible to amplifier gain. If the power of the entire signal is halved (curve GON - Fig. 5.2), there obviously is no change in the maximum frequency, but the projection given by |KL| is different from that given by |AB|.

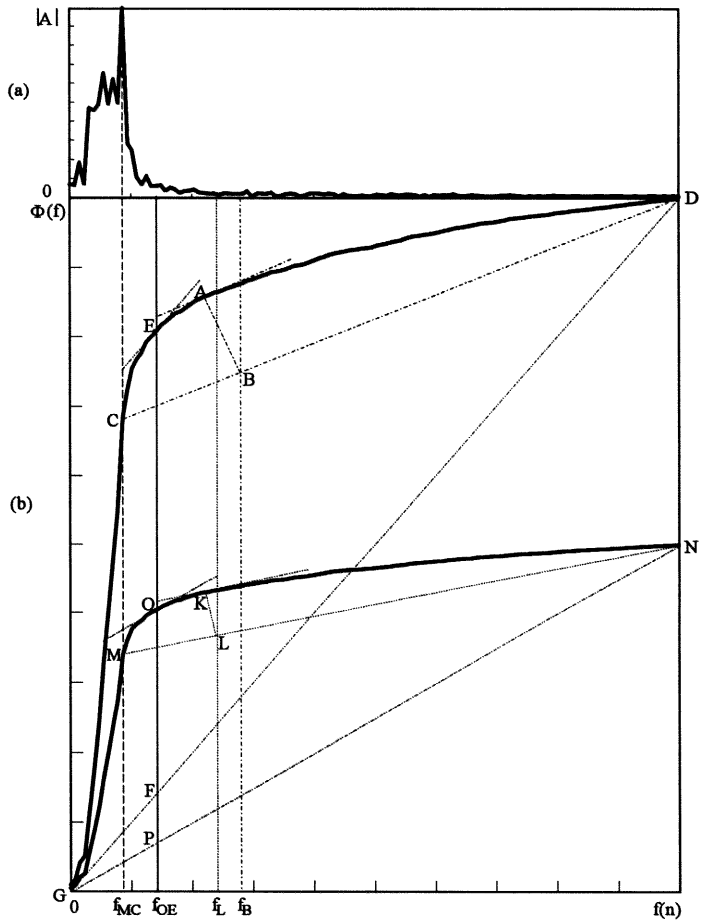

Fig. 5.2 - (a) Doppler signal spectrum and (b) its integrated spectrum curve at two different gains.

This can be better understood with the use of equations derived from Fig. 5.3, where the origin of the XY axes is placed on the point that corresponds to the maximum magnitude of the spectrum to simplify the equations below.

From the similar triangles ΔQPR and ΔQRS, it is possible to write:

$$\cos\alpha = \frac{a}{\sqrt{a^2+b^2}} = \frac{\delta h}{\delta s} \tag{5.1}$$

$$\sin\alpha = \frac{b}{\sqrt{a^2+b^2}} = \frac{\delta x}{\delta h} \tag{5.2}$$

where $\delta s = y_q - y_p$.

Rearranging these equations, we obtain:

$$\delta h = \frac{a}{\sqrt{a^2+b^2}}\delta s, \tag{5.3}$$

$$\delta x = \frac{b}{\sqrt{a^2+b^2}}\delta h \tag{5.4}$$

By substituting Eq. 5.3 into Eq. 5.4, δx can be expressed as:

$$\delta x = \frac{ab}{a^2+b^2}\delta s \tag{5.5}$$

If the gain is changed by a factor of k, all parameters defined in the y direction are multiplied by this constant. Using Eq. 5.5, the new δx becomes:

$$\delta' x = \frac{akb}{a^2+k^2b^2}\delta' s \tag{5.6}$$

where $\delta' s = k\delta s$. The relation between $\delta' x$ and δx can be expressed as:

$$\delta' x = \frac{a^2+b^2}{\left(\frac{a^2}{k^2}+b^2\right)}\delta x \tag{5.7}$$

Eq. 5.7 demonstrates that different gains will result in different values for δx which represents the difference between the maximum frequency bin and the knee of the ISC.

In order to provide maximum frequency detection independent of gain, we associate its position with the point that corresponds to the maximum distance between the ISC and the line from the origin to the end of the ISC rather than using its projection ('f_{OE}' for both curves- Fig. 5.2). In spite of these modifications, it is possible to see that this method produces a reasonable detection of the 'knee' of the ISC which has been shown to correspond to the maximum frequency (Mo et al. 1988).

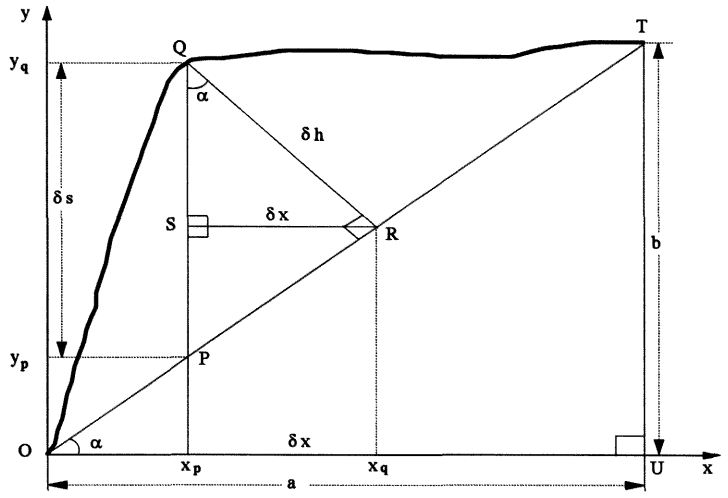

Fig. 5.3 - Integrated spectrum curve and geometry used to show that maximum frequency detection is dependent on gain for the GM.

5.3 - Methodology

The system utilised for the evaluation of the three methods is based on a DSP board installed in an IBM compatible (as described in Chapter 3). All methods were implemented in assembly of the DSP32C processor. Routines written in 'C' for the PC interact with the DSP board in order to present the results on the screen.

For a quantitative evaluation, white noise (since the Doppler signal has a Gaussian distribution - Mo and Cobbold 1986; Guo et al. 1993) was sampled from an analogue generator and processed, using DSP techniques, to produce analogue narrow-band quadrature signals whose frequency content was determined by digital band-pass filters. A second IBM compatible PC was used to sample and store the quadrature signals whose averaged spectra are presented in Fig. 5.4. This approach was taken to include the effect of the anti-aliasing filters in the assessment of the performance of the MFE's.

The spectra shown in Fig. 5.4.a has a very well defined maximum frequency (4 kHz) and provides a good basis for an objective comparison of the methods. This spectra does not however correspond to those obtained in clinical practice since the latter are subjected to intrinsic spectral broadening (ISB) effects (Evans et al. 1989).

All the other simulated Doppler signals (Fig. 5.4.b - 5.4.f) were designed to incorporate ISB effects. These signals were designed to have their 4 kHz frequency components in the fall-off region being attenuated approximately by half of the stopband attenuation. This was done to provide a reference value for the detections. The signals whose spectra are given by Figs. 5.4.a, 5.4.b and 5.4.c were used to analyse the effect of ISB on MFE detection. For these three signals, the high-pass frequency was set to 0.4 kHz to include the 'wall thump' filtering effect.

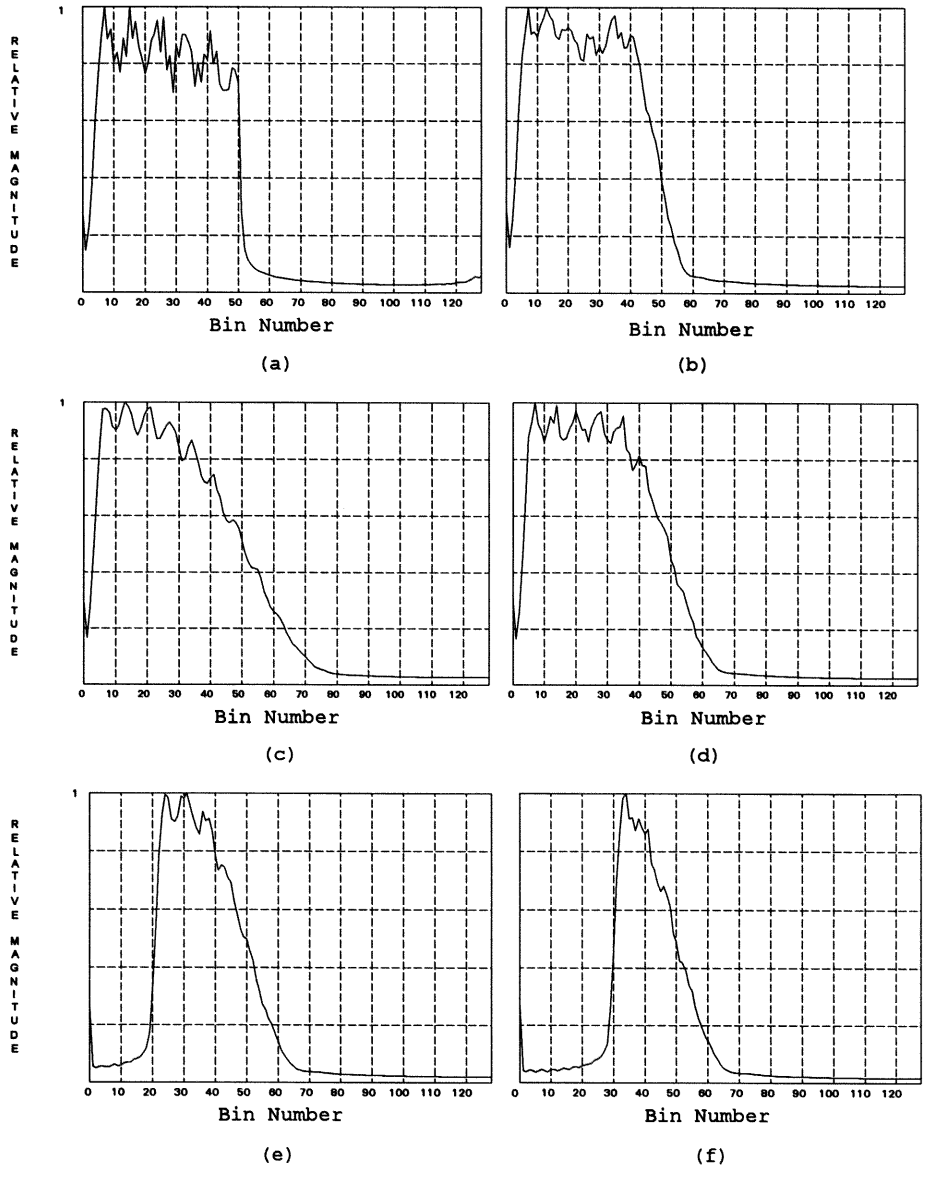

Fig. 5.4 - Averaged spectra of the simulated Doppler signals used to compare the performances of the MFE detectors. Their magnitudes are normalised by their respective maximum values. They are presented in terms of a bin scale to be related to the results presented later on. The correspondent frequency can be found by multiplying the scale by the bin spacing (80 Hz/bin).

To analyse the effect of bandwidth on the MFE detection, the spectra given by Fig. 5.4.d was made narrower by using higher high-pass frequencies: 1.8 kHz for Fig. 5.4.e and 2.56 kHz for Fig. 5.4.f. The low-pass filter specifications used to generate these signals were unchanged.

The MFEs obtained with the simulated Doppler signals were digitally stored for statistical evaluation. For further analysis, sampled white noise (therefore, incorporating the effect of anti-aliasing filters) was digitally added to the simulated Doppler signals to produce different SNRs and the behaviour of the MFE detection algorithms for these signals was observed. The SNRs levels utilised were: 25, 20, 17.5, 15, 12.5 and 10 dB.

The waveforms used in these experiments were sampled at a frequency of 20.48 kHz. The DSP board anti-aliasing filters were 4th order Butterworth, having a cut-off frequency of 6 kHz. The software applied a Hanning window to the data and calculated a 256-point complex FFT before implementing the MFE detections. Therefore, the frequency resolution or bin spacing is equal to 80 Hz/bin.

For qualitative comparison of the three methods in terms of real clinical situation, quadrature Doppler signals from a carotid artery were sampled and digitally stored.

5.4 - Results

500 detections were used to estimate each of the averaged values and their standard deviations. The mean value and standard deviation of the detected maximum bin obtained with each of the three methods for the signals at different SNRs are shown in Figs. 5.5 and 5.6, respectively. In all curves, the bin 50 corresponds to the maximum frequency of 4 kHz.

For the STM, several threshold values were tried to achieve the best envelope detection according to the evaluation of the operator.

The threshold used in the MTCM should be empirically set by the programmer according to the characteristics of the system. The software developed for this work allows the user to change the value of the constant to be multiplied by the noise estimation. This was done in order to find the best subjective value, and because the same constant was unable to cover the SNR range used in this study. To compare it with the other methods, it was necessary to set a new constant for each of the SNR ranges. The MTCM is different from the STM in being able to adapt to small SNR changes.

The MGM was able to adapt satisfactory to the different SNR and presented similar values of standard deviation when compared to the other methods. The detected values were affected by the SNR and the intrinsic spectral broadening. Narrow band signals allow a higher noise contribution for the integrated spectrum curve which results in a MFE overestimation for the MGM.

Fig. 5.7 shows the MFE obtained by each of the methods for the Doppler signals recorded from a carotid artery. The MGM achieves similar results to the other methods in spite of being totally automatic. For the other two methods, thresholds were changed subjectively to produce the apparent best results.

5.5 - Discussion and Conclusion

The results show that all three methods have a similar performance. The STM is more useful for off-line applications, where several values might be tried for achieving the best MFE fit. For on-line applications, it will increase the system complexity for the user.

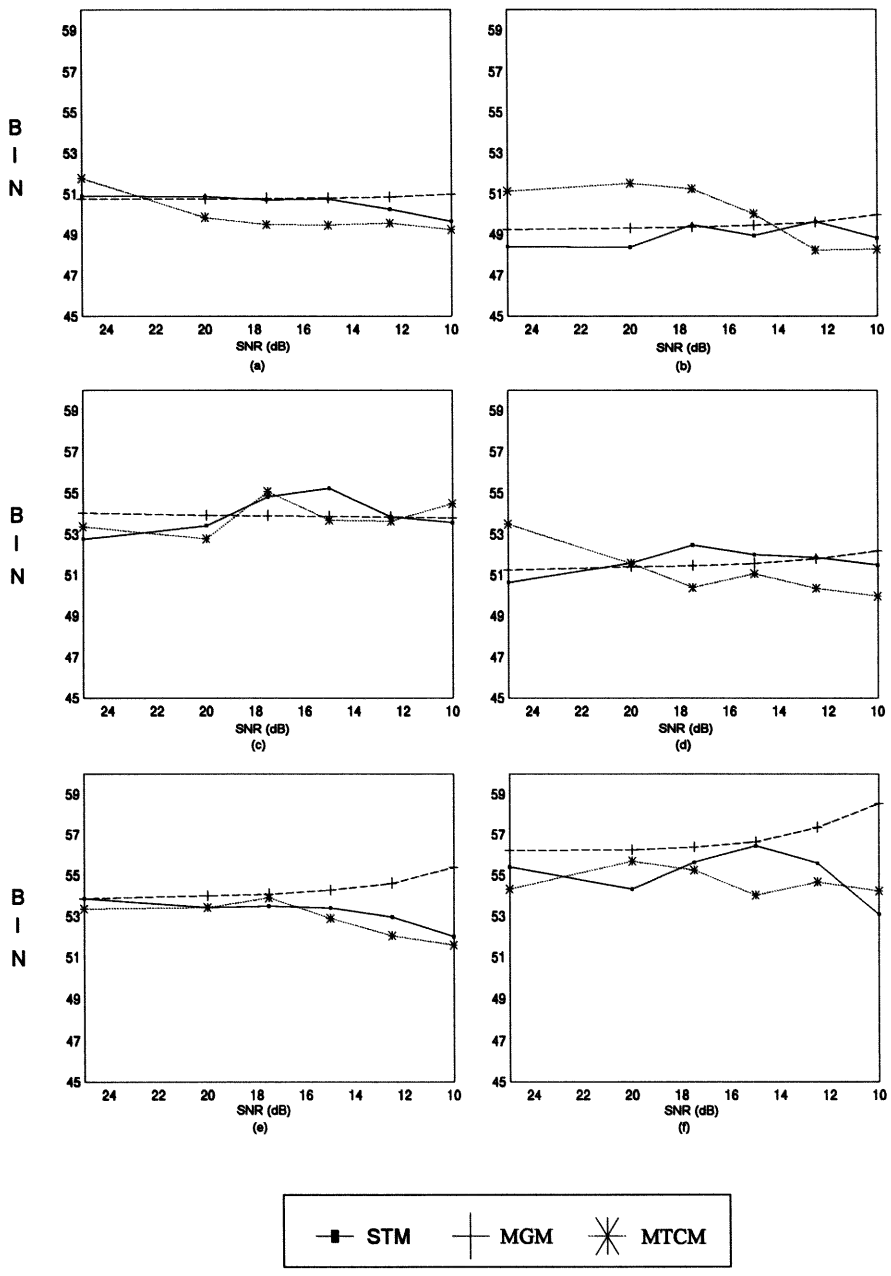

Fig. 5.5 - Bin detections for each of the signals whose spectra is presented in Fig 5.4 at different SNR values. The reference value for all of them is 50.

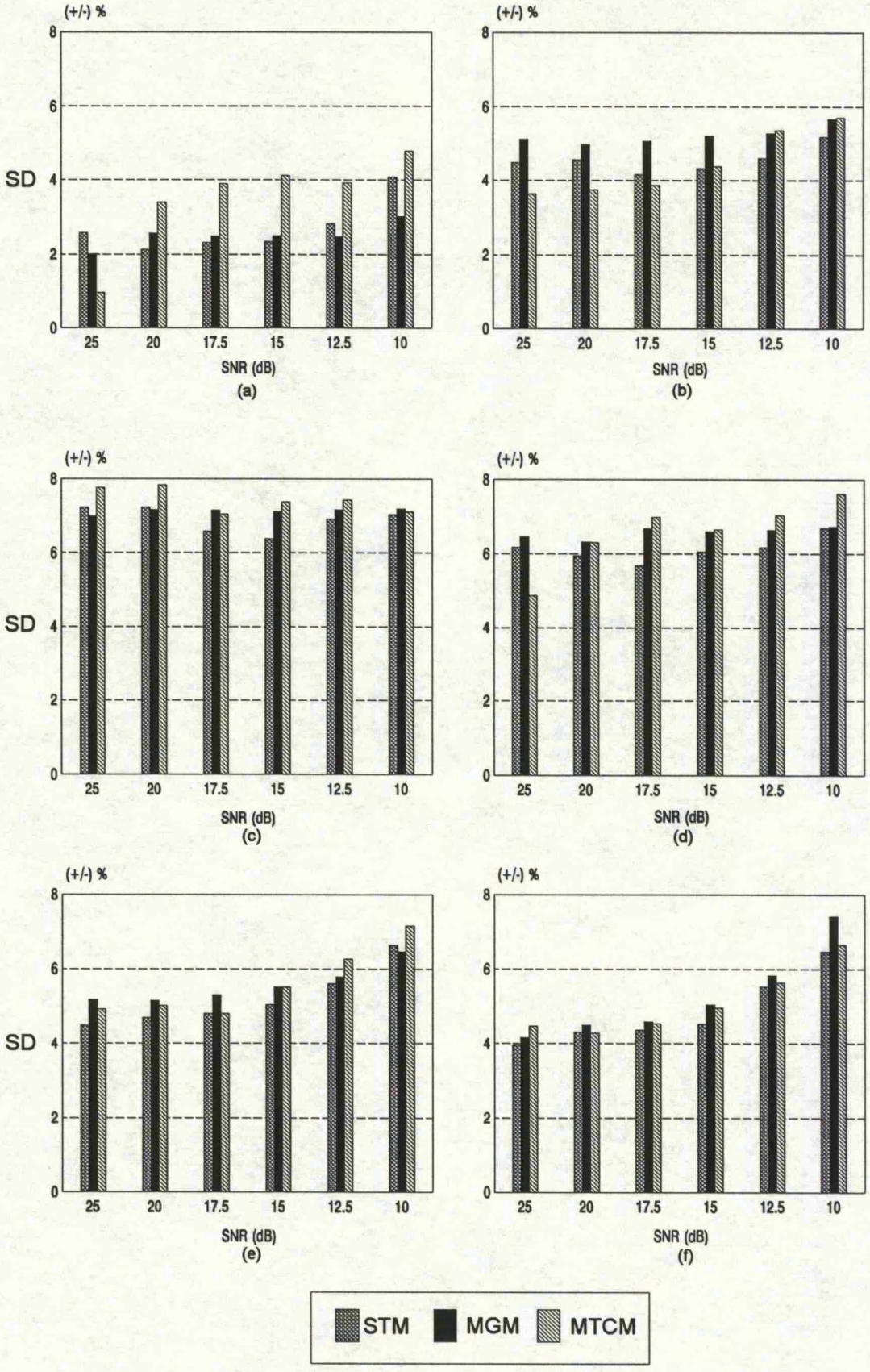

Fig. 5.6 - Standard deviation for the bin detections presented in Fig. 5.4

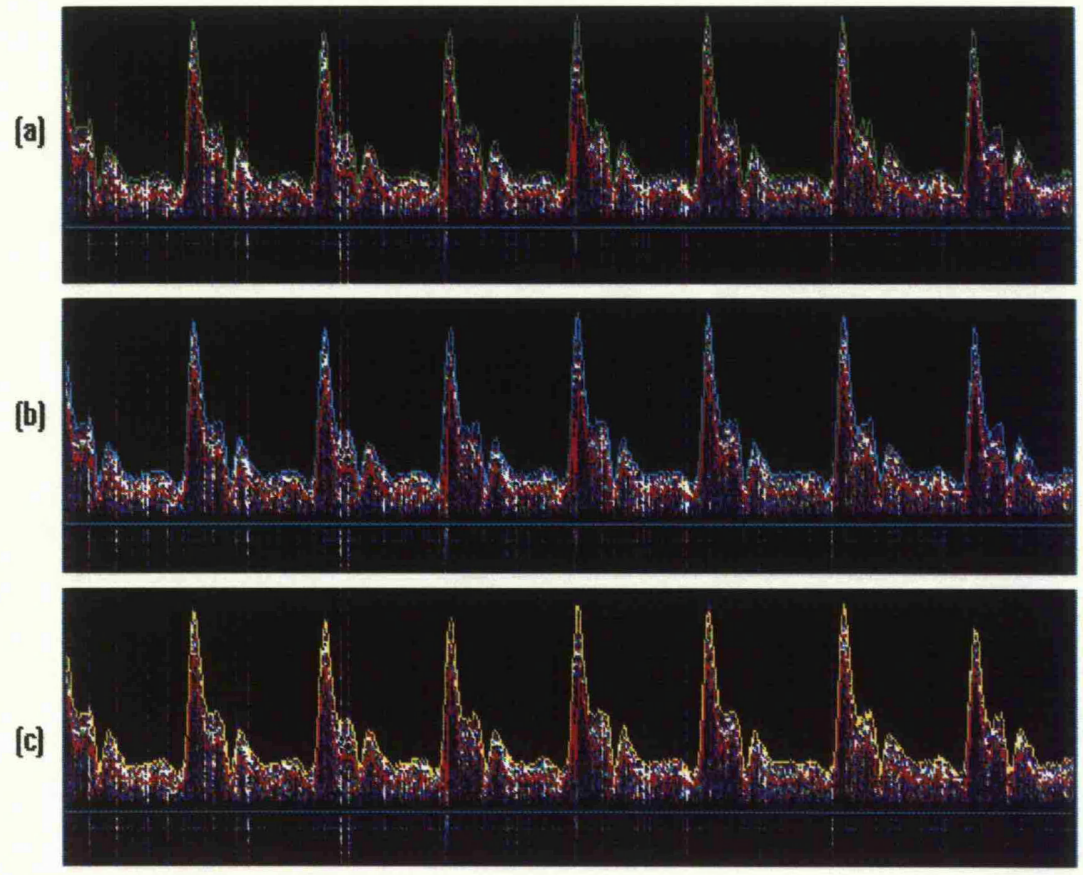

Fig. 5.7 - Maximum frequency envelopes obtained from a Doppler signal recorded from a carotid artery: (a) MGM (b) MTCM (c) STM.

The MTCM has a simpler and faster algorithm than the MGM and may be used where a loss of frequency resolution is acceptable. However, since the constant chosen for a given SNR may not be adequate for another SNR, care should be taken to determine it in order to achieve the best results. It has as advantage over the STM in its capacity to adapt to small SNR changes

The MGM is more suitable for general purpose software which may be used with different Doppler systems and may employ different sampling rates since an evaluation of the level of noise produced by the interaction between computer and a new Doppler system is not necessary. It is a very robust method, totally automatic, having as a disadvantage its higher algorithm complexity when compared to the other methods.

5.6 - Clinical Observations

Based on the discussion above, the software described in Chapter 3 was implemented to detect the MFE in real time using the MGM.

In this implementation, since forward and/or reverse flow may be present, the power of either side of the spectrum is summed and compared to each other. The flow direction is assumed to be the one of the spectrum side that presents larger power. The MFE algorithm is then applied to this side of the spectrum.

Fig. 5.8 shows two practical aspects related to the application of the MGM for the MFE detection of a sonogram obtained during catheterization of a coronary artery. The first one is that the MGM fails when signals of low frequency and high intensity due to the vessel wall movements are present (lower arrow). This produces a non typical ISC curve that leads to a false detection.

The second aspect is that the MGM rejects artefacts due to aliasing at the top of the sonogram (upper arrow). These artefacts occur quite frequently after angioplasty, when the PRF is lower than the Nyquist limit required to sample the highest velocities present in the blood flow. In this situation, according to *in vitro* observations, the MTCM fails to detect the peak of the sonogram, generating a distorted envelope. This occurs because the power generated and used to set the threshold does not relate to the blood flow.

The use of the STM may present similar problem if a threshold, large enough to reject the artefacts, does not provide correct MFE detection.

Beyond this, each time that the catheter is moved to a different site, it is very often necessary to change the sampling rate, the intensity scale for presentation of the

sonogram on the screen, store files and also change the range control of the Doppler unit. It is undesirable to introduce a new control and increase the complexity of the already complex system operation.

Therefore, in spite of the problems mentioned above, the MGM presents useful characteristics and can be successfully used if care is taken to place the catheter within the artery to avoid the detection of wall movements, and/or if the cut-off frequency of the 'wall thump' filters is properly adjusted.

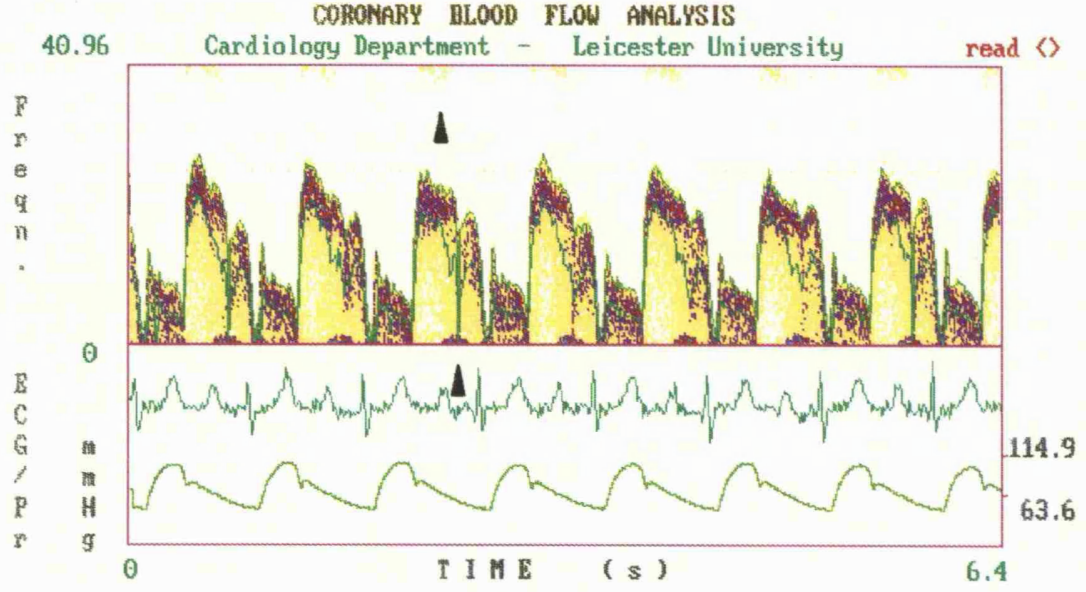

Fig. 5.8 - Example of artefacts present in sonogram obtained from Doppler signals sampled from a coronary artery and the MFE detection with the use of MGM.

Chapter 6 - Effects of Non-uniform Insonation by Catheter-tipped Doppler Transducers on Velocity Estimation

6.1 - Introduction

There are few reported investigations of the errors introduced into velocity estimates obtained using catheter tipped transducers, and these have mainly been concerned with the accuracy of velocity measurements made *in vitro* flow rigs (Tadaoka et al. 1990; Yamagishi et al. 1991). There are two major sources of errors in these measurements. As for the external transducers, the mean and maximum velocity measurements calculated from Doppler signals are dependent on the beam shape produced by the ultrasonic transducer and the degree of vessel insonation (Evans et al. 1989), and in addition the introduction of a relatively large catheter into a coronary artery can both change the average flow and the flow profile, which may also affect the estimate.

This chapter presents analytical, computational and experimental work carried out in order to gain some insight into the velocity estimates obtained with these catheters, characterising their ultrasound beams and their interaction with two different flow profiles.

6.2 - Sample Volume Characterisation

Recalling Chapter 2, the transducer investigated has an annular piezoelectric crystal with outer and inner diameters of 0.8 mm and 0.5 mm respectively. It is driven by a 20 MHz oscillator in 0.4 μsec bursts with a pulse repetition frequency of 62.5 kHz. Since the signal applied to the transducer has a length of 8 cycles, it is possible to use CW solutions to investigate the pressure at different ranges from the catheter tip (Beaver 1974).

The following theoretical calculations deal only with effects produced by the transducer geometry, whilst the experimental measurements reported later are also affected by the Doppler system circuitry.

6.2.1 - Analytical Solution for Beam Shape

The acoustic pressure wave radiated by an element of infinitesimal area, allowing for attenuation by the medium, is given by (Kinsler et al. 1982):

$$p(r',t) = \frac{A}{r'} e^{j(wt-kr')-\alpha r'} \qquad (6.1)$$

where:
A = amplitude of vibration,
r' = distance from the element to the measurement point,
α = attenuation coefficient,
$k = w/c$,
w = angular frequency,
c = the velocity of sound in the medium.

To calculate the acoustic pressure produced by the transducer at any distance r' from its tip, it is necessary to sum the contributions of all its infinitesimal elements.

For a rigid annular piston with the same dimensions as the Doppler catheter, the sum of the contributions given by all elements that belong to its surface is given by (Fig. 6.1):

$$p(r,\theta,t) = A \int_0^{2\pi} \int_a^b \frac{e^{j(wt-kr')-\alpha r'}}{r'} \tau d\tau d\phi \qquad (6.2)$$

where:
r = distance from the centre of the transducer,
r' = distance from a given transducer element,
θ = angle between z axis and r,
a = inner radius,
b = outer radius,
A, α and k are as defined above.

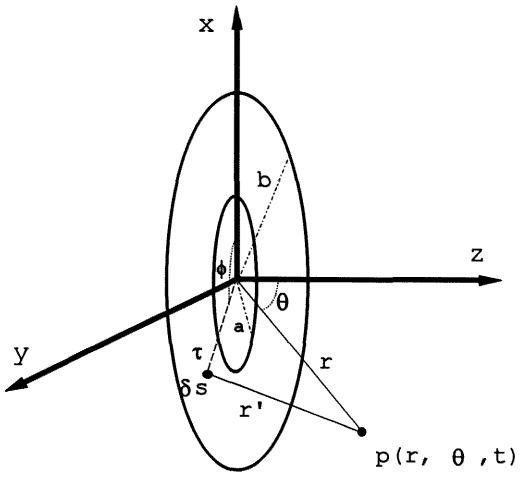

Fig. 6.1 - Geometry used to calculate the beam shape produced by an annular rigid piston.

The axial response for the acoustic beam is found solving Eq. 6.2 for θ equal to zero. Therefore:

$$r' = \sqrt{r^2 + \tau^2}$$

and Eq. 6.2 becomes:

$$p(r,0,t) = 2\pi A e^{jwt} \int_a^b \frac{e^{-(\alpha+jk)\sqrt{r^2+\tau^2}}}{\sqrt{r^2+\tau^2}} \tau d\tau = \frac{2\pi A}{\alpha + kj} e^{jwt} \left(e^{-(\alpha+jk)\sqrt{r^2+a^2}} - e^{-(\alpha+jk)\sqrt{r^2+b^2}} \right)$$

And the pressure amplitude is given by:

$$P(r) = |p(r,0,t)| = \left| \frac{2\pi A}{(\alpha+jk)} \left[\left(G\cos\left(k\sqrt{r^2+a^2}\right) - H\cos\left(k\sqrt{r^2+b^2}\right) \right) + j\left(H\sin\left(k\sqrt{r^2+b^2}\right) - G\sin\left(k\sqrt{r^2+a^2}\right) \right) \right] \right|$$

(6.3)

where:

$G = e^{-\alpha\sqrt{r^2+a^2}}$

$H = e^{-\alpha\sqrt{r^2+b^2}}$.

For a non attenuating medium Eq. 6.3 simplifies to:

$$P(r) = \left| \frac{4\pi A}{jk} \sin\left(\frac{k}{2}\left(\sqrt{r^2+a^2} - \sqrt{r^2+b^2} \right) \right) \right| \qquad (6.4)$$

Fig. 6.2.a presents the normalised results of Eq. 6.4 for the annular piston and those for a circular piston (i.e. $a = 0$) with the same outer diameter as that of the annular transducer. Fig. 6.2.b shows the normalised pressure amplitude for different axial distances calculated from Eq. 6.4 for the annular piston (continuous line), and that given by Eq. 6.3 where attenuation by blood is taken into account (normalised by the maximum value of the previous curve). The attenuation coefficient used for blood at 20 MHz was 5 dB/cm.

At the region close to the transducer, the interference among the acoustic pressures produced by its elements produces a beam fluctuation. This region is named the near field. The region where the beam shows a monotonically decreasing pattern is called far field. The demarcation between these two regions is, for displacements away from the transducer, the last maximum along the axial distance.

A more general equation allows the determination of the pressure amplitude for a distance r much larger than the external radius of the transducer.
For the annular piston at $r >> \tau$ (Fig. 6.1):

$$r' \cong r\left(1 - \frac{\tau}{r}\sin\theta\cos\phi\right)$$

Ignoring the effect of attenuation, Eq. 6.2 may be written as:

$$p(r,\theta,t)=\frac{A}{r}e^{jwt}\int_a^b\int_0^{2\pi}\frac{e^{-jk(r-\tau\sin\theta\cos\phi)}}{1-\frac{\tau}{r}\sin\theta\cos\phi}\tau d\phi d\tau=\frac{A}{r}e^{j(wt-kr)}\int_a^b\int_0^{2\pi}\frac{e^{jk\tau\sin\theta\cos\phi}}{1-\frac{\tau}{r}\sin\theta\cos\phi}\tau d\phi d\tau$$

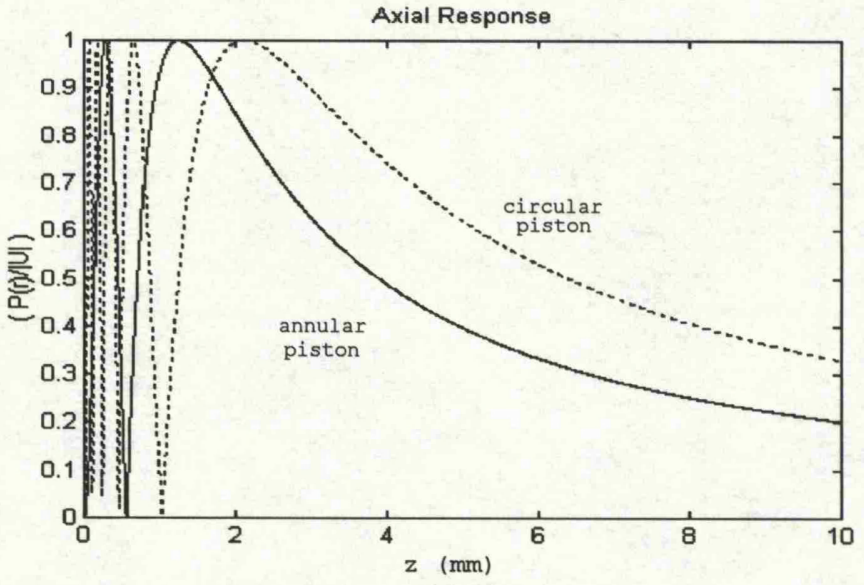

(a)

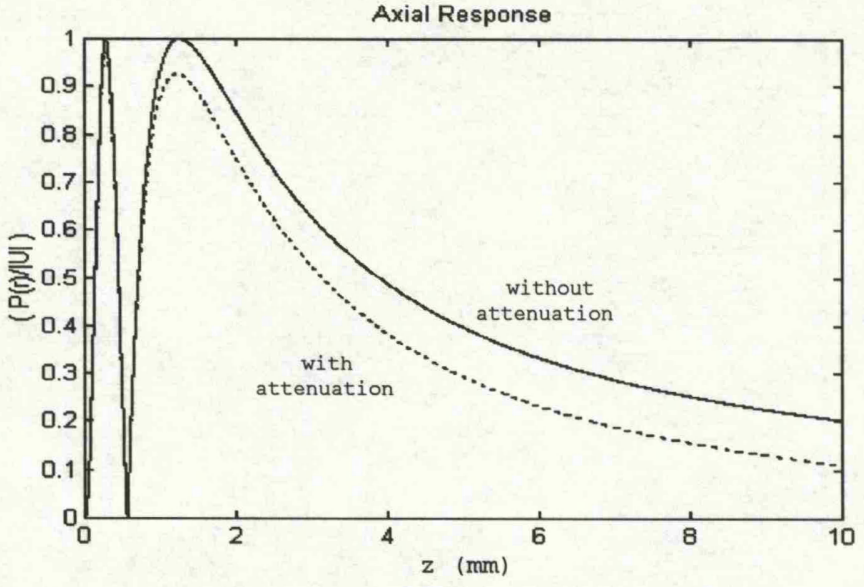

(b)

Fig. 6.2 - (a) Theoretical axial pressure amplitude response for an annular rigid piston with the dimensions of the Doppler catheter (a = 0.25 mm, b = 0.4 mm - continuous line) and a circular piston (broken line) with the radius of 0.4 mm. In neither case has the effect of attenuation been included. (b) Theoretical axial pressure amplitude response for an annular rigid piston with the dimensions of Doppler catheter, accounting for (broken line) and ignoring (continuous line) the attenuation due to blood (estimated for this purpose to be 5 dB/cm).

In the integral, the denominator tends to 1, and, using the following substitutions:

$$J_n(z) = \frac{j^{-n}}{2\pi}\int_0^{2\pi} e^{jz\cos\varphi}\cos(n\varphi)d\varphi$$

$$zJ_1(z) = \int zJ_0(z)dz$$

where J_n is a Bessel function of first kind, order n, the previous equation may be rewritten:

$$p(r,\theta,t) = \frac{2\pi A}{r}e^{j(\omega t-kr)}\int_a^b J_0(k\tau\sin\theta)\tau d\tau = \frac{B}{rk^2\sin^2\theta}e^{j(\omega t-kr)}\int_a^b k\tau\sin\theta J_o(k\tau\sin\theta)k\sin\theta d\tau$$

where $B = 2\pi A$.

The result of the integral is given by:

$$p(r,\theta,t) = \frac{B}{r}e^{j(\omega t-kr)}\left[b^2\left(\frac{J_1(kb\sin\theta)}{kb\sin\theta}\right)-a^2\left(\frac{J_1(ka\sin\theta)}{ka\sin\theta}\right)\right]$$

and the pressure amplitude is:

$$P(r,\theta) = \left|\frac{B}{r}\left[b^2\left(\frac{J_1(kb\sin\theta)}{kb\sin\theta}\right)-a^2\left(\frac{J_1(ka\sin\theta)}{ka\sin\theta}\right)\right]\right| \qquad (6.5)$$

The imposition of a large r was necessary to simplify the integral and to make the analytical solution feasible. An alternative computational approach is presented in section 6.2.2.

The beam pattern obtained from Eq. 6.5 for r equal to 10 mm is shown in Fig. 6.3 (solid line). The beam pattern generated by a circular piston with a diameter of 0.8 mm is also depicted (dashed line).

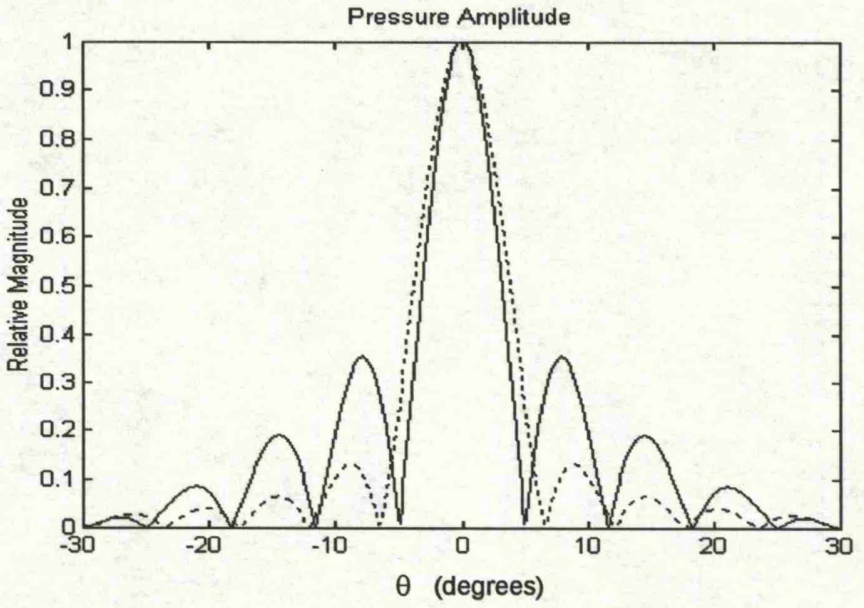

Fig. 6.3 - Theoretical pressure amplitude response for an rigid annular piston with the dimensions of the Doppler catheter (continuous line) and a circular piston of radius equal to 0.4 mm (broken line) at the distance of 10 mm as a function of θ. The effect of attenuation has been ignored

6.2.2 - Numerical Solution for Beam Shape

Eq. 6.5 describes a beam shape at a constant distance r (r much larger than transducer radius) for different angles θ (angle between the point at the distance r and the axis perpendicular to the transducer surface). In order to provide data to evaluate the experimental results without the restriction of a large r, a program was developed to compute the contributions of all crystal elements of small area δs producing the beam shape. In these calculations the value of attenuation used was that for water at 20MHz (0.7 dB/cm) so as to allow comparisons with experimental measurements.

Using Eq. 6.1, the normalised pressure amplitude can be calculated by the discrete sum of the element contributions as:

$$\frac{P(r')}{|A|} = \left| \sum_{0}^{2\pi} \sum_{a}^{b} \frac{e^{-r'(jk+\alpha)}}{r'} \tau \Delta\tau \Delta\phi \right|$$

where (Fig. 6.1):

$r' = \sqrt{z^2 + (x - \tau\cos\phi)^2 + (y - \tau\sin\phi)^2}$

(x, y, z) = the position of the point in the space where the pressure is to be determined.

(τ, ϕ) = the polar co-ordinates of the crystal element whose contribution is being summed.

The results are squared to account for the transmission and receiving characteristics of the transducer.

The pressure amplitude was calculated for three different ranges (z = 4, 5 and 6 mm) at 176 lateral positions symmetrically distributed along the beam centre (from x=-1.76 to x=1.76 mm) to describe the beam pattern. Fig. 6.4 shows these results.

6.2.3 - Experimental Measurements of Sample Volume

As mentioned in Chapter 2, the sample volume of pulsed Doppler systems has a 'teardrop' shape. Eq. 6.5 gives some insight into its shape in the radial direction for the Doppler catheter, but its axial length is defined by the Doppler system circuitry.

Hydrophones have been used to investigate the sample volume of Doppler systems, but can not fully characterise it since it is not possible to assess the effects of the Doppler receiver circuit.

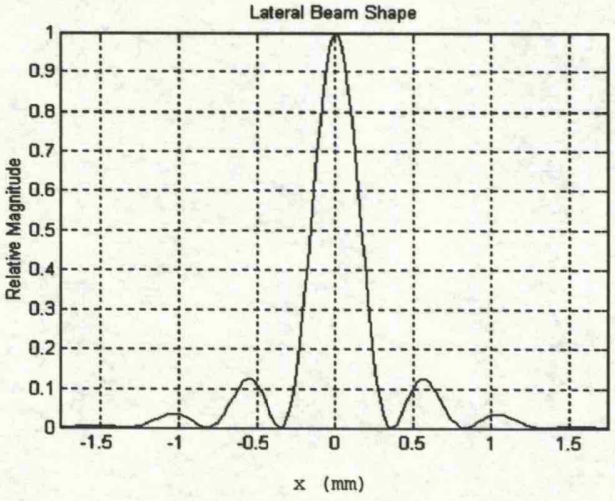

(a)

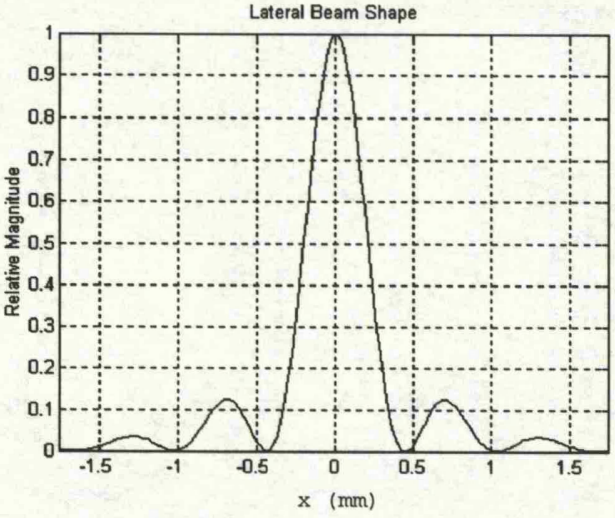

(b)

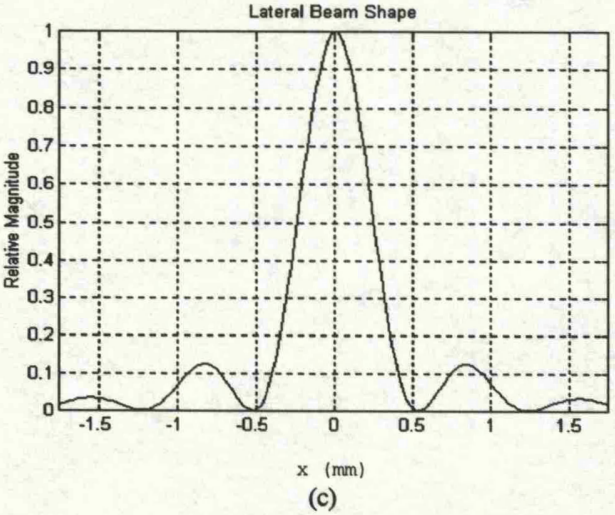

(c)

Fig. 6.4 - Computational results for the lateral beam shape (plotted in terms of relative pressure) along its centre at three different ranges (a) 4 mm, (b) 5 mm and (c) 6 mm. In this case, the effect of the attenuation by water (0.7 dB/cm) was included.

To measure the sample volume of the Doppler catheter along its axial and lateral directions, a system based on the work of Hoeks et al. (1984) was constructed. Fig. 6.5 depicts the experimental set-up. The output of a function generator is amplified to drive a loudspeaker (the circuit of the amplifier utilised is given in Appendix C). The vibration of the loudspeaker membrane is transmitted to a target immersed in degassed water. The transducer is also immersed in the tank and held by a micro manipulator. Where the beam intersects the target, their interaction will produce a Doppler signal whose amplitude is proportional to the beam amplitude. Measurements of the Doppler signal amplitude at several points along either axial and lateral directions allow the determination of the beam shape produced by the Doppler system.

For an object to act as a point source its maximum diameter should be half-wavelength of the acoustic wave (Lee and Furgason 1980). Hoeks et al. (1984) analysed the beam shape produced by a 6.1 MHz Doppler system using, a sphere with a diameter of 0.8 mm as a target. This sphere was attached to a wire whose diameter was 0.01 mm. In this experiment, the signals originating from the interaction between wire and acoustic beam were not significant. In our set-up, a line with a diameter of 0.04 mm ($\cong 0.5\lambda$ of a 20 MHz waveform in water) was used. This choice was dictated by technical constraints of mechanical resistance and manipulation. Unlike the previous work, the signals propagating back from the line were not negligible and therefore, the line itself was used as a target. The effect of the finite target length on the measured pattern was investigated and is discussed in the next section.

The speaker was driven by a 600 Hz sinusoid well above the 300 Hz cut-off frequency of the wall-thump filters. For small amplitude displacements of a target, Doppler signals are subjected to a narrow band tone phase modulation whose main harmonic is at the same frequency as the signal applied to the speaker (Carlson 1986). The relative phase related to the demodulator reference signal is a function

of the distance between the target and the transducer. Displacement of the transducer will further modulate the in-phase and quadrature channels. The amplitude of interest may be calculated from $\sqrt{A_i^2 + A_q^2}$, where A_i and A_q are the amplitude of the in-phase and quadrature signals respectively.

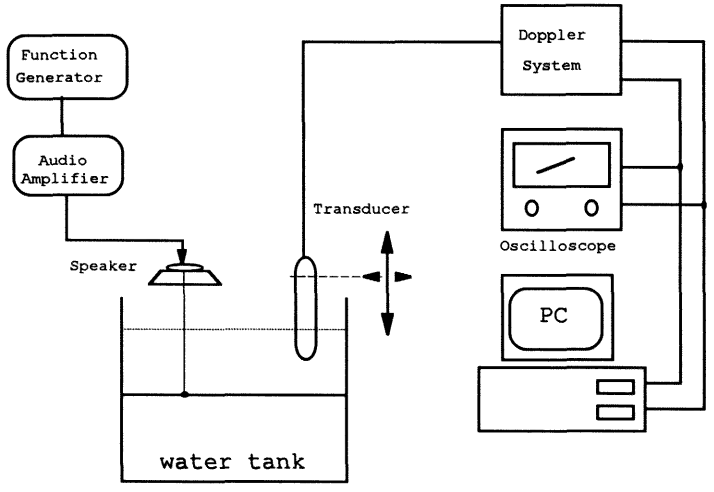

Fig. 6.5 - Schematic diagram of the set-up used for experimental measurements of the catheter beam shape.

The quadrature outputs of the Doppler system were connected to an oscilloscope configured to display in vector-mode. The ultrasound beam centre (assumed to be at the point of the largest Doppler signal amplitude) was found, and the transducer moved again in either axial or lateral direction (according to the particular measurement being made) to a position where no signal was detected. The transducer was then successively displaced in the opposite direction and measurements made until signals were no longer detected.

To determine the Doppler signal amplitude at each point accurately, the in-phase and quadrature signals were digitally sampled at 20480 kHz and a 256 point complex FFT computed. The results from ten time intervals were averaged and the amplitude at the frequency of 600 Hz obtained. The results normalised to the highest amplitude are presented in the Fig. 6.6 and Fig. 6.7. Fig. 6.6 shows the lateral beam shapes at three different gate ranges: 4, 5 and 6 mm (the continuous lines on this figure are theoretical results and will be discussed later). At the range of 6 mm the main lobe width is about 1 mm. Fig. 6.7 shows the axial envelope of the sample volume for the same gate ranges. Adopting 20 dB below the highest pressure response as an arbitrary limit, the axial length is close to 0.7 mm for all three ranges.

6.2.4 - Effect of Target Size

The effect of using a finite target length, rather than a point target, on the experimental results was studied by computing the pressure amplitude for several points equally spaced along the target line (y direction in Fig. 6.1) and then combining these results to predict the effective beam pattern for such a finite target.

For typical sample volume depths (4 to 6 mm), the beam pattern in Fig. 6.3 shows the approximate length of the target which will contribute with significant echoes. Most of the beam power is distributed over an arc of 24° and thus, a set of discrete point sources, whose diameter may be as large as 0.5λ, was used to replace the line segment that corresponds to the arc length (1.7 to 2.52 mm depending on range). The calculation was repeated for different lateral positions (x direction) and the resultant arrays were vectorially summed. Fig. 6.8 depicts the results obtained for 41 points distributed along the line segment at the three different ranges (z = 4, 5 and 6 mm).

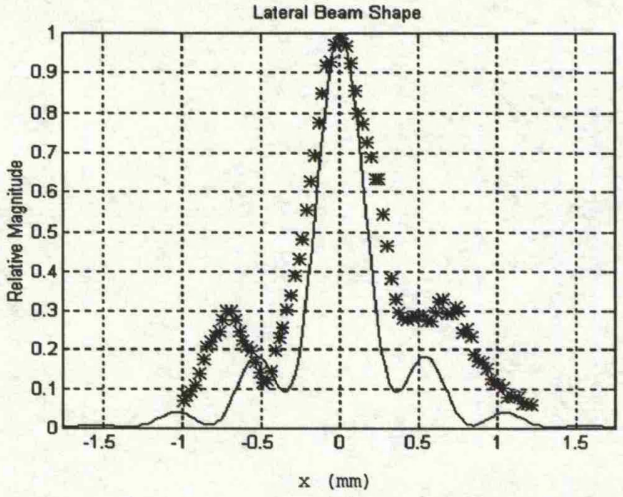

(a)

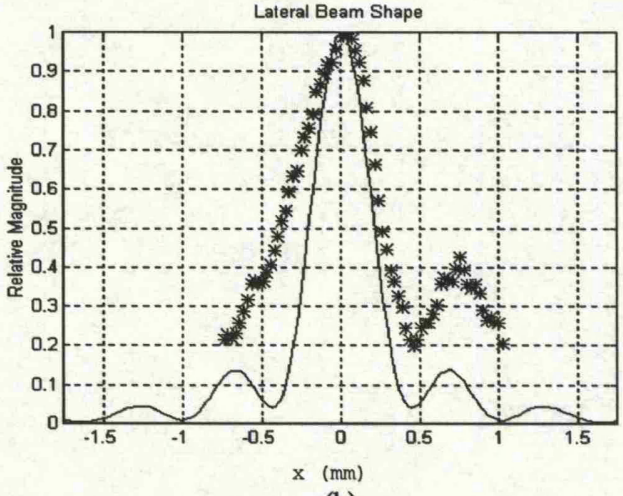

(b)

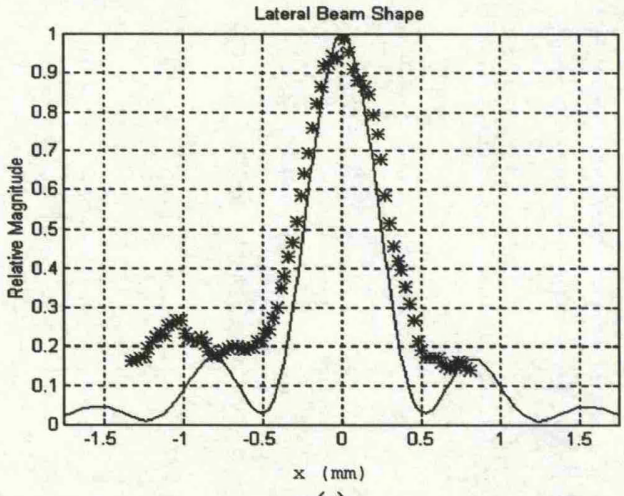

(c)

Fig. 6.6 - Experimental results ('*' points) and computational results (continuous line) for the sample volume lateral shape produced by the Doppler catheter at three ranges in water (a) 4 mm, (b) 5 mm and (c) 6 mm. The results are plotted in terms of pressure responses.

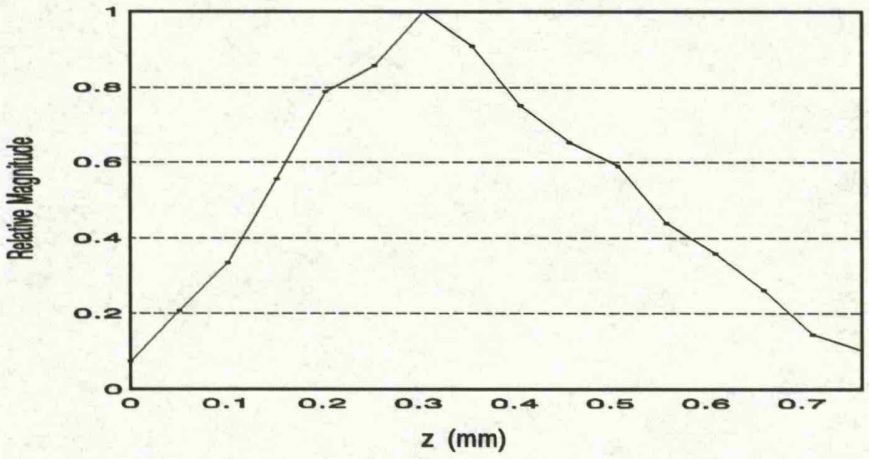

(a)

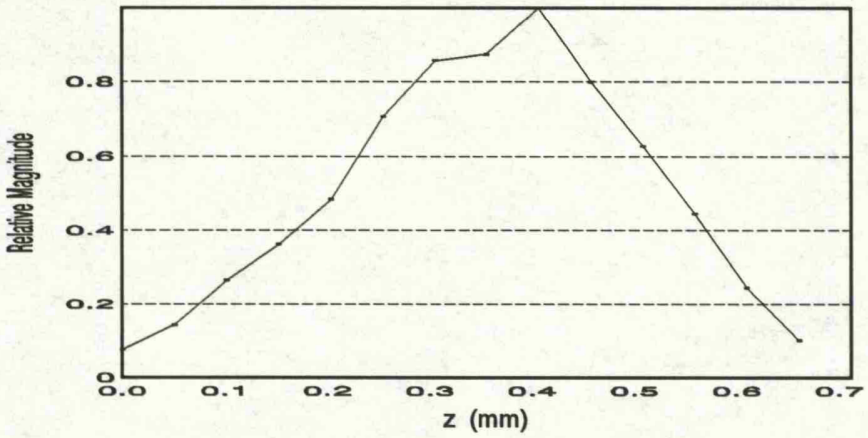

(b)

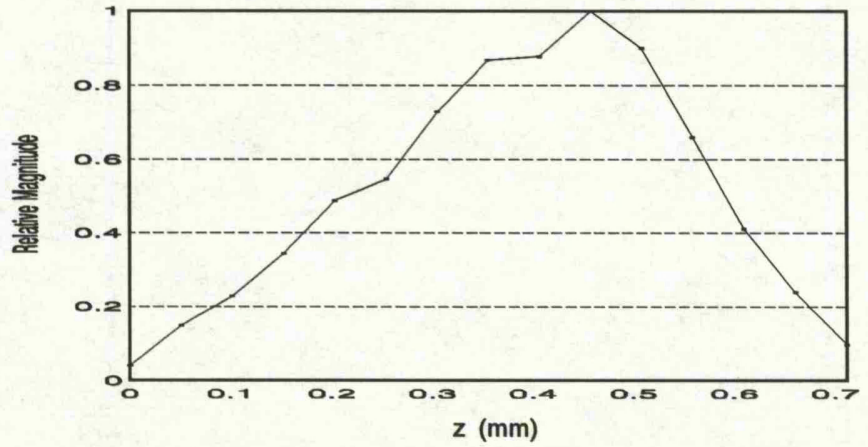

(c)

Fig. 6.7 - Experimental results for the sample volume axial response produced by the Doppler catheter at three ranges in water (a) 4 mm, (b) 5 mm and (c) 6 mm. The results are plotted in terms of pressure responses.

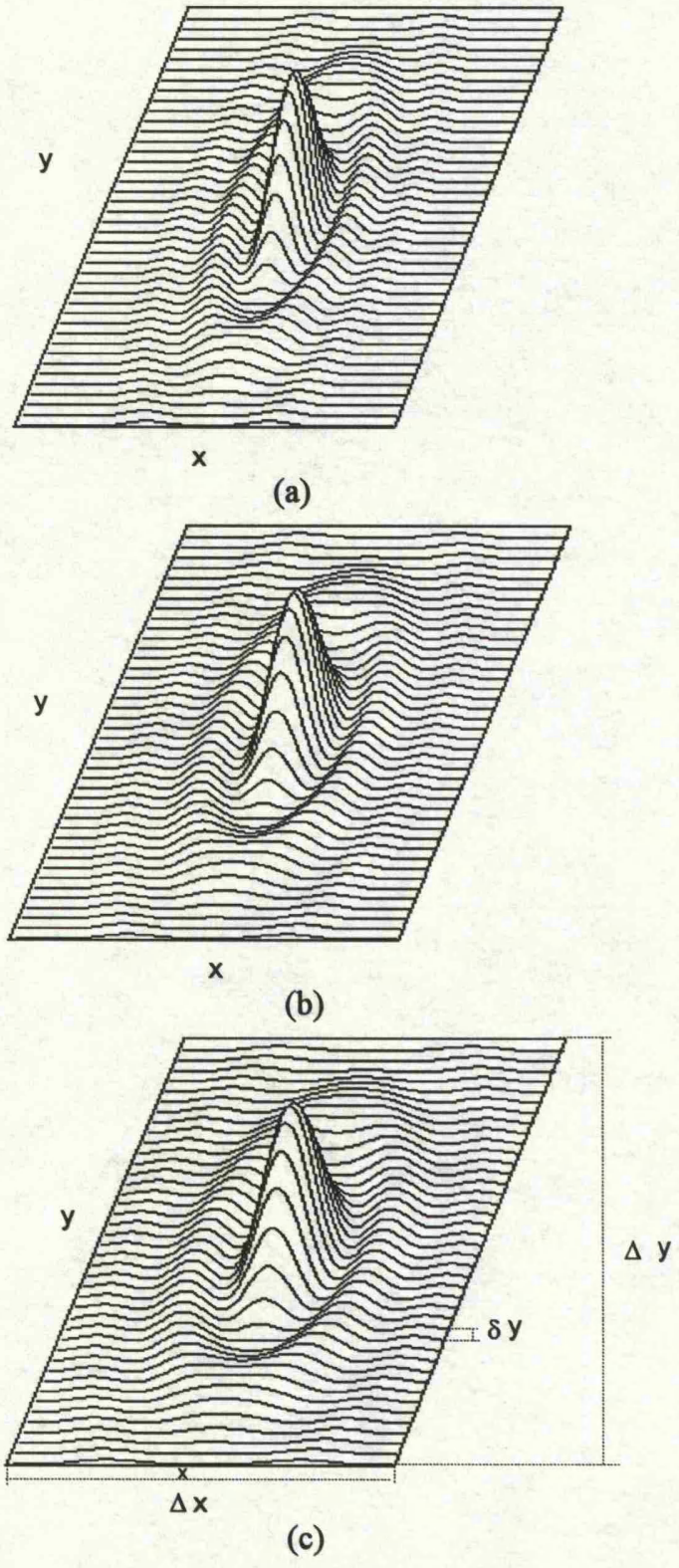

Fig. 6.8 - Computed beam shapes for different points along the line (y) calculated for 176 different lateral positions (x) at three different ranges. Δx is the same for all figures and equal to 3.52 mm. (a) Range = 4 mm, δy = 0.0425 mm, Δy = 1.7 mm. (b) Range = 5 mm, δy = 0.053 mm, Δy = 2.12 mm. (c) Range = 6 mm, δy = 0.063 mm, Δy = 2.52 mm. (Note that the x and y scale are different and therefore the results do not appear to have circular symmetry).

Fig. 6.9 shows the theoretical lateral shape obtained as described above for a finite line target (of 2.12 mm length) at the range of 6 mm (dashed line). This was obtained by vectorially summing the 41 pressure responses shown in Fig. 6.8.c. The continuous line is the same as that in Fig. 6.4.c which corresponds to the response for a single point target displaced along the beam centre. The curves are normalised to their respective maximum values. The finite target length produces side lobes with a higher amplitude relative to the main lobe, but there is no major distortions of the beam shape whose dimensions are being determined. The solid lines on Fig. 6.6 show the computed results for the three ranges superimposed on the experimental ones to allow their comparison.

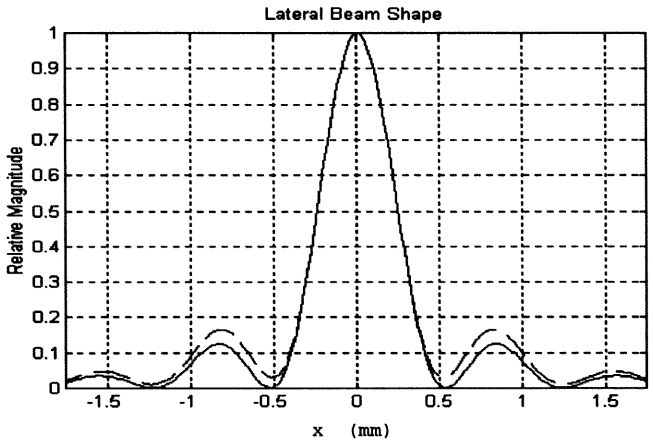

Fig. 6.9 - Effect of interfering multiple echoes from a line target on lateral beam shape at the range of 6 mm. The calculated beam shape for a point target at the beam centre is given by the continuous line and the one that corresponds to the sum of 41 points equally spaced along the target line is given by the broken line. They were both calculated for 176 lateral positions symmetrically distributed along the beam centre.

6.3 - Effect of Beam Shape on Velocity Estimation

The intensity weighted mean frequency (IWMF) of a Doppler signal is defined as (Evans et al. 1989):

$$IWMF = \frac{\int_f P(f) f df}{\int_f P(f) df} \qquad (6.6)$$

where P(f) = Doppler power distribution as a function of frequency. Provided that the entire vessel cross-section is uniformly insonated by an ultrasound beam, then the IWMF is (neglecting other distorting influences such as filtering) proportional to the mean flow velocity, and the latter may be calculated by substituting the former into the standard Doppler equation. If however the vessel is not uniformly sampled by the ultrasound beam this relationship does not hold, and a number of reports have discussed this interaction and its significance on the mean velocity calculation (Evans 1982; Cobbold et al. 1983; Law et al. 1991). In this section, the effects on the intensity weighted mean velocity produced by non-uniform vessel insonation and different flow profiles are explored in the context of the Doppler catheter.

Information concerning velocity profiles distal to a catheter placed in coronary arteries appears to be sparse, and a complete solution would be extremely complex and completely relevant only to the specific geometry investigated and is beyond the scope of this work. Useful insights into the general effects of the non-uniform insonation by the catheter may be gained by considering the velocity profile that would be encountered in the presence of steady flow in a long straight vessel with the catheter either centred in the vessel, or in contact with the vessel wall. In the former case the flow can be thought of as consisting of three regions, the annular flow which must occur around the catheter and up to its tip, the parabolic flow which must occur at large distances downstream from its tip, and the transition zone between the two, where the flow will be much more complex, but will in fact

be the region from which Doppler measurements are made (these intuitive assertions are supported by numerical calculations using the three-dimensional Navier-Stokes equation for axi-symmetric flow carried out by Kagiyama and his colleagues in Japan (1988) and cited by Tadaoka et al. 1990)). In the case where the catheter lies against the vessel wall the situation is even more complex in that the flow profiles no longer have rotational symmetry. In the discussion that follows we will first examine the effects of non-uniform insonation on a parabolic profile, and then consider an 'M' shaped profile.

Parabolic Flow Profile

The velocity distribution for a parabolic flow profile is given by:

$$V(r) = V_{max}\left(1 - \frac{r^2}{R^2}\right) \qquad (6.7)$$

where:
R = vessel radius,
r = distance from any flow lamina to the vessel centre,
V_{max} = maximum flow velocity.

The Doppler power can also be written as a function of the radius. The experimental results obtained in section 6.3 to characterise the beam shape were used to estimate the beam power distribution received by the Doppler system. The experimental points that describe the sample volume main lobe at the range of 6 mm were squared and a Gaussian curve fitted to them (Fig. 6.10). Assuming that the beam shape may be generated by rotating the experimental points around its centre, the Gaussian function describes the received power at any beam point.

The normalised Gaussian power function is:

$$P(r) = e^{\frac{-r^2}{2\sigma^2}} \qquad (6.8)$$

where:
r = distance from the centre to any point,
σ = standard deviation.

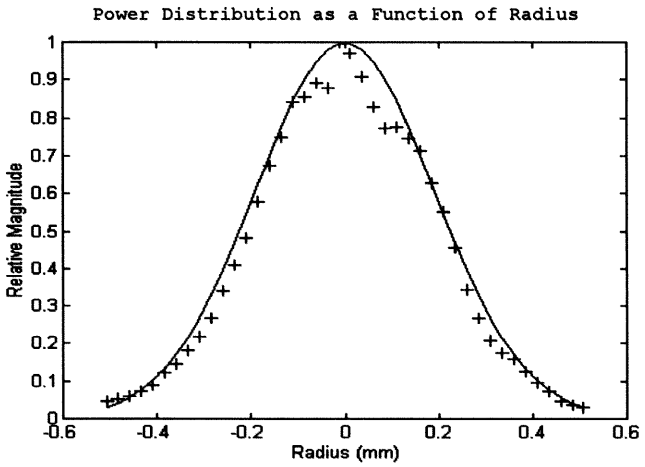

Fig. 6.10 - Gaussian curve fitted to the square of the experimental points that describe the main lobe of the sample volume at the range of 6 mm.

The intensity weighted mean velocity (IWMV) may be written as a function of radius:

$$IWMV = \frac{\int_{\theta}\int_{r} P(r)v(r)r\,dr\,d\theta}{\int_{\varphi}\int_{\varepsilon} P(\varepsilon)\varepsilon\,d\varepsilon\,d\varphi} \qquad (6.9)$$

The relevant geometry for an ultrasound beam with circular symmetry inside a blood vessel is shown in Fig. 6.11. The Gaussian model of the ultrasound beam is clearly only valid for a limited range of r, and therefore to simplify the subsequent calculations it was assumed that any contributions from radii of greater than 0.5

mm, i.e. 2.5σ, were zero. In practise this point corresponds to the width of the main lobe at the 13dB down point.

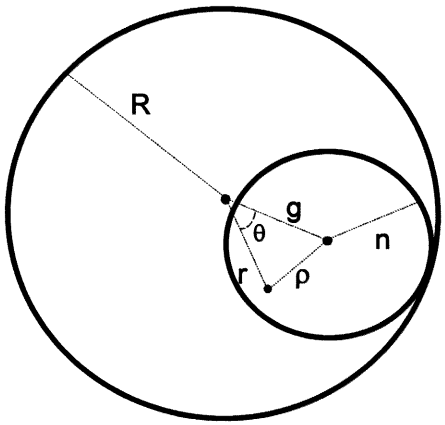

Fig. 6.11 - Geometry of a representative position of the sample volume within a blood vessel. Note that the sample volume at the range of 6 mm is arbitrarily taken to have the same diameter of the catheter. It is assumed that the catheter is parallel to the vessel wall.

From Eqs. 6.7 and 6.8, and noting the geometry presented in Fig. 6.11, Eq. 6.9 may be rewritten as:

$$IWMV = \frac{2V_{max}}{R^2} \frac{\int_0^{\phi}\int_A^B (R^2 - r^2) e^{-\frac{\rho^2}{2\sigma^2}} r\,dr\,d\theta}{\int_0^{2\pi}\int_0^n e^{-\frac{\varepsilon^2}{2\sigma^2}} \varepsilon\,d\varepsilon\,d\varphi} \qquad (6.10)$$

where:

$\rho = \sqrt{r^2 + g^2 - 2rg\cos\theta}$,

$\phi = \cos^{-1}\left(\frac{r^2 + g^2 - n^2}{2rg}\right)$,

r = distance between the vessel centre and any arbitrary point inside the insonated region,
g = distance between the centres of the beam and the vessel,

θ = angle between r and g,
A = g - n;
B = g + n;
R = vessel radius,
n = arbitrary limit of the beam radius (2.5σ).

A program was developed to compute Eq. 6.10 for different σ/R ratios. Fig. 6.12 shows the results obtained for two extreme catheter positions within the vessel i.e. in the centre and adjacent to the wall; in both cases it is assumed that the catheter is parallel to the wall. The results are normalised by the true mean velocity, 0.5Vmax.

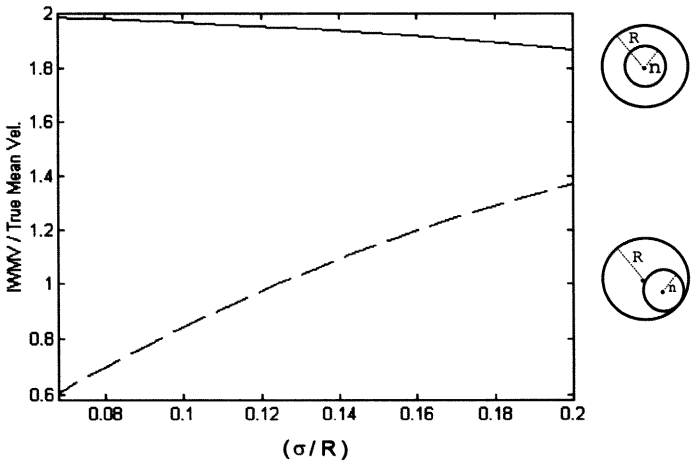

Fig. 6.12 - Effect of non-uniform insonation on the calculated IWMV, as a function of vessel radius, for a sample volume centred in the vessel (continuous line) and adjacent to the vessel wall (dashed line). This figure is based on a parabolic flow profile. σ is the standard deviation of the Gaussian beam and R the vessel radius.

The maximum velocity detected by a frequency follower depends on the 'effective' size of the ultrasonic beam, i.e., in the case of a beam with circular symmetry, the maximum diameter from which adequate signals (detectable by the maximum frequency algorithm) are collected. Fig. 6.13 presents the maximum velocity

intersected by a beam which extends up to the artery wall (dashed line) and one which has the same centre as the vessel (continuous line) as a function of the ratio of the effective beam radius (n) to the vessel radius (R). As previously the results are normalised by the true mean velocity.

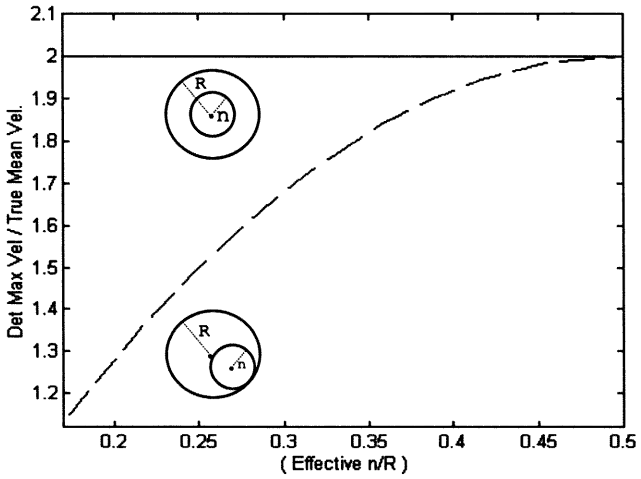

Fig. 6.13 - Maximum velocity of a parabolic flow profile detected by a beam of effective radius n, positioned in the vessel centre (continuous line) and adjacent to the vessel wall (dashed line), for different ratios between effective beam radius (n) and vessel radius (R).

M-shaped Velocity Profile

An arbitrary annular flow distribution which approximates to the profile which might be found distal to the catheter tip is now analysed. A cross-section through the profile is modelled as consisting of two parabolas with maximum velocities at R/2 and zero velocity at the vessel centre and vessel wall, where R is once again the vessel diameter (Fig. 6.14). As for the parabolic flow given by the Eq. 6.7, the proposed profile is normalised by its maximum velocity:

$$v(r) = V_{max} \frac{4}{R^2} r(R-r)$$

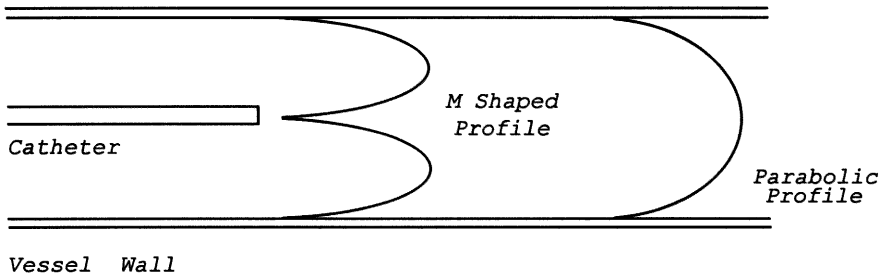

Fig. 6.14 - Schematic diagram of steady flow passing around the catheter and developing an 'M'-shape profile that becomes parabolic at some distance from the catheter tip.

Therefore, IWMV for a Gaussian power distribution is given by:

$$IWMV = \frac{4V_{max}}{R^2} \frac{\int_0^{2\pi} \int_0^n \left(Rr^2 - r^3\right) e^{-\frac{r^2}{2\sigma^2}} dr d\theta}{\int_0^{2\pi} \int_0^n e^{-\frac{\varepsilon^2}{2\sigma^2}} \varepsilon d\varepsilon d\varphi} \qquad (6.11)$$

where n and r are defined above.

The computational results obtained from Eq. 6.11 are presented in Fig. 6.15 for different σ/R ratios. The results are normalised by the true mean velocity of the annular flow, 0.67Vmax. Whilst a somewhat artificial situation the results pertaining to a catheter adjacent to the arterial wall with the same profile are presented on the same figure (a combination of an M-shaped profile and a sample volume adjacent to the wall could conceivably arise due to the catheter not sitting parallel to the axis of the vessel because of either vessel curvature or the catheter being bent).

Fig. 6.16 shows the normalised maximum velocity intersected by a beam of effective radius n for this flow profile in the centre of the vessel (continuous line) and by the wall (dashed line).

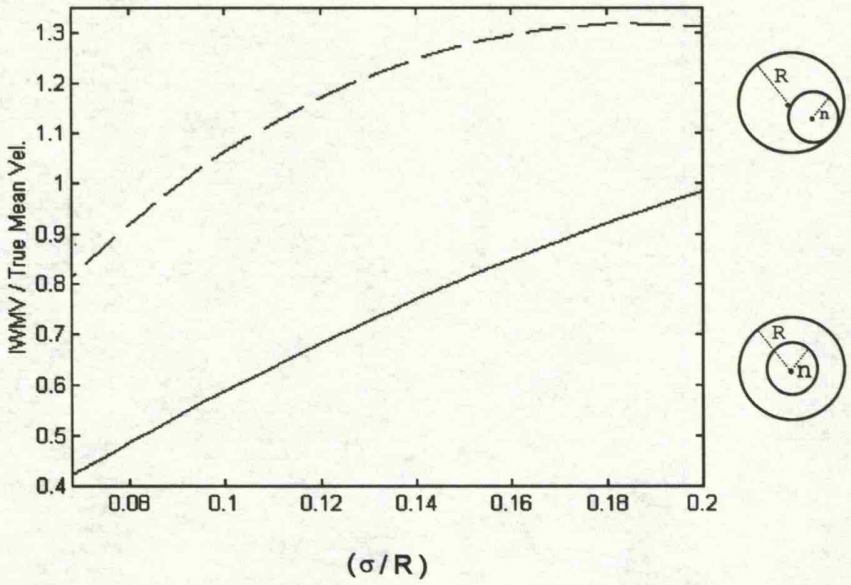

Fig. 6.15 - Effect of non-uniform insonation on the calculated IWMV, as a function of vessel radius, for a sample volume centred in the vessel (continuous line) and adjacent to the vessel wall (dashed line). This figure is based on an 'M' shaped profile. σ is the standard deviation of the Gaussian beam and *R* the vessel radius.

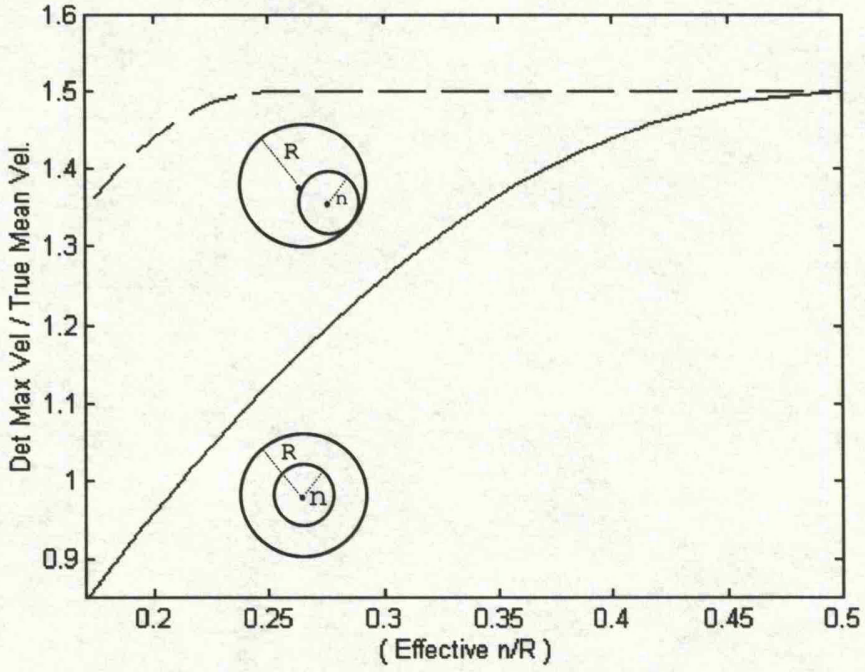

Fig. 6.16 - Maximum velocity of an annular flow profile detected by a beam of effective radius *n*, positioned in the vessel centre (continuous line) and adjacent to the vessel wall (dashed line), for different ratios between effective beam radius (*n*) and vessel radius (*R*).

6.4 - Discussion and Conclusion

The results of the study presented in this chapter emphasise the difficulty of making high quality flow measurements using catheter tipped Doppler transducers, both because the catheter can alter the gross flow and the flow profile by its presence, and because the ultrasound beam is unlikely to insonate uniformly the flow.

From the analytical studies of the beam shape arising from an annular piston, it is seen that the introduction of the lumen into the crystal increases the relative significance of the side lobes but reduces the length of the near field when compared to the results obtained for the circular piston. For the particular annular piston studied here, the near field is contained within a zone extending 1.26 mm from the transducer face.

In practice measurements made with catheter tipped transducers should be taken as far as possible from the catheter tip to avoid effects of the flow disturbances caused by the catheter on velocity estimation, and since our experience shows that the configuration of the coronary arteries seldom allows practical measurements to be made beyond a range of 6 mm, the emphasis in this study has been on ranges of between 4 and 6 mm.

The calculated and measured results shown in Fig. 6.6 are in reasonable agreement and it is thought that the mismatches between the two may be attributed to the limitations of the rigid piston model, the non-homogeneity of the crystal (for instance, due to the weld point) and measurement artefacts.

It is not possible to model accurately the complex velocity profiles that are found in diseased coronary arteries, and thus we have used two very simple profiles to gain some insight into the effects of the interaction between the profile and its changes,

and of the relatively small beam sizes produced by the Doppler catheter. The parabolic profile seems a reasonable model of the average profile that might be found at a distance from the catheter tip, but the 'M' shaped profile is much less realistic. It is in fact easy to calculate the mean component of the flow profile flush with the catheter tip but this clearly changes very rapidly beyond the tip, and of more practical importance, has a central zone of zero velocity which is larger than the effective beam size and cannot therefore be used. The numerical results for velocity profiles distal to catheter tips illustrated by Tadaoka (1990) suggest that the profile close to the tip may be reasonably modelled as 'M' shaped and that as the distance from the catheter tip increases it becomes progressively more parabolic in shape.

Because of the difficulties of modelling the haemodynamic situation in detail the results presented in Figs. 6.12, 6.13, 6.15 and 6.16 can only be used as an aid to understanding errors in catheter tipped measurements in a very general sense, but nevertheless contain some valuable clues to the types of error that may be encountered. The ranges of σ/R and effective n/R values illustrated in the figures correspond to vessels with diameters of between about 2 and 6 mm when the catheter has the dimensions of the Schneider transducer, and thus are typical of the values which might be encountered in coronary arteries (Marcus 1983).

Even for relatively small blood vessels (were the value of σ/R may rise to 0.2) the lateral width of the sample volume does not allow uniform vessel insonation, and whilst the situation appears to improve as the σ/R ratio increases, this only occurs when the transducer itself is large compared with R and the likely gain in accuracy of velocity estimate due to more complete sampling of the velocity profile will be off-set by the interference to flow caused by the catheter.

Perhaps the most disturbing aspect of these results is how susceptible the measurements are to changes in catheter position and velocity profile; which makes

the comparison of velocity measurements before and after an intervention such as angioplasty (where the Doppler catheter will have to be moved unless the balloon is built into the same catheter as the Doppler transducer) very difficult. Even if the catheter remains in the same position, the effect of a change in flow caused by a drug or other intervention, might well be to influence the average velocity profile and thus the relationship between the measured and actual mean velocities.

Although both the IWM and maximum frequency results are influenced by catheter position, vessel size and profile shape, reference to the figures suggests that the output of the maximum follower may be less sensitive to changes in catheter position and flow profile for a given vessel size than the IWM output (note the differences in the ranges of vertical axes) and may therefore be more reliable as a method of quantifying percentage changes in velocity. At large distances from the catheter tip where the velocity profile may be thought of as parabolic, manipulation of the catheter to obtain the maximum possible velocity should improve reproducibility. Whichever follower is used it seems unlikely that accurate measurements of absolute velocity can be made in coronary arteries with a system such as that investigated in this work, although changes in flow might be monitored with some degree of reproducibility.

There is a considerable body of work in the literature which reports the use of zero-crossing detectors in conjunction with catheter tipped Doppler systems. These systems which estimate the RMS frequency are susceptible to many errors (Lunt 1975), and, given the added difficulties due to non-uniform insonation discussed in this chapter which will influence the RMS frequency in a similar way to the IWM frequency, can not be recommended for catheter tipped measurements.

If catheter tipped transducers are to be used to measure mean velocities within vessels with a good degree of accuracy, steps will have to be taken to markedly increase the size of the beams relative to the transducer. In the interim clinical

results obtained with systems such as that studied in this work must be treated with extreme caution.

Chapter 7 - Software for Off-line Analysis of Doppler Signals

7.1 - Introduction

Sonograms are usually obtained by applying FFTs to short-time segments of the Doppler signal, and consecutively displaying their results. This procedure produces information on the temporal changes of the spectral power distribution of the signal. This approach is based on the assumption that for the time window used, the signal is short-time stationary such that each spectral estimate will present a good description of the process under investigation. Therefore, the window should be made short enough to encompass a stationary interval of the signal.

Doppler signals have usually been processed within a time interval of 10 ms (DiMario et al. 1993; Vaitkus et al. 1988). Nevertheless, Kitney and Talhami (1987) have suggested a 2.5 ms time window when the blood flow is disturbed by the presence of stenosis in the vessel. Guo et al. (1993) studying the stationarity of signals recorded from close to the aortic valve have recommended the use of a 5 ms window. However, if the time window used is very short, the frequency resolution will be poor.

With the development of faster processors and DSP techniques, time-frequency distributions have become feasible as tools for the analysis of non-stationary signals, circumventing the trade-off between time and frequency resolution present in the FFT at the expense of more computational time.

As there is no available information on the stationarity of Doppler signals sampled from coronary arteries, a program was implemented to provide a tool for their off-line analysis with better time frequency characteristics than the one described in Chapter 3.

It should be noted that the application of the correct time window allows a better qualitative evaluation of the blood flow but it is unlikely that the use of a slightly larger window will introduce significant errors in the mean and maximum velocity estimation. These two estimates, which are usually used to calculate parameters to assess quantitatively the haemodynamics being investigated, will be affected to a much larger extent by other artefacts (Chapter 6).

The implemented software offers four options:

1 - Data Acquisition
2 - CFFT
3- Wigner Distribution
4 - Choi-Williams Distribution

These topics are discussed in the following sections. Results are presented and discussed.

7.2 - Data Acquisition

This software for off-line analysis was mainly designed to investigate the Doppler signals recorded by the system described in Chapter 3. The files to be read by this software should have the format of the files *.DOP described in Appendix B. Therefore, all the following applications assume that the sampled signals are complex. In order to transform this software into a more general tool, this option was added to sample Doppler signals from directional devices and convert them to complex signals, storing the results, with the patient data, on disk files for posterior analysis.

Signals are sampled at 20.48 kHz from the A/D channel of the DSP board. Each sample is filtered by a delay filter and a FIR Hilbert transform[1] (Fig 7.1). This Hilbert transform is an all-pass filter that produces a phase shift of 90 degree. The delay filter is an all-pass filter with the same number of taps as the Hilbert transform filter used to synchronise the outputs of the two branches of Fig. 7.1. The procedure described, performed by the DSP32C processor, generates complex signals. The results are read by the PC and stored on disk file. The patient data should have been previously inserted by the user through the keyboard to be stored with the sampled data.

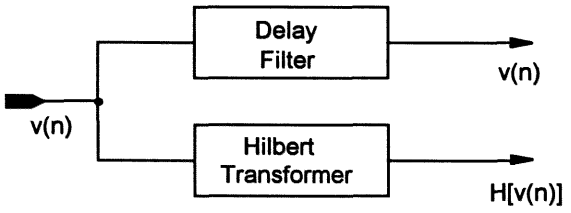

Fig. 7.1 - Diagram representing the generation of analytical signal from real signal using FIR filters.

7.3 - CFFT

In the real-time software (Chapter 3), a new column is added to the sonogram every 12.5 ms. This choice was mainly dictated by the relatively slow speed of the PC

[1]The Hilbert Transform is defined in the time domain by (Carlson 1986):

$$H[x(t)] = \frac{1}{\pi}\int_{-\infty}^{\infty}\frac{x(\lambda)}{t-\lambda}\partial\lambda$$

And its Fourier Transform is:

$$F\{H[x(t)]\} = \begin{cases} -jF\{x(t)\}; f > 0. \\ +jF\{x(t)\}; f < 0. \end{cases}$$

video interface. Other systems described in the literature for coronary studies have similar time window sizes (Doucette et al. 1992; DiMario et al. 1993).

For the recorded data, it is possible to have more flexibility. The software allows the user to select the CFFT size from, in numbers of complex pairs:

1 - 256 (Double zero padding)
2 - 256
3 - 512 (Double zero padding)
4 - 512

Averaging of the CFFT columns are not performed in this software. Therefore, the time window is given by N/Fs where N is the number of pairs of samples and Fs is the sampling frequency.

Double zero padding is a technique used to provide an interpolated transform that improves the determination of the spectral peaks. It consists of adding N zero values to the end of the buffer containing the N data samples. The $2N$ FFT will present for its odd bins, N interpolated FFT values and for its even bins, the original N FFT values (Marple 1987).

The software allows the user to choose between two maximum envelope detectors (simple threshold and modified geometric method) and it also calculates the IWMF. These are plotted on the sonogram after the presentation of each screen that corresponds to 512 columns of CFFT results.

7.4 - Wigner Distribution

The autocorrelation for a sample function of a random process v(t) is defined by:

$$R(t_1, t_2) = E[v(t_1)v(t_2)] \tag{7.1}$$

where E[] stands for statistical expectation operator.

For stationary random processes, the autocorrelation is not dependent on the specific times t_1 and t_2, but their time difference. Eq. 7.1 may be rewritten as:

$$R(\tau) = E[v(t)v(t+\tau)] \tag{7.2}$$

where $\tau = t_2 - t_1$.

For non-stationary processes, Eq. 7.1 can be also rewritten as a function of τ.

Making:

$t_1 = t - \frac{\tau}{2}$ and $t_2 = t + \frac{\tau}{2}$;

then $\tau = t_2 - t_1$ and $t = \frac{t_1 + t_2}{2}$.

Therefore, τ is the time difference and t is the midtime between t_1 and t_2. Replacing them in Eq. 7.1, it is defined for the plane (τ, t) the generalised autocorrelation function (Bendat and Piersol 1986):

$$\Re(\tau, t) = E\left[v\left(t - \frac{\tau}{2}\right)v\left(t + \frac{\tau}{2}\right)\right] \tag{7.3}$$

Using the autocorrelation function, it is possible to define the average power of the stationary random process v(t) by (Carlson 1986):

$$\overline{P} = \int_{-\infty}^{\infty} G(f)\partial f = \int_{-\infty}^{\infty}\int_{-\infty}^{\infty} R(\tau)e^{-j\omega\tau}\partial\tau\partial f \qquad (7.4)$$

where G(f) is the power spectral density.

An estimation of G(f) is the very well know periodogram (Oppenheim and Schaffer 1975).

Similarly, for a non-stationary random process, the power at the instant t may be written as:

$$P(t) = \int_{-\infty}^{\infty}\int_{-\infty}^{\infty} \Re(\tau,t)e^{-j\omega\tau}\partial\tau\partial f = \int_{-\infty}^{\infty}\int_{-\infty}^{\infty} E\left[v\left(t-\frac{\tau}{2}\right)v\left(t+\frac{\tau}{2}\right)\right]e^{-j\omega\tau}\partial\tau\partial f \qquad (7.5)$$

The inner integral in the above equation is called auto-Wigner-Ville distribution (WD) which gives the distribution of instantaneous power over all frequencies:

$$WD(t,f) = \int_{-\infty}^{\infty} E\left[v\left(t-\frac{\tau}{2}\right)v\left(t+\frac{\tau}{2}\right)\right]e^{-j\omega\tau}\partial\tau \qquad (7.6)$$

The cross WD is similarly defined by:

$$WD_{x,y}(t,f) = \int_{-\infty}^{\infty} E\left[x\left(t-\frac{\tau}{2}\right)y\left(t+\frac{\tau}{2}\right)\right]e^{-j\omega\tau}\partial\tau \qquad (7.7)$$

Integrating Eq. 7.6 from t=-∞ to t=∞, it is possible to determine the autospectral density function for a particular frequency:

$$S_w(f) = \int_{-\infty}^{\infty} WD(t,f)\partial t \qquad (7.8)$$

The total signal energy is obtained by integrating Eq. 7.8 for all frequencies.

This approach tries to clarify the relation between WD, spectral density, and power and shows that the WD can be seen as a generalisation of the periodogram.

Another approach would be the use of Cohen's class of time-frequency distributions. Cohen (1966) has shown that an infinite number of time-frequency distributions can be generated from a more generic equation given by:

$$P(t,w) = \frac{1}{4\pi^2}\iiint e^{-j(\theta t+\tau w-\theta u)}\phi(\theta,\tau)s\left(u+\frac{\tau}{2}\right)s^*\left(u-\frac{\tau}{2}\right)\partial u\partial\tau\partial\theta \qquad (7.9)$$

('*' denotes complex conjugate and all integral ranges are from -∞ to ∞)

where Φ(τ,θ) is an arbitrary function called kernel which satisfies:

$$\Phi(0,\theta)=\Phi(\tau,0)=1$$

By choosing different kernels, different time-frequency distributions are derived. They will present their own properties and diversified behaviour. The WD is obtained by making the kernel in Eq. 7.9 equal to 1.

7.4.1 - Implementation of WD

A discrete-time estimator for the WD (DTWD) is given by Claasen and Mecklenbrauker (1980):

$$DTWD(n,w_n) = 2\sum_{k=-\infty}^{k=\infty} v(n+k)v^*(n-k)e^{-j2w_n k} \qquad (7.10)$$

where '*' denotes conjugate complex (This is an extension of the concept presented by Eq. 7.6. The use of complex signals has mathematical convenience and can be used to code information (Chapter 3)).

It can be seen from Eq. 7.10 that the DTWD has a period of π due to the multiplying factor of two in the exponential. Since any signal spectrum is defined in a interval of 2π, aliasing will occur. There are two approaches to avoid distortions produced by this aliasing: oversampling and the use of analytical signals.

Oversampling, by at least a factor of two (two times the Nyquist rate), basically keeps the signal spectrum to half of the frequency scale avoiding possible distortions.

A real FFT produces redundancy of information for the negative frequencies and these frequencies will superimpose the DTWD results on the positive spectrum if the signals are sampled at the Nyquist rate. This drawback can be eliminated by the use of analytical signals. The analytical signal *z(n)* for the sampled random process *v(n)* is defined as:

$$z(n) = v(n) + jH[v(n)] \qquad (7.11)$$

where H[] is the Hilbert transform operator.

The analytical signal spectrum is given by:

$$Z(w)=\begin{cases}2V(w), 0<w<\pi\\ V(w), \quad w=0\\ 0, \qquad -\pi<w<0\end{cases}$$

where $Z(w)$ and $V(w)$ are the Fourier transforms of $z(n)$ and $v(n)$ respectively.

Therefore, by generating analytical signals as shown in Eq. 7.11, the negative side of the spectrum, and consequently the distortions, are removed.

For computational purposes it is necessary to window the DTWD in the time domain. Eq. 7.10 becomes the so-called discrete pseudo WD (DPWD):

$$DPWD(n,w_n)=2\sum_{k=-N+1}^{k=N-1}h(k)h^*(-k)v(n+k)v^*(n-k)e^{-j2w_nk} \tag{7.12}$$

Martin and Flandrin (1985) have suggested that Eq. 7.12 can be rewritten in a more efficient computational form:

$$DPWD(n,w_n)=2\sum_{k=-N+1}^{k=0}h(k)h^*(-k)v(n+k)v^*(n-k)e^{-j2w_nk}+2\sum_{k=0}^{k=N-1}h(k)h^*(-k)v(n+k)v^*(n-k)e^{-j2w_nk}-2|v(n)|^2 \therefore$$

$$DPWD(n,w_n)=4\,\mathrm{Re}\left[\sum_{k=0}^{k=N-1}h(k)h^*(-k)v(n+k)v^*(n-k)e^{-j2w_nkT}\right]-2|v(n)|^2 \tag{7.13}$$

Eq. 7.13 basically reduces the number of computational evaluations by half when compared to Eq. 7.12. It is possible to use FFT algorithms to calculate Eq. 7.13 by neglecting the power of two in the exponential that stands for a scaling factor in the frequency axis and replacing w_n by $2\pi n/N$. The results of Eq. 7.13 are real. Actually, this is a WD property, that is, the WD of any function, real or complex, is real (Claasen and Mecklenbrauker 1980).

In terms of practical implementation of the WD for Doppler signals stored as described in Appendix B, it should be remembered that they are modulated in quadrature form to provide directional information, having real and imaginary components. Therefore, the only possible approach to avoid aliasing is the use of oversampling. Since there is a maximum sampling rate in the system developed, it is not always possible to achieve this. Another disadvantage of this approach is the reduction of the time interval that is possible to record because the maximum file size is 640 kbytes for any of the sampling rates (Chapter 3).

Doppler signals recorded from arteries presenting only forward flow can be considered encoded as described by Eq. 7.11, since the quadrature channel is not providing any useful information about flow direction. For these cases (the majority of the coronary arteries) no oversampling is necessary and the analytical encoding by hardware saves computational time to calculate their DPWD.

Considering Eq. 7.13, since the dc component does not have physical significance in medical ultrasound ('wall thump' filters in Doppler systems usually have cut off frequencies below 300 Hz), the second term of that expression works just as a scaling factor. Therefore, its subtraction, together with the multiplication by 4 of the first term, can be neglected since the interest is in the relative intensities of the frequency components.

Based on these considerations, the following algorithm was implemented, where Δm is the number of sample pairs (real and imaginary) between the successive DPWD calculations:

1- ask the user to define Δn.

2 - retrieve 2N complex sampled data points from the disk file. Store them in a data buffer.

3 - apply a complex Hann window (2N points):

hv(k)=h(k)v(k); for *k*=-N+1,N-1; where *n*=0 (E. 7.13) corresponds to the window centre.

Store results in processing buffer.

4 - calculate the inner product from the windowed data: *hv(k)hv*(-k)*, for *k*=0,N-1.

5 - apply a complex FFT (N points).

8 - display the modulus of the real values of the CFFT results on the screen with scaled magnitudes.

7 - shift the last (2N - Δn) complex samples to the beginning of the data buffer.

9 - retrieve Δn complex sampled data points from the disk file. Store the new data at the end of data buffer. Go to 3.

Steps 1, 2 and 9 are executed by a 486 PC with software written in 'C' language. The other steps are performed by a DSP board with software written in Assembly language.

The minimum time resolution is 1/Fs, where Fs is the sampling frequency. N was set to 256. The frequency resolution is constant and equal to Fs/N.

7.5 - Choi-Williams Distribution

Let a signal be given by the composition of two sinusoids:

$$h = f + g = e^{jw_1 t} + e^{jw_2 t}$$

Applying DTWD to it:

$$DTWD_h(n,w) = 2\sum_{k=-\infty}^{k=\infty}\left(e^{jw_1(n+k)} + e^{jw_2(n+k)}\right)\left(e^{-jw_1(n-k)} + e^{-jw_2(n-k)}\right)e^{-j2kw} \therefore$$

$$DTWD_h(n,w) = 2\sum_{k=-\infty}^{k=\infty}\left(e^{jw_1(n+k)}e^{-jw_1(n-k)}\right)e^{-j2kw} + 2\sum_{k=-\infty}^{k=\infty}\left(e^{jw_2(n+k)}e^{-jw_2(n-k)}\right)e^{-j2kw} +$$

$$+2\sum_{-\infty}^{\infty}\left(e^{jw_1(n+k)}e^{-jw_2(n-k)}\right)e^{-j2kw} + 2\sum_{-\infty}^{\infty}\left(e^{jw_2(n+k)}e^{-jw_1(n-k)}\right)e^{-j2kw}$$

Therefore:

$$DTWD_h = DTWD_f + DTWD_g + 2\,\mathrm{Re}\{DTWD_{f,g}\} \qquad (7.14)$$

where $DTWD_{f,g}$ is the cross DTWD between the two signals.

The result of Eq. 7.14 can be generalised. If a signal is composed of several components as:

$$h(t) = \sum_{l=1}^{n} h_l(t)$$

Its DTWD is given by:

$$DTWD_h = \sum_{i=1}^{n} DTWD_{h_i} + \sum_{j}\sum_{m} DTWD_{h_j,h_m}, \text{ for j}\neq\text{m.} \qquad (7.15)$$

As can be seen, the DTWD of a signal is not given by the sum of the DTWD of its components. This result is also valid for the WD. Due to this property, the WD is classified as a bilinear function. The second term in Eq. 7.15 is called the cross term. Flandrim (1984) has pointed out that this term appears in the time-frequency plane at a distance from the monocomponents that is related to their position, but not close to them. The presence of cross terms may obscure the interpretation of the signal analysed since they do not have any physical meaning.

Based on time-frequency distributions of Cohen's class (Eq. 7.9), Choi and Williams (1989) proposed another distribution to decrease the interference effect among the different signal components.

A new kernel was defined by:

$$\phi(\theta,\tau) = e^{\frac{-\theta^2\tau^2}{\sigma}} \tag{7.16}$$

where σ is a scaling factor.

Replacing this kernel in Eq. 7.9 and integrating over θ, the so-called Choi-Williams distribution (CWD) is obtained:

$$CWD(t,w) = \int_{-\infty}^{\infty} e^{-jw\tau} \int_{-\infty}^{\infty} \sqrt{\frac{\sigma}{4\pi\tau^2}} e^{\frac{-\sigma(u-t)^2}{4\tau^2}} s\left(u+\frac{\tau}{2}\right) s^*\left(u-\frac{\tau}{2}\right) \partial u \partial\tau \tag{7.17}$$

As can be seen from Eq. 7.17, the introduction of the kernel assigns different weights to the inner product of the function ***s***. Higher weights are given for ***u*** close to ***t*** and lower weights when ***u*** is far from ***t***. Therefore, the cross terms present in the time-frequency plane are smoothed out by the application of this kernel, since they are not close to the monocomponents.

Analysing the effect of the parameter σ for a multicomponent chirp signal, Choi and Williams (1989) concluded that a large σ increases the auto-term resolution, but also reinforces the cross terms. Therefore, there is a trade-off between the auto-term resolution and cross term suppression. Based on their experimental results, the use of a value between 0.1 and 10 is recommended for the parameter σ.

7.5.1 - Implementation of CWD

The discrete version of Eq. 7.17, called the discrete CWD (DCWD), is (Choi and Williams 1989):

$$DCWD(n,w_n) = 2\sum_{k=-N}^{k=N} e^{-j2w_n k} \sum_{u=-M}^{u=M} \sqrt{\frac{\sigma}{4\pi k^2}} e^{\frac{-\sigma u^2}{4k^2}} s(n+u+k)s^*(n+u-k) \qquad (7.18)$$

As for the DTWD, the DCWD is real valued and periodic for π. Therefore, oversampling or the use of analytical signals must be considered to avoid aliasing.

Eq. 7.18 can be simplified for computational use. Considering the application of a non rectangular time window and changing the order of the summation operators:

$$DCWD(n,w_n) = 2\sum_{u=-M}^{u=M} \sum_{k=-N}^{k=N} \sqrt{\frac{\sigma}{4\pi k^2}} e^{\frac{-\sigma u^2}{4k^2}} h(k)h^*(-k)s(n+u+k)s^*(n+u-k)e^{-j2w_n k}$$

$$DCWD(n,w_n) = 2\sum_{u=-M}^{u=M} \left(\begin{array}{l} \sum_{k=-N}^{k=0} \sqrt{\frac{\sigma}{4\pi k^2}} e^{\frac{-\sigma u^2}{4k^2}} h(k)h^*(-k)s(n+u+k)s^*(n+u-k)e^{-j2w_n k} + \\ \sum_{k=0}^{k=N} \sqrt{\frac{\sigma}{4\pi k^2}} e^{\frac{-\sigma u^2}{4k^2}} h(k)h^*(-k)s(n+u+k)s^*(n+u-k)e^{-j2w_n k} \end{array} \right) - |v(u,n)|^2$$

$$DCWD(n,w_n) = 2\sum_{u=-M}^{u=M} \left(2\,\mathrm{Re}\left[\sum_{k=0}^{k=N} \sqrt{\frac{\sigma}{4\pi k^2}} e^{\frac{-\sigma u^2}{4k^2}} h(k)h^*(-k)s(n+u+k)s^*(n+u-k)e^{-j2w_n k} \right] \right) - 2\sum_{u=-M}^{u=M} |v(n+u)|^2$$

By restoring the summation operator order:

$$DCWD(n,w_n) = 4\,\mathrm{Re}\left[\sum_{k=0}^{k=N}\left(\sum_{u=-M}^{u=M}\sqrt{\frac{\sigma}{4\pi k^2}}e^{\frac{-\sigma u^2}{4k^2}}h(k)h^*(-k)s(n+u+k)s^*(n+u-k)\right)e^{-j2w_n k}\right] - 2\sum_{u=-M}^{u=M}\left|v(n+u)\right|^2$$

(7.19)

For the reasons mentioned in Section 7.4.1, the second term of Eq. 7.19 and the multiplication by 4 in the first term are not taken into account in this implementation. The power of two in the exponential is again neglected in order to apply FFT routines. The displacement in numbers of samples (Δn) between the distribution computation and the parameter σ must be defined by the user at the start of the program. Since the weights to be assigned to the inner product are used in a repetitive way, they are calculated just once and stored in a look up table to speed up the execution of the program. The algorithm implemented can be described by the following steps:

1 - ask the user to define σ and Δn.

2 - generate weights:

$GW(u,k) = \sqrt{\frac{\sigma}{4\pi k^2}}e^{\frac{-\sigma u^2}{4k^2}}$, for u=0,M; k=0,N-1; store them in a look up table.

3 - retrieve 2N complex sampled data points from disk file. Store them in processing buffer.

4 - apply a complex Hann window (2N points):

$hs(k)=h(k)s(k)$; for k=-N+1,N-1; where n=0 (Eq. 7.19) corresponds to the window midpoint.

Store results in processing buffer.

5 - shift the last 2M arrays in data buffer of 2M+1 arrays to the first 2M positions.

6 - calculate the inner product from windowed data:

$hs(u,k) = hs(u+k)hs^*(u-k)$, for k=0,N-1.

Store results in the last 2M+1 arrays of data buffer.

7 - if the number of arrays stored is smaller than 2M+1, go to 9.

8 - with the use of the lookup table and the data buffer, calculate:

$\sum_{u=-M}^{u=M} GW(u,k)hs(u,k)$, for k=0,N-1.

Store results in processing array.

9 - apply a complex FFT (N points). Store them in processing buffer.

10 - display the modulus of the real values of the complex FFT results on the screen with scaled magnitudes.

11 - retrieve 2N complex sampled data spaced 2Δn positions (real and imaginary data) from the beginning of the last reading operation in disk file. Store the new data in the processing buffer. Go to 4.

Steps 1, 2, 3, 10 and 11 are executed by a 486 PC with software written in 'C' language. The other steps are performed by a DSP board with software written in Assembly language. As for DPWD, the minimum time resolution is 1/Fs, and the frequency resolution is equal to Fs/N. N was set to 256 and M to 4.

To illustrate the features of the DPWD and DCWD, Fig. 7.2 displays the results of applying both distributions for a short segment of an ECG signal.

Comparing the sampled signal (at the lower part of Figs. 7.2.a and 7.2.b) with the corresponding time-frequency distribution, it can be seen that the DPWD produces a 'ghost' QRS complex due to the cross terms. For the DCWD, the cross terms are smoothed and the distribution can be more easily interpreted.

7.6 - Examples and Discussion

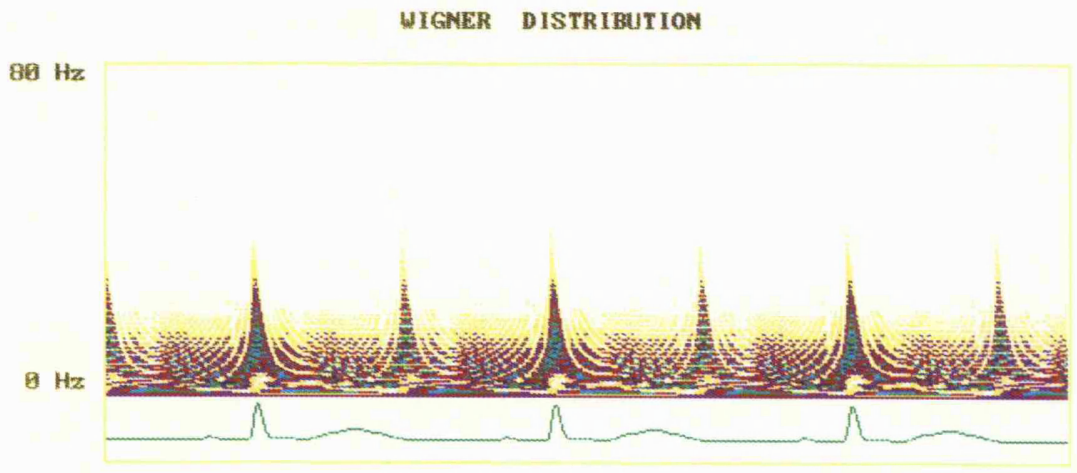

(a)

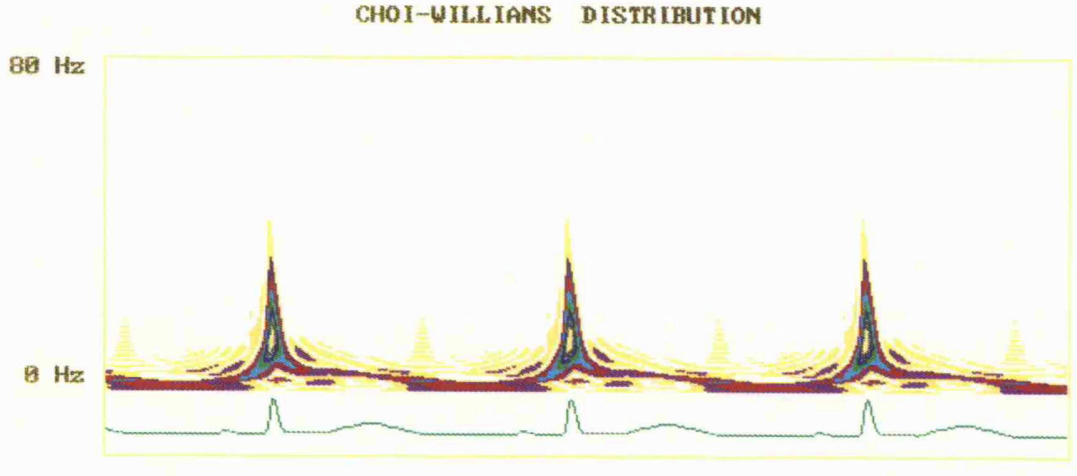

(b)

Fig. 7.2 - (a) DPWD and (b) DCWD of a ECG signal. The ECG signal was sampled at 160 Hz after filtering by an anti-aliasing filter set to 40 Hz. The Hilbert transform is used to generate analytical signals before the computation of the distributions. N = 256 and Δn = 1 for both distributions. For DCWD, $\sigma = 6$, M = 4.

Fig 7.3 shows CFFT, DPWD and DCWD results for a recorded Doppler signal sampled from a coronary artery. Details about the way in which they were obtained is given in the figure caption.

Application of DPWD to stochastic processes (Martin and Flandrim 1985) and Doppler signals have been reported in the literature. Motivated by this, the DPWD was implemented with the aim of better assessing some features of Doppler signals.

As shown in Fig. 7.2, the cross terms present in the DPWD may introduce difficulties in interpreting its results. To verify the possibility of obtaining an enhanced time-frequency distribution for Doppler signals, the DCWD was also implemented.

According to Fig. 7.3, the DCWD does not appear to provide better results than the DPWD. As mentioned before, the purpose of the proposed kernel is to smooth out the cross terms that lay among the autocomponents in the time-frequency plane. Nevertheless, for the Doppler signals, since the autocomponents are continuously distributed along the time and frequency axis, auto and cross terms may be superimposed, and therefore, DCWD does not work efficiently in this application.

This is in agreement with work of Baraniuk and Jones (1993). These authors, working with two components of frequency, have shown that the efficiency of a specific time-frequency distribution is dependent on the signal analysed and particularly, that the DCWD offers poor frequency resolution for frequency modulated signals.

Lately, some other kernels have been proposed in the literature (Jones and Parks 1990; Baraniuk and Jones 1993) that are claimed to have better performance than the ones discussed in this chapter and therefore, should be object of further investigation concerned to their application to Doppler signals analysis.
Based on these considerations, care should be taken during the interpretation of these time frequency distributions when applied to Doppler signals. Off-line CFFT produces more reliable results and, as mentioned above, since averaging of two or more CFFT columns is not performed, a better time resolution is achieved.

7.7 - Summary

This chapter has described an off-line software to analyse recorded Doppler signals. The software allows the processing of the Doppler signals with a better time-frequency resolution than that offered by the real time software. The options for processing the signals are: CFFT, Wigner distribution and Choi-Williams distribution.

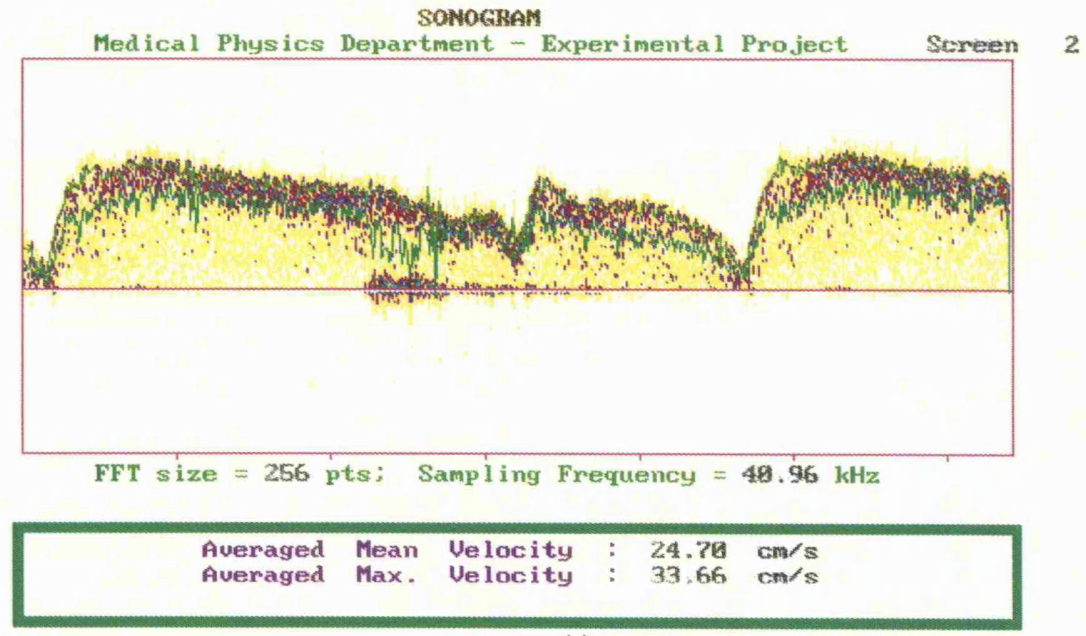

(a)

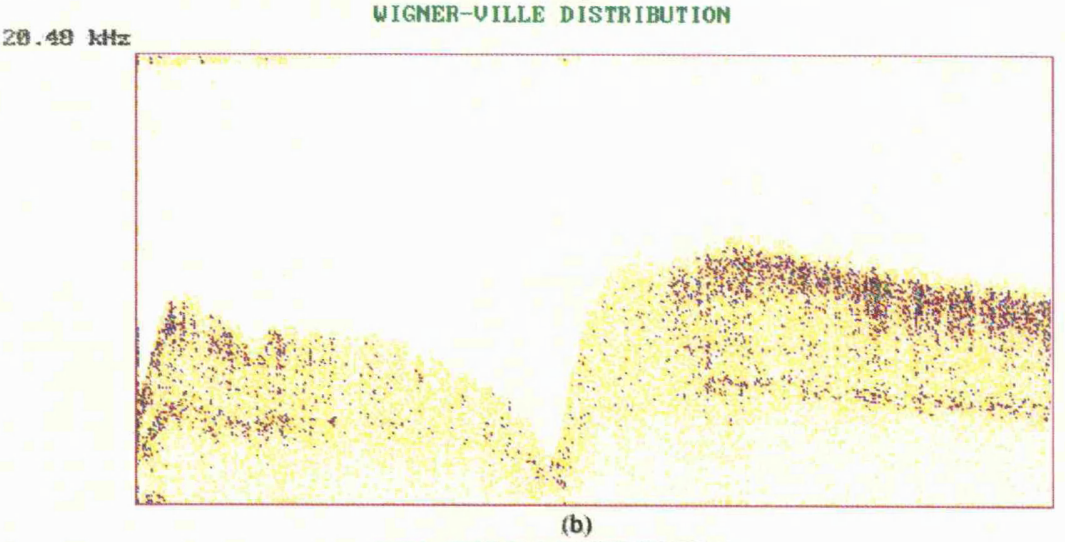

(b)

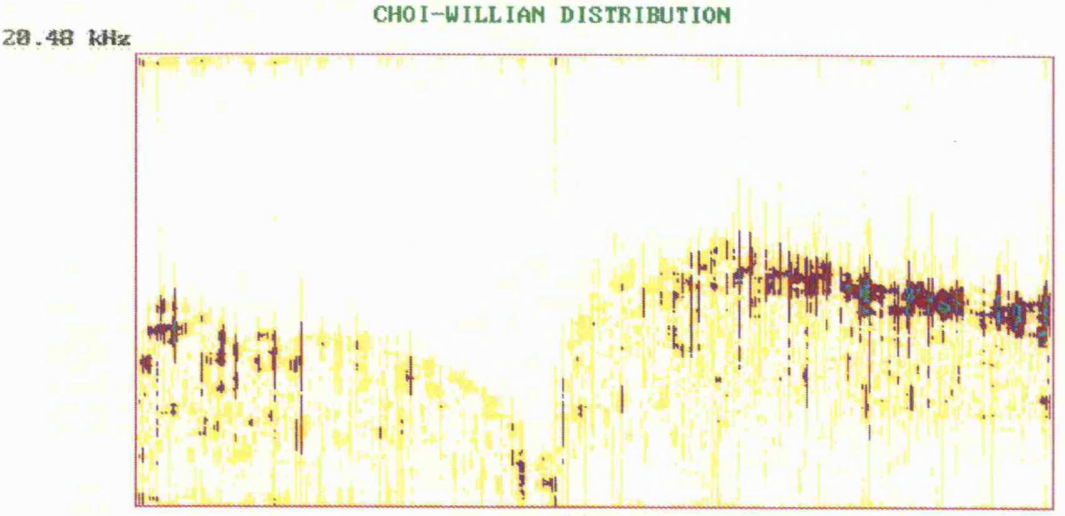

(c)

Fig. 7.3 - Doppler signals sampled from coronary artery at 40.96 kHz and processed by (a) CFFT with double overpadding, (b) DPWD with $\Delta n = 64$ and (c) DCWD with $\Delta n = 64$, $\sigma = 10$.

Chapter 8 - Experiments *in vitro*

8.1 - Introduction

In this chapter, experiments carried out *in vitro* to better characterise the performance of the Doppler system are reported. These experiments include observation of flow behaviour close to the catheter tip and measurements of flow velocity performed with blood and a blood analogue.

8.2 - Experimental Observation of Flow Proximal to the Catheter Tip

Chapter 6 mentioned the work of Kagiyama et al. (1988) who used numerical techniques to describe the flow profile away from the catheter tip for steady flow in a vessel with a diameter of 7 mm. Their work characterised the flow transition from annular to parabolic profiles but did not emphasise the flow behaviour in the proximity of the catheter tip. The objective of this section is to report some observations performed to investigate whether the flow close to the catheter tip presents turbulent behaviour. Turbulent flow develops irregular fluctuations of velocity in space and time. This could further influence the velocity estimates obtained for ranges close to the catheter tip.

For this, the flow rig illustrated in Fig. 8.1 was built in order to obtain photographic records of a column of dye passing around the catheter tip. The set up produces steady flow whose velocity is established by the height of the reservoir.

A segment of glass pipe was manufactured with auxiliary inputs to allow the insertion of the Doppler catheter and the placement of a needle, used to introduce dye into the circulating solution. The solution used was a mixture of glycerol and water (42%-58%) which has, at the temperature of 20° C used, the same viscosity

as blood at the body temperature (0.04 P - Hoskins et al. 1990). The dye used was fluorescein sodium mixed with milk to increase the stability of the dye column and its reflective properties.

The level of the solution in the headtank was kept constant by a pump connected to an auxiliary reservoir and an overflow outlet to assure a constant flow velocity. The solution at the output of the rig, contaminated with dye, was discarded.

The maximum flow velocity sampled without aliasing by the Doppler system described in Chapter 2 is 115 cm/s, but higher velocities than that have been registered in coronary circulation (Nakatani et al. 1992; Ofili et al. 1993). In this study, the height of the headtank was adjusted to produce a flow velocity close to the maximum detectable with the Doppler system used.

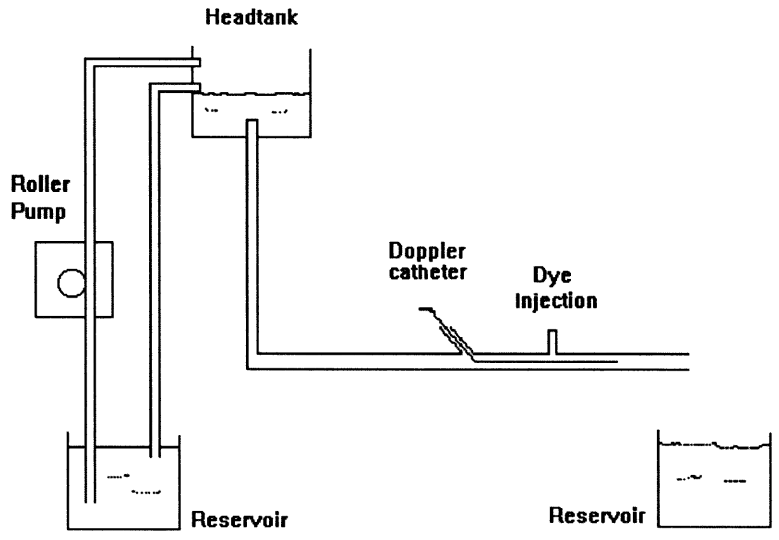

Fig. 8.1 - Diagram of set up used to register the flow behaviour passing by the catheter tip

The mean velocity, measured using a stopwatch technique, was set to 55.5 cm/s. For a parabolic flow, the corresponding maximum velocity is equal to 111 cm/s. The inner diameter of the glass pipe used was 3 mm. Therefore, the Reynolds number was 416 and the inlet length, 3.75 cm. The pictures were taken 23 cm distal to the point of the catheter insertion with the use of a microlens.

Fig. 8.2 reproduces the photographs obtained. As can be seen, there was no production of eddies. The filaments of dye changed their direction when passing around the catheter tip but retained their integrity within the region in which the velocity measurements are usually taken. Therefore the velocity estimates should only be affected by the factors discussed in Chapter 6.

8.3 - Experimental Measurements of Flow Velocity

In this section, flow velocity measurements performed with the system developed *in vitro* are reported. These experiments were carried out to verify the accuracy of the Doppler catheter measurements, mainly in steady flow regime. This section is divided in two parts, firstly describing measurements with blood and then, measurements with a blood analogue. Blood analogues more commonly used are not very suitable for these measurements at the high frequency utilised by Doppler catheters. The main limitations are the small size of the particles required to achieve Rayleigh criterion (diameter of the particles has to be much smaller than the wavelength of the transmitted pulse $\approx$ 75 μm at 20 MHz) and the need of determining the optimal particle concentration in the solution to achieve a similar ultrasonic attenuation to that of blood. For instance, experiments with a blood analogue proposed by Oates (1991) did not allow the recording of signals beyond the range of 4 mm due to rapid attenuation of the nylon particle suspension at 20 MHz. For these reasons, out of date human blood from a blood bank was used, but there were difficulties in working with it (availability, safety precautions and proper storage). In spite of the mentioned limitations, in order to perform additional

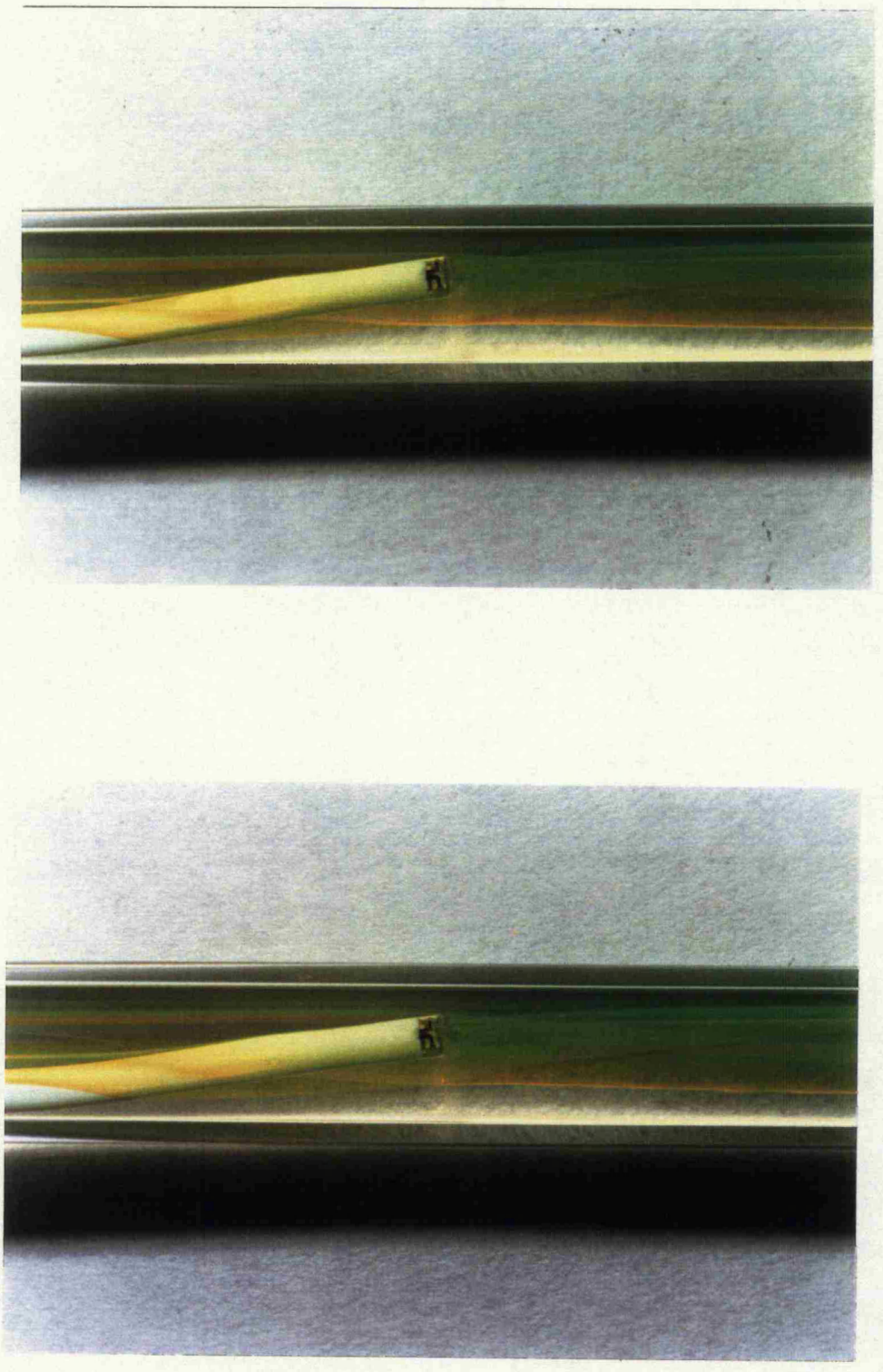

Fig. 8.2 - Photographs of a column of dye passing around the Doppler catheter tip in steady flow regime.

observations, some measurements were carried out with a solution containing Sephadex particles whose diameter ranges from 20 to 70 μm (Hoskins et al. 1990).

Fig. 8.3 presents a sketch of the flow rig set up to produce steady flow for the measurements described below. It was based on the review by Law et al. (1989) and has the following characteristics:

- The segment from which the measurements are obtained is vertical to avoid the settling of the scattering particles of the solution used. A glass tube is used since a rigid tube provides symmetry for the velocity profile.

- The use of a headtank to produce steady flow avoids the necessity of a very stable pump and the flow velocity is changed by adjusting the headtank height.

- The level of the headtank is kept constant by a pump and an overflow outlet. This assures a constant velocity. The pump is placed on a different work surface to avoid the transmission of vibration to the test region.

- The placement of the outlet in the bottom of the headtank and the use of a magnetic stirrer for the reservoir avoid the sedimentation of particles in both containers.

8.3.1 - Measurements with Blood

The use of blood provides results closer to those obtained in clinical applications, but some care is necessary. A roller pump was used to avoid damage to the blood cells and the volume capacity of the flow rig was reduced as much as possible since only small amounts of blood were available. 2000 units of heparin were mixed with

the blood to avoid clotting which would affect the acoustic power scattered back to the transducer.

Velocities were measured for flow away and towards the transducer. To speed up the measurements, two Doppler catheters were utilised. They were inserted into the rig through auxiliary inputs (as shown in Fig. 8.3), and connected, alternatively, to the system described in Chapter 3. The tip of the downstream catheter was placed 15 cm away from the other to avoid the entrance effect in its measurements. The diameter of the test section was 3 mm.

The height of the reservoir was changed a number of times and the mean flow velocity was measured using a stopwatch technique. The IWMV and the detected maximum velocity were recorded for both catheters for each new position of the reservoir. Fig. 8.4 depicts the results obtained.

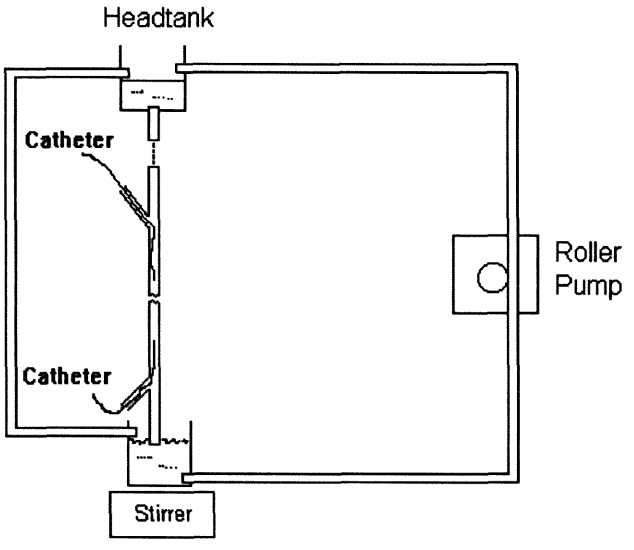

Fig. 8.3 - Diagram of set up for flow velocity measurements

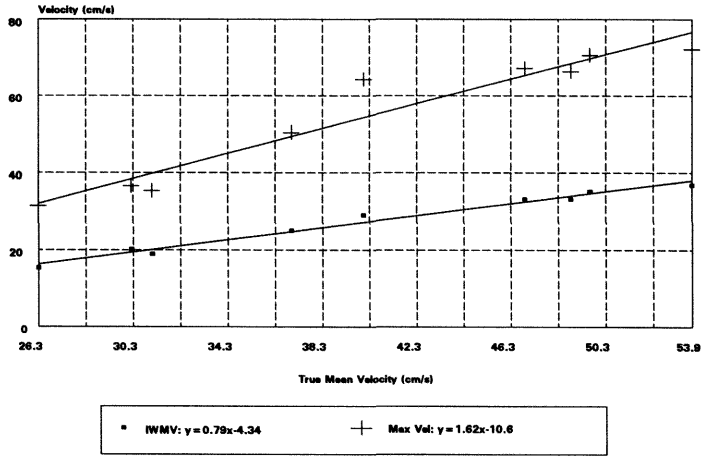

(a)

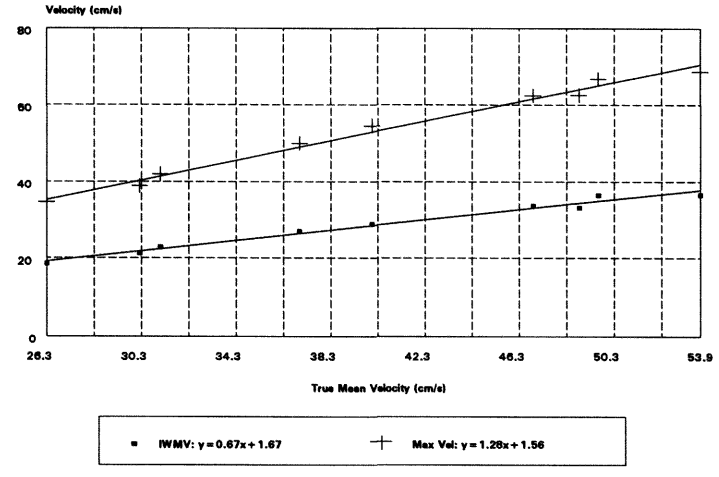

(b)

Fig. 8.4 - Relationships among the true mean velocity, the calculated IWMV and the detected maximum velocity for flow away from (a) and towards (b) the catheter. The measurements were performed for blood in steady flow using the same range gate (6 mm). The equation of the lines fitted to the experimental points by linear regression are given in the legends.

For two different mean flow velocities (30.8 and 53.9 cm/s), the range gate of the Doppler system was set to 6 mm and both catheters were manipulated inside the glass tube to obtain the highest maximum velocity and an intensity weighted mean frequency close to half of the spectra. The range gate was then changed repeatedly

and the corresponding velocity estimates obtained. The results are presented in Figs. 8.5 and 8.6 along with the true mean velocity, measured using a stopwatch technique, and the true maximum velocity, plotted as twice the mean velocity (this value corresponds to the maximum velocity where the flow profile is parabolic).

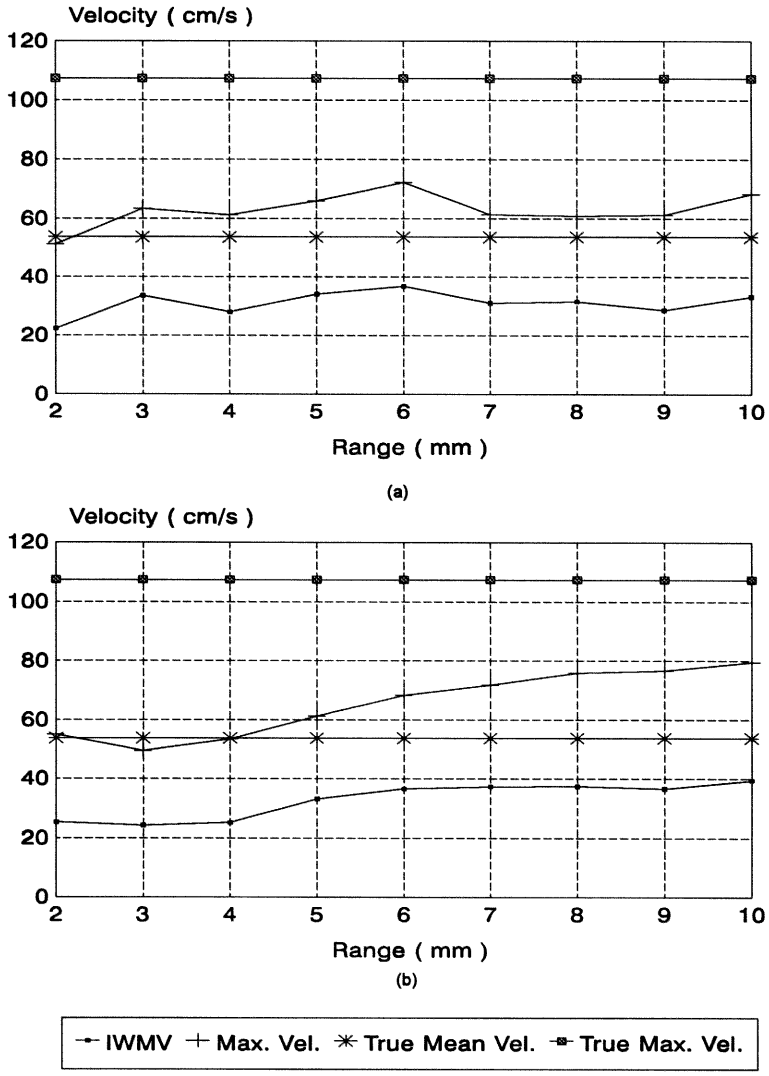

Fig. 8.5 - Relationships between the true and estimated velocities at different sampling points from the transducer for flow away from (a) and towards the catheter tip (b). The measurements were performed for blood in steady flow without changing the catheter position. The true mean velocity is 53.9 cm/s and the true maximum one is plotted as twice the mean (parabolic flow profile).

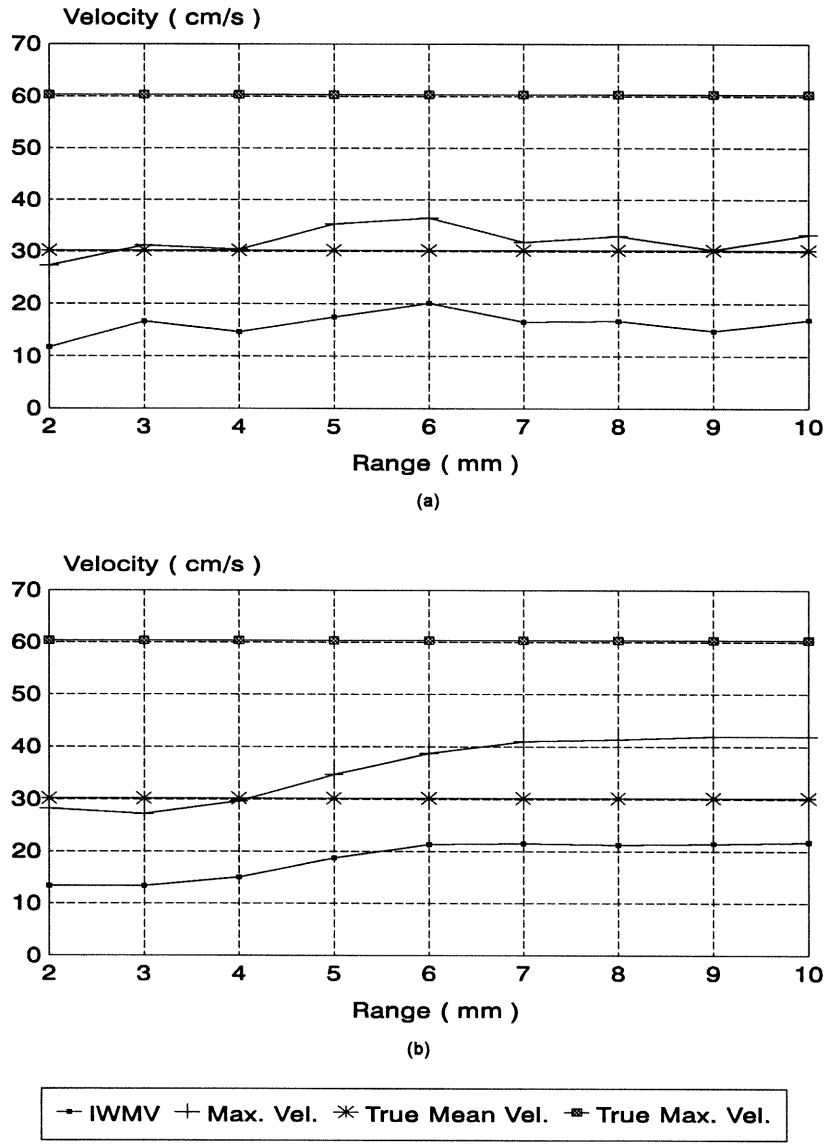

Fig. 8.6 - Relationships between the true and estimated velocities at different sampling points from the transducer for flow away from (a) and towards the catheter tip (b). The measurements were performed for blood in steady flow without changing the catheter position. The true mean velocity is 30.8 cm/s and the true maximum one is plotted as twice the mean (parabolic flow profile).

The gain of the amplifiers and the cut-off frequency of the 'wall thump' filters were kept constant during the measurements: 0 dB and 300 Hz, respectively.

Figs. 8.5 and 8.6 shows that the velocity estimates are a function of the range used in the Doppler system. The different values obtained at each range should be related to the factors discussed in Chapter 6, namely, the changes of the beam width, the flow profile and the sample volume position within the vessel along the different ranges.

The experiments with blood were limited to a particular beam radius/vessel radius ratio and some few Reynolds numbers due to the practical difficulties involved (i.e., availability and manipulation of blood) and even the impossibility of covering all possible geometries (vessel radius and sample volume positions) and flow velocities. The diameter of 3 mm was chosen for the experiments above because the size of most normal proximal coronary arteries ranges between 3 to 3.5 mm (Block 1986).

8.3.2 - Measurements with Sephadex

The results described above provide a good idea about current problems in obtaining accurate velocity estimates with Doppler catheters. Nevertheless, blood did not give the flexibility necessary to better assess the aspects discussed in Chapter 6. For this, measurements were performed with a solution containing Sephadex. Due to the size of the Sephadex particles, caution is necessary in comparing Doppler spectra obtained for this solution with those obtained for blood. Comparison among results obtained for Sephadex allows conclusions to be taken.

Sephadex was diluted in a degassed solution of water (58%) and glycerol (42%) in a proportion of 8 gm/l. The solution was allowed to stand overnight to permit the Sephadex particles to achieve their final size. The temperature of the laboratory was kept to $20 \pm 3°$ C during these measurements.

Using the flow rig shown in Fig. 8.3, velocity measurements were performed for flow away from and towards the catheter (in a similar way to those described above) in glass tubes of two different diameters: 3 mm (Fig. 8.7) and 5 mm (Fig. 8.8).

Two different flow velocities were used for the measurements shown in Fig. 8.7: 21.43 cm/s (Figs 8.7.a and 8.7.b) and 45.86 cm/s (Figs. 8.7.b and 8.7.c). Figs. 8.7.a and 8.7.c show measurements carried out for flow away from the catheter tip. Measurements obtained for flow towards the catheter are presented in Figs. 8.7.b and 8.7.d. For each of these situations described, the Doppler catheters were manipulated inside the tubes to be placed in two different and arbitrary positions. Therefore, the effects of the catheter position on the measurements could be observed. The different curves presented can be related to the different positions by the indices (1 or 2) presented in the legend of the figure. Calculated IWMV and estimated maximum velocity are plotted for both positions. The true mean velocity (measured by stopwatch technique) and the true maximum velocity (supposing a parabolic flow profile) are also plotted for reference.

Similar data are presented in Fig. 8.8 for the glass tube of 5 mm. The two velocities used were: 18.65 cm/s (Figs. 8.8.a and 8.8.b) and 25.89 cm/s (Figs. 8.8.c and 8.8.d). Figs. 8.8.a and 8.8.c show measurements for flow away from the catheter and Figs. 8.8.b and 8.8.d display measurements for flow towards the catheter.

Flow velocity measurements were also performed for pulsatile flow of arbitrary pattern in glass tubes of two diameters: 3 mm and 5 mm. Pulsatile flow was obtained by including a chamber (sketched in Fig. 8.9) in series with the pipe feeding the solution into the glass tube shown in Fig. 8.3. The moveable wall was

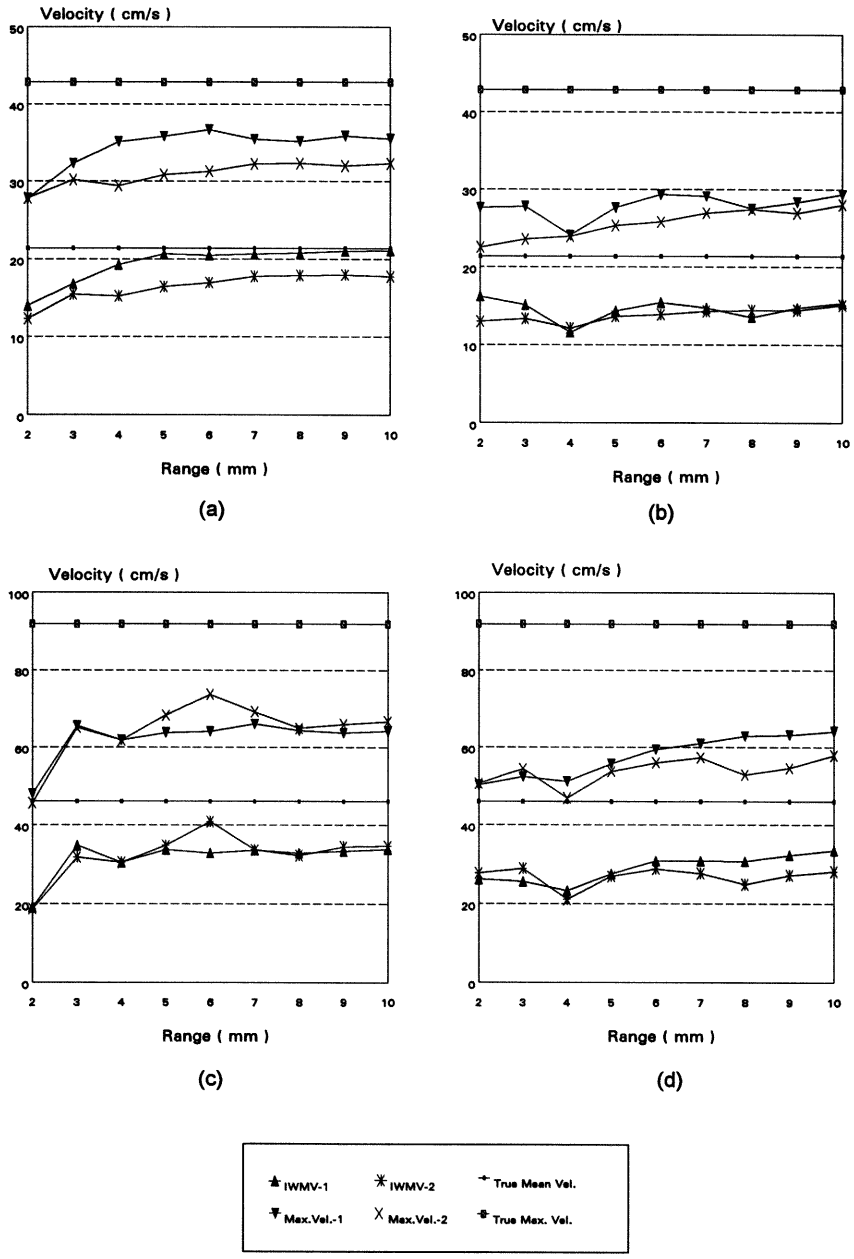

Fig. 8.7 - Measurements performed for Sephadex solution in steady flow from a glass tube with a diameter of 3 mm. Figs 8.7.a and 8.7.b were obtained for the flow velocity of 21.43 cm/s. Figs. 8.7.c and 8.7.d for a velocity of 45.86 cm/s. Figs. 8.7.a and 8.7.c show measurements carried out for flow away from the catheter tip. Measurements obtained for flow towards the catheter are presented in Figs. 8.7.b and 8.7.d. The indices utilised (1 and 2) discriminate the IWMV and maximum velocity measurements obtained for two different catheter positions.

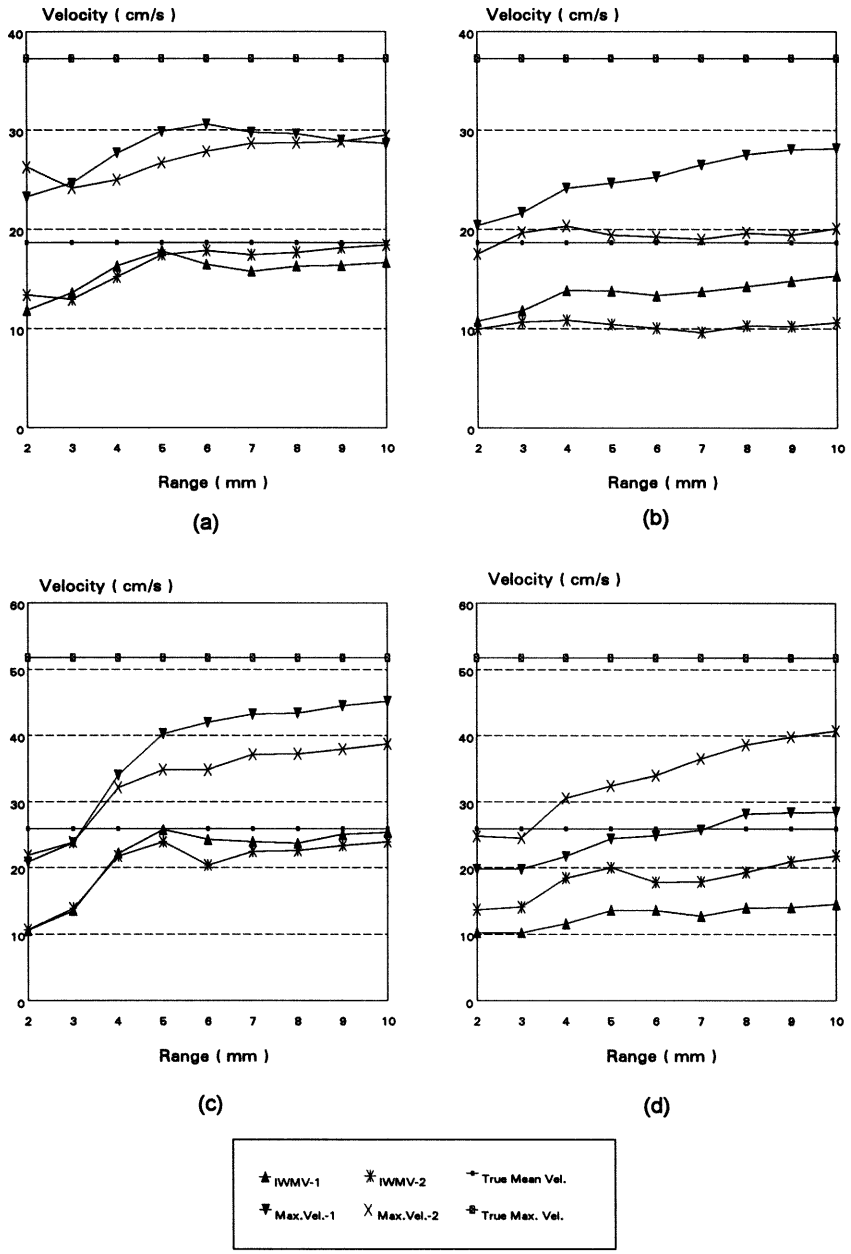

Fig. 8.8 - Measurements performed for Sephadex solution in steady flow from a glass tube with a diameter of 5 mm. Figs 8.8.a and 8.8.b were obtained for the flow velocity of 18.65 cm/s. Figs. 8.8.c and 8.8.d for a velocity of 25.89 cm/s. Figs. 8.8.a and 8.8.c show measurements carried out for flow away from the catheter tip. Measurements obtained for flow towards the catheter are presented in Figs. 8.8.b and 8.8.d. The indices utilised (1 and 2) discriminate the IWMV and maximum velocity measurements obtained for two different catheter positions.

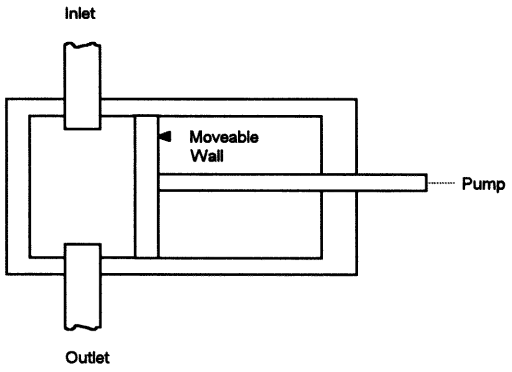

Fig. 8.9 - Diagram of chamber connected to a pulsatile pump and put in series with the feeding pipe to the test segment of the flow rig shown in Fig. 8.3 to produce pulsatile flow.

driven by a pulsatile pump (Pulsatile Blood Pump, Harvard Apparatus, USA).

Fig. 8.10 displays the calculated IWMV results obtained for the glass tube of 3 mm at two mean flow velocities: 30.72 cm/s (Fig. 8.10.a) and 35.48 cm/s (Fig. 8.10.b). The true mean velocity is also plotted.

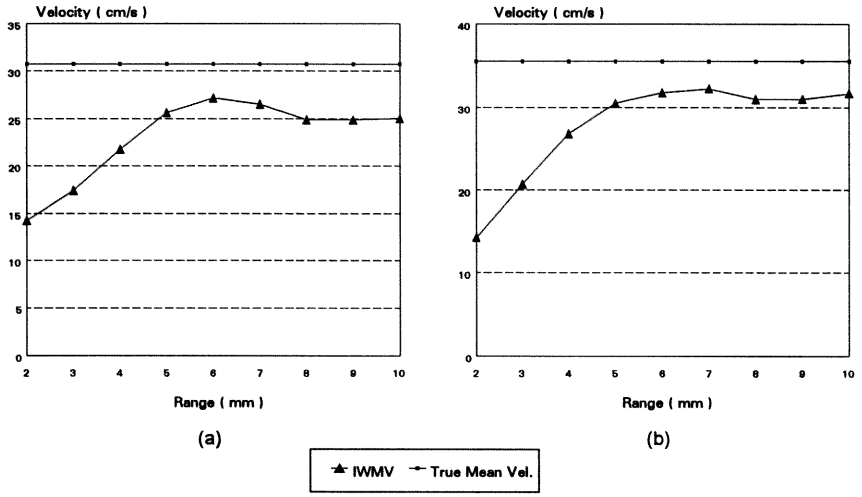

Fig. 8.10 - Measurements performed for Sephadex solution in pulsatile flow from a glass tube with a diameter of 3 mm. Fig 8.10.a was obtained for the flow velocity of 30.72 cm/s. Fig. 8.10.b for a velocity of 35.48 cm/s

IWMV measurements for the glass tube of 5 mm is shown in Fig. 8.11 for two mean flow velocities: 20.69 cm/s (Fig. 8.11.a) and 26.66 cm/s (Fig. 8.11.b). The true mean velocity is plotted for reference.

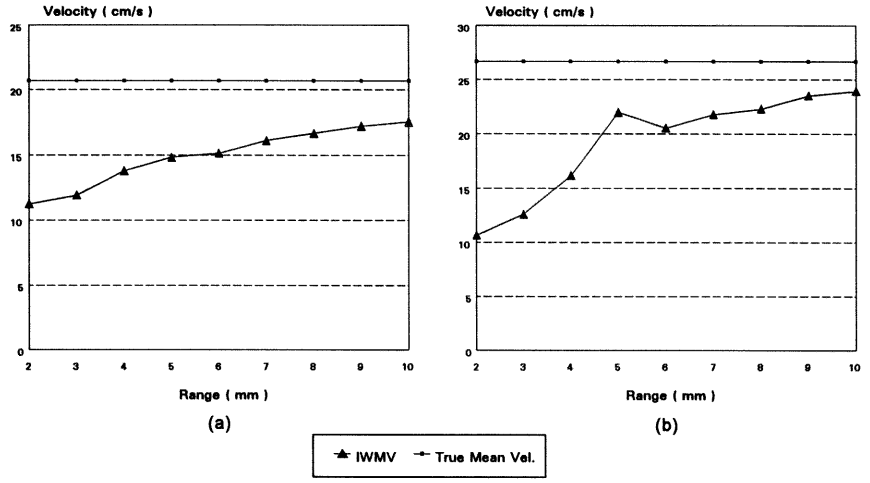

Fig. 8.11 - Measurements performed for Sephadex solution in pulsatile flow from a glass tube with a diameter of 5 mm. Fig 8.11.a was obtained for the flow velocity of 20.69 cm/s. Fig. 8.11.b for a velocity of 26.66 cm/s

Figs. 8.10 and 8.11 show that IWMV obtained for pulsatile flow present similar behaviour to those obtained for steady flow.

The measurements reported in Figs. 8.7 and 8.8 show the strong dependence of the velocity estimates on the range used, catheter position and vessel diameter. For the glass tube of 5 mm (Fig. 8.8), larger differences between velocity estimates for different catheter positions were found. This should have been expected since a smaller percentage of the flow profile is insonated in this case than that for the 3 mm glass tube. Changes of flow velocity did not appear to introduce any particular trend in the errors present in these measurements. Nevertheless, the flow profile for flow away from the catheter may change and affect the measurements as discussed in Chapter 6.

8.4 - Discussion and Conclusion

The presence of the Doppler catheter changes the flow velocity profile in the normal circulation (Tadaoka et al. 1990); but, according to the photographs shown in Fig. 8.2, the catheter does not introduce additional disturbances, such as eddies, that could further affect velocity estimates.

The experimental measurements performed provide information on the accuracy of the Doppler system in producing flow velocity estimates. Fig. 8.4 reveals an underestimation of flow velocities for flow away and towards the catheter which should be attributed to the non uniform insonation of the flow profile. Figs. 8.5 and 8.6 show that the velocity estimates depend also on the range utilised to produce the measurements. It was not possible to note any particular change in the behaviour of the curves presented by Figs. 8.5 and 8.6 due to the velocity increase.

The measurements performed with Sephadex solution (Figs. 8.7 and 8.8) show the effect of the catheter position and vessel diameter on the velocity estimates. Figs. 8.10 and 8.11 show that Doppler catheters present similar performance for pulsatile flow.

Based on these observations, it is interesting to comment on some of the current techniques investigated for evaluating the coronary circulation. As mentioned in Chapter 1, the application of the continuity equation requires the sampling of the velocity at the pre-stenotic and stenotic segments. Johnson et al. (1989) and Nakatani et al. (1992) reported that their measurements were taken by keeping the position of the catheter constant and changing the range to sample the maximum velocity in the two segments. According to Figs. 8.5 and 8.6, the change of range can represent another source of error for the described procedure. For each range, the catheter would have to be manipulated to ensure that the maximum flow

velocity was sampled. As the flow profile changes along the vessel, the relation between maximum flow and mean flow velocities is likely to be different at the different ranges. Therefore, this technique should not be able to produce accurate results.

For the coronary blood flow reserve ratio measurements (CBFRR - Chapter 1), it is not always described in the literature how the velocity estimates were obtained. It is advisable to keep the same range for the measurements obtained in the basal condition and during hyperaemia to minimise errors.

Considering these aspects, quantitative data currently available and conclusions obtained about a particular technique investigated may not be reliable. As already mentioned in Chapter 6, further technical developments should be aimed to increase the width of the ultrasound beam produced by Doppler catheters in order to achieve a uniform vessel insonation and therefore, more accurate velocity estimates. Experimental and clinical re-assessment of these techniques should be performed after technical improvements to verify their potential as diagnostic tools. At present the clinical value of Doppler catheter tipped measurements may be concealed by artefacts present in the measurements.

Chapter 9 - Measurements *in vivo*

9.1 - Introduction

The measurements reported in this chapter were performed in patients undergoing percutaneous transluminal coronary angioplasty (PTCA) by Prof. DeBono at Glenfield General Hospital (Leicester).

PTCA is a technique to increase the luminal diameter of a stenosed artery through application of a lateral force against the vessel wall. This is performed by means of a distensible balloon attached to a catheter tip. PTCA is indicated for concentric and discrete proximal stenoses which occlude more than 50% of the vessel diameter (Block 1986).

Briefly, PTCA is performed by placing, through a femoral puncture, a guide catheter in the coronary ostium. A steerable guide wire is inserted through the guide catheter and passed through the stenoses into the distal coronary artery. The next step is the insertion of the dilation balloon over a guide wire up to the stenotic vessel segment. The guide wire is removed and the balloon is inflated three or four times at the internal pressure of 5 atm. The catheters are then withdrawn. The manipulation of the catheters is done under fluoroscopy control. Cineangiography is performed before and after the intervention to assess its results.

The measurements performed allowed testing of the viability of applying the developed system (Chapter 3) in clinical situations and the acquisition of data for further processing.

Examples of parameters calculated off-line from stored frequency envelopes, ECG and pressure waveforms obtained during angioplasty are also presented. The routines developed to calculate these parameters are described in this chapter.

While this section could have been included in Chapter 3, we opted to place it here in order to be more easily related to the results presented.

9.2 - Measurements *In vivo*

In preparation for performing measurements in patients, the system (consisting of the PC, A/D board, DSP board, Doppler system and pressure amplifier) was submitted to an electrical safety test according to the requirements of HEI-95 (Health Equipment Information 95).

The measurements of flow velocity were carried out before and after angioplasty, introducing the catheter close to the stenosis using a guidewire. Measurements of pressure were simultaneously taken, introducing the pressure catheter, which had been previously zeroed, by an incision in the other femoral artery up to the root of the aorta. As mentioned in Chapter 2, ECG signals were obtained from the amplifier of the monitoring system used by the medical staff.

Measurements were taken from a total number of 8 patients, using the developed system, between 14/10/93 and 8/12/94. This small number of patients is a reflection of the difficulties present in obtaining the data. These difficulties were mainly the availability of the catheters (expense being the limiting factor - catheter price: £650) and the fact that not all patients were judged suitable for these measurements by the doctors during the catheterization. Among these patients, only three had the pressure signals sampled following medical evaluation of the patients.

Fig. 9.1 presents examples of the sonograms, velocity envelopes, ECG and pressure waveforms recovered from files of signals sampled from the left coronary artery of the same patient, before and after angioplasty proximal to the stenosis site.

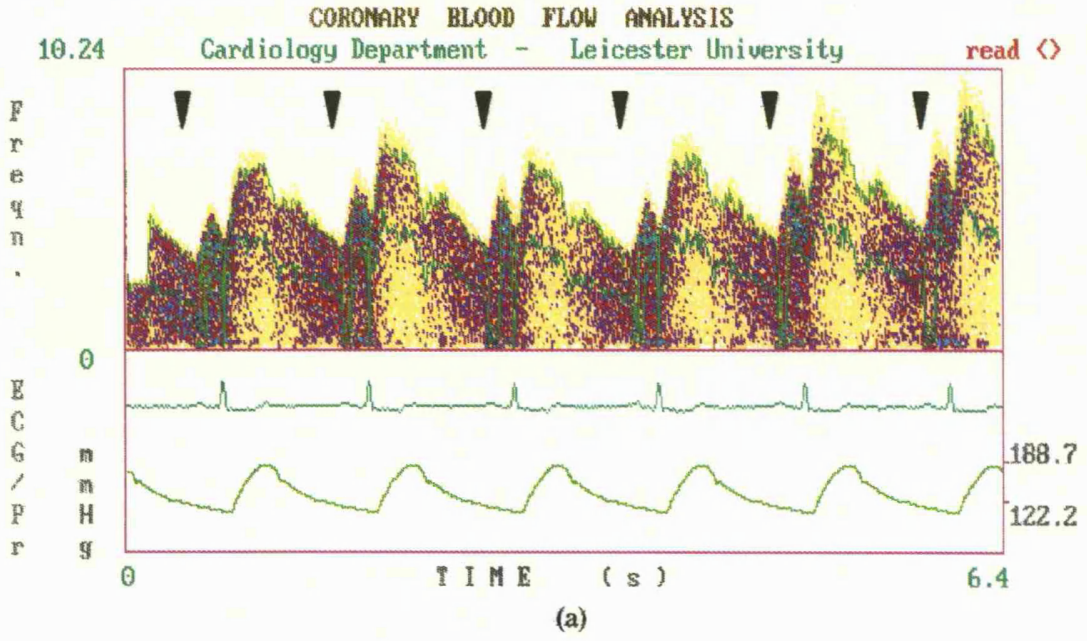

(a)

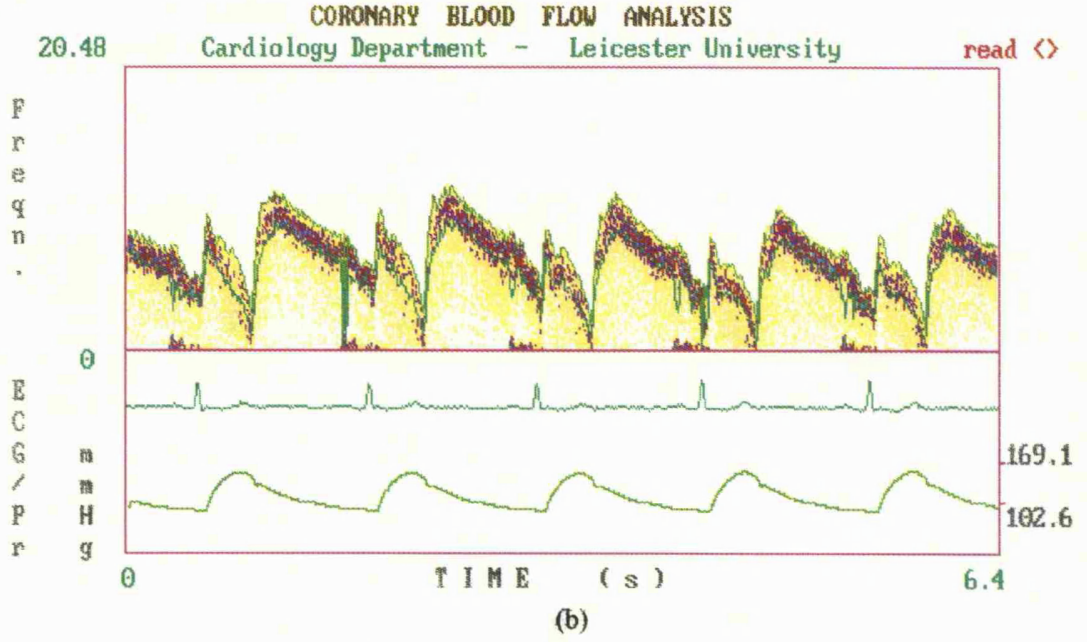

(b)

Fig. 9.1 - Examples of sonogram, maximum velocity envelopes, IWMV curves, ECG and pressure waveforms that correspond to those shown on screen at the time of their acquisition. These signals were sampled from the left coronary artery of a same patient, before and after angioplasty downstream to the stenosis site.

It is interesting to observe that the blood flow pattern changed between the two measurements. Fig. 9.1.a shows that the majority of flow was occuring in the systolic period (between QRS complex and dicrotic notch) and not during the diastolic period, as in the normal coronary circulation, due to the flow constraint

produced by the stenosis. After angioplasty, it was possible to note that the flow pattern assumed a normal behaviour with a higher flow velocity, indicating the success of the intervention. (Note that in Fig. 9.1.a the maximum frequency estimator failed (arrows) due to the presence of high intensity signals originating from wall movements. As mentioned in Chapter 3, the presence of these artefacts resulted in the later inclusion of the 'wall thump' filters in the final design of the A/D conversion board).

Another storing option allows the user to record the envelopes of the sonogram, ECG and pressure waveforms (Chapter 3). The next section describes the software used to calculate parameters from these curves and presents some examples.

9.3 - Off-line Processing of Sonogram Envelopes

Software was written to calculate separately the averaged velocity during diastole and during systole for the curves of IWMV and maximum velocity envelope. The ratio between the averaged diastolic and averaged systolic velocities is also calculated for both curves. These parameters quantify the most important features of the coronary blood flow since they may provide information on phasic changes of the coronary blood flow due to the presence of stenosis as shown in Fig. 9.1.

The identification of the systole and the diastole can be achieved by detecting the dicrotic notch and the QRS complex.

Fig. 9.2 shows that the position of the dicrotic notches in the pressure curve can be located by finding the peak negative of the derivative of the pressure (*dP/dt* - Fig. 9.2.b). This derivative is obtained by subtracting the pressure values of two

consecutive samples of the pressure data. The diastolic flow velocity is calculated starting 25 ms after the detection of the dicrotic notch (Mancini et al. 1989).

The algorithm implemented for the detection of QRS complexes was based on the work of Lima et al. (1983). According to these authors, their algorithm was able to detect correctly 99.58% of QRS complexes for 21 different ECG signals belonging to the MIT Arrhythmia Database.

In this approach, the ECG signal (Fig 9.3.a) is filtered and the modulus of the resultant signal (Fig 9.3.b) submitted to a set of tests to identify the QRS complexes. These tests are based on physiological rules, taking into account the QRS duration and latencies between them.

The components of frequency of the ECG signal that correspond to the QRS are selected by a filter centred on 17 Hz, having a bandwidth of 16 Hz (Ahlstrom and Tompkins 1985). After obtaining the modulus of the filtered signal, its maximum value is found and three arbitrary thresholds are determined:

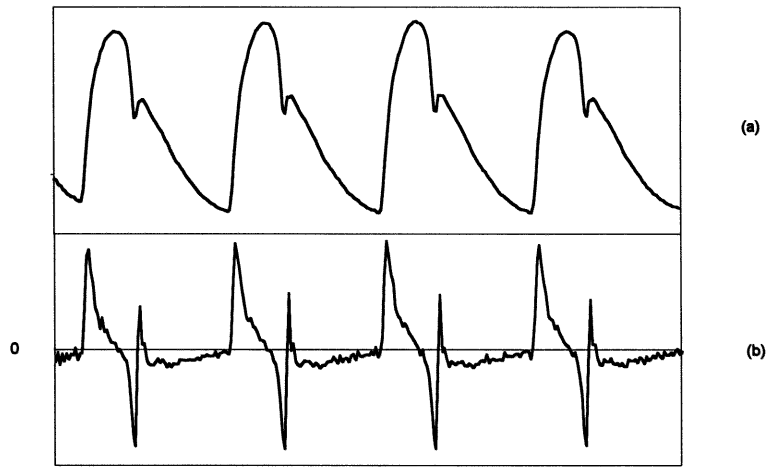

Fig. 9.2 - (a) Pressure waveform P(t) sampled from the root of aorta by an intravascular pressure catheter and (b) its $\Delta P/\Delta t$. The peak negative of the derivative of the pressure corresponds to the position of the dicrotic notch.

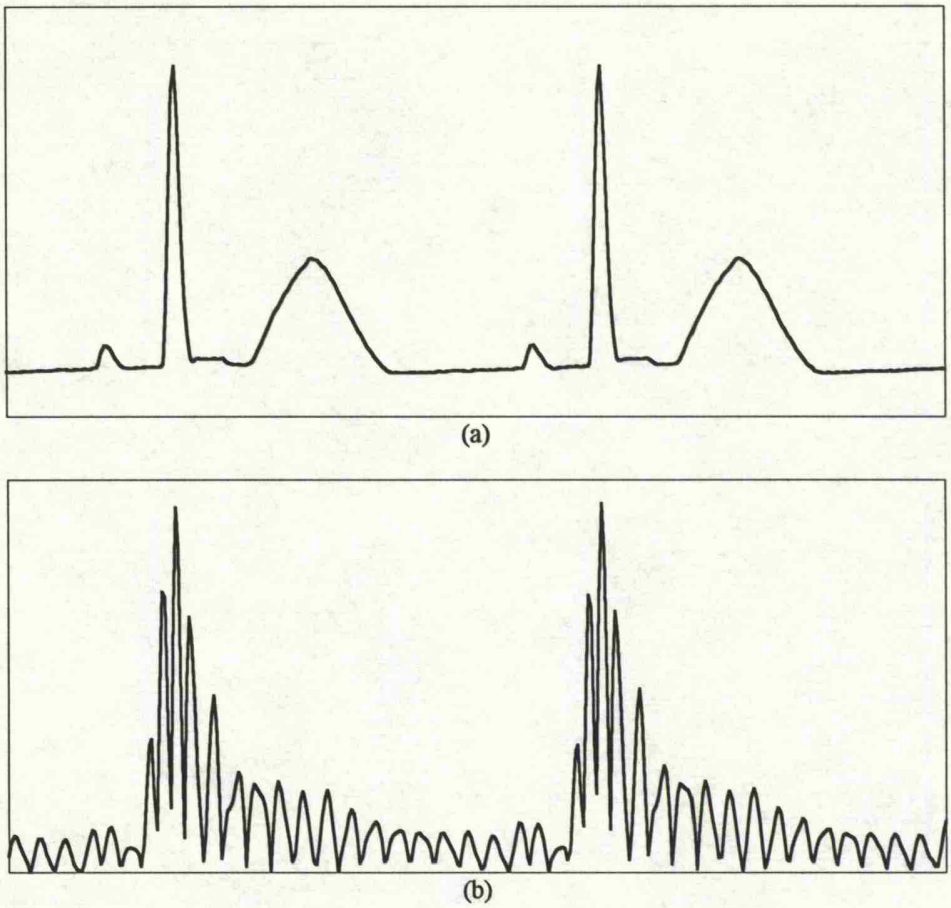

Fig. 9.3 - (a) ECG signal and (b) its modulus after processing by a bandpass filter centred in 17 Hz (bandwidth of 16 Hz).

MNT (minimum threshold) = 15% of maximum value,

T (threshold) = 35% of maximum value,

MXT (maximum threshold) = 80% of maximum value.

The recorded signal is then compared to the threshold **T**. When a sample larger than **T** is found, the subsequent samples, corresponding to an interval of 160 ms, are tested to verify the number of times that they cross upwards the threshold **T**. The interval of 160 ms corresponds to the refractory period of the heart cells, when excited cells are unable to be reactivated (Milnor 1980). The following decisions are taken based on the number of crossings (NC):

case 1: NC >= 5

When this situation occurs, the threshold T is increased by 10% and the test repeated for the current interval. This procedure continues until the occurrence of case 2 or the new threshold achieves MXT. If the latter happens, the segment is assumed to be contaminated by noise. The interval is discarded and the threshold is slowly decreased in intervals of 37.5 ms down to the previous value.

case 2: 2 <= NC < 5

A QRS complex is considered to be found. When the first crossing is detected, the routine always starts tracking the maximum value (MV) of the interval that corresponds to the R wave, if the segment is accepted as a QRS complex.
MNT is modified to: MNT = 0.9*MNT + 0.1*MV.

case 3: N=1

For this case, the width of the event is tested. The algorithm also tracks the interval between RR detections. The event is considered to be a QRS complex, if it occurs after a period greater than to a quarter of the last RR interval and its width is between 40 to 200 ms. Otherwise, it is rejected.

case 4: N=0 and the time interval between the present tested sample and the last QRS detection is above 1.5 times the last RR interval.

If the period of time between the last QRS detection and the present sample being tested is larger than 1.5 times the last RR interval, the threshold is decreased by 10% and the interval tested again, looking backwards for a possible missed QRS. This procedure is repeated up to the occurrence of case 2, case 3 or until the new threshold reaches MNT. If the latter happens, the old threshold is retrieved and the tests carried on.

A database was not available to verify the efficiency of our implementation of this algorithm. It was tested with ECG signals from a simulator and a healthy volunteer.

The routine has been working satisfactorily for all ECG signals sampled from the patients.

Figs. 9.4.a, 9.5.a and 9.6.a give examples of curves retrieved from files storing ECG, pressure, maximum frequency envelope and IWMF waveform. The identification of the QRS and dicrotic notch are shown, as detected by the routines described. Figs. 9.4.b, 9.5.b and 9.6.b present the parameters calculated by this software where:

HR = Heart Rate;
SD = Standard Deviation;
AMNV = Averaged Mean Velocity;
AMXV = Averaged Maximum Velocity;
ASMNV = Averaged Systolic Mean Velocity;
ADMNV = Averaged Diastolic Mean Velocity;
ASMXV = Averaged Systolic Maximum Velocity;
ADMXV = Averaged Diastolic Maximum Velocity;
DSMNVR = Diastolic/Systolic Mean Velocity Ratio.

9.4 - Discussion and Conclusion

The measurements obtained *in vivo* have shown the viability of applying the developed system in the clinical practice. The digital storage of the data allows their prompt recovery to compute a number of parameters discussed in the literature and allows the storage of a data bank for future studies. The ability to register phasic changes in flow velocity illustrates the potential of Doppler catheters as research tools for qualitative assessment of the coronary circulation.

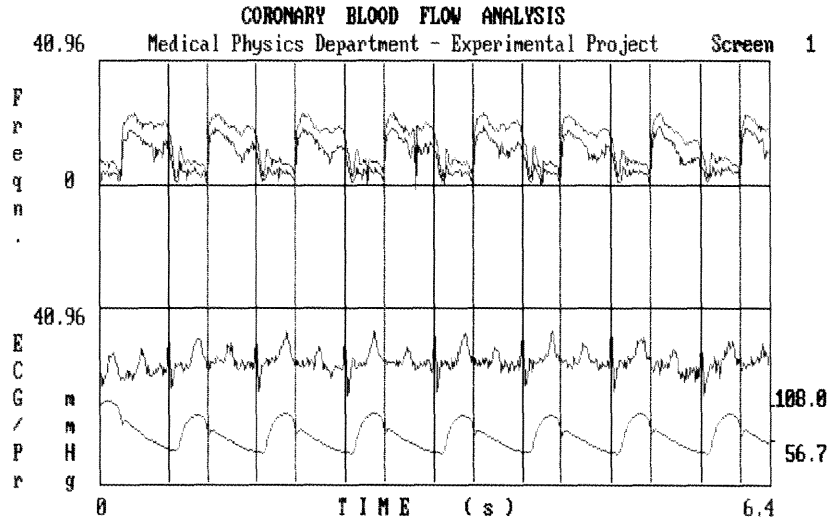

(a)

CORONARY BLOOD FLOW ANALYSIS
Medical Physics Department - LRI

PARAMETERS

H. R. = 70.59 bpm	AMNV = 36.61 cm/s	AMXV = 55.83 cm/s
ASMNV = 18.63 cm/s	ADMNV = 50.26 cm/s	DSMNVR = 2.70
SD(%) = +/- 2.42	SD(%) = +/- 5.09	SD(%) = +/- 4.77
ASMXV = 33.00 cm/s	ADMXV = 73.08 cm/s	DSMXVR = 2.21
SD(%) = +/- 2.02	SD(%) = +/- 4.44	SD(%) = +/- 4.72

Based on 7 heart beats

(b)

Fig. 9.4 - (a) Maximum velocity envelope, IWMV curve, ECG and pressure sampled from circumflex artery proximal to a stenosis site after angioplasty. (b) Parameters calculated from curves shown in Fig. 9.4.a. Male patient, age: 74.

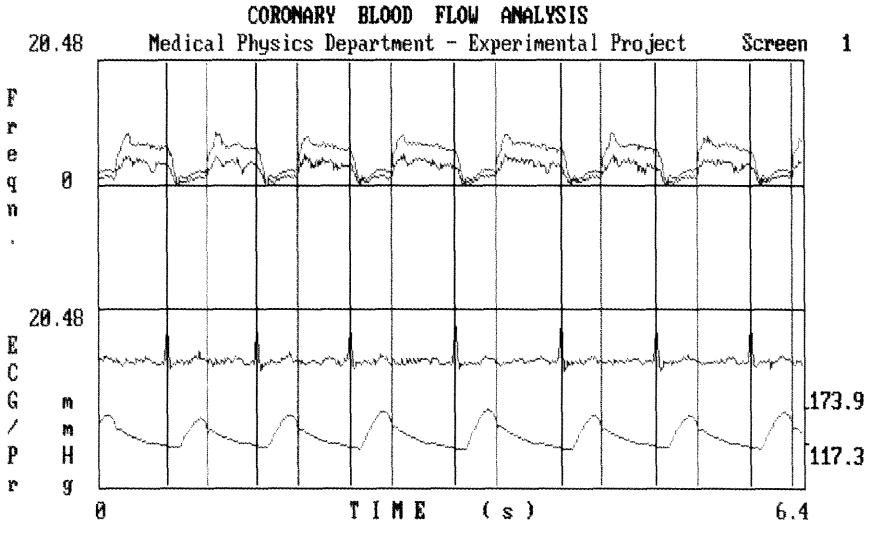

(a)

CORONARY BLOOD FLOW ANALYSIS
Medical Physics Department - LRI

PARAMETERS

H. R. = 67.33 bpm	AMNV = 10.39 cm/s	AMXV = 18.86 cm/s
ASMNV = 5.45 cm/s	ADMNV = 13.92 cm/s	DSMNVR = 2.55
SD(%) = +/- 4.36	SD(%) = +/- 2.99	SD(%) = +/- 2.00
ASMXV = 9.77 cm/s	ADMXV = 25.34 cm/s	DSMXVR = 2.59
SD(%) = +/- 2.57	SD(%) = +/- 1.09	SD(%) = +/- 2.77

Based on 7 heart beats

(b)

Fig. 9.5 - (a) Maximum velocity envelope, IWMV curve, ECG and pressure sampled from left coronary artery past a stenosis site before angioplasty. (b) Parameters calculated from curves shown in Fig. 9.5.a. Male patient, age: 52.

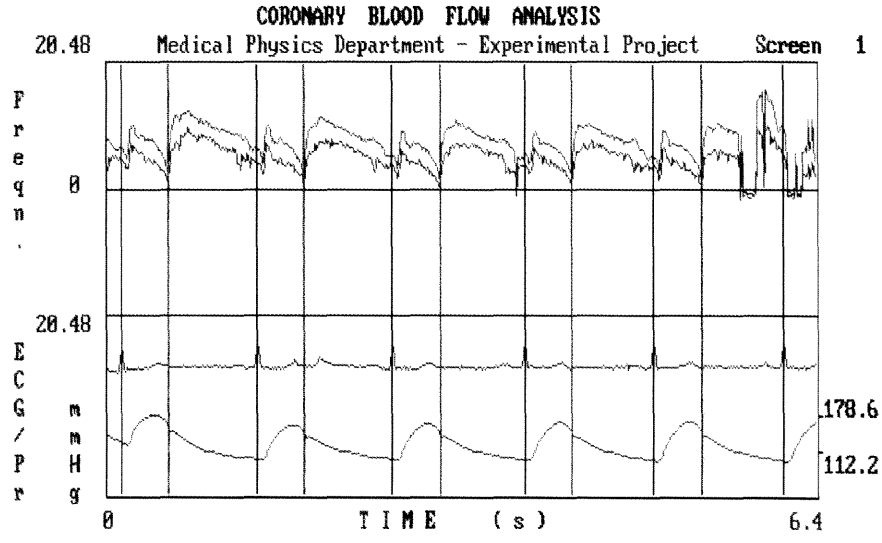

(a)

CORONARY BLOOD FLOW ANALYSIS
Medical Physics Department - LRI

PARAMETERS

H. R. = 50.21 bpm	AMNV = 20.51 cm/s	AMXV = 31.47 cm/s
ASMNV = 16.63 cm/s	ADMNV = 23.27 cm/s	DSMNVR = 1.40
SD(%) = +/- 10.44	SD(%) = +/- 11.82	SD(%) = +/- 3.75
ASMXV = 26.69 cm/s	ADMXV = 34.23 cm/s	DSMXVR = 1.28
SD(%) = +/- 7.36	SD(%) = +/- 8.41	SD(%) = +/- 1.67

Based on 5 heart beats

(b)

Fig. 9.6 - (a) Maximum velocity envelope, IWMV curve, ECG and pressure sampled from circumflex artery proximal to a stenosis site after angioplasty. (b) Parameters calculated from curves shown in Fig. 9.6.a. Male patient, age: 64.

Chapter 10 - Summary and Conclusion

In the recent years, many researchers have investigated the possibility of correlating blood flow velocity measurements in the coronary arteries (obtained with catheter-tipped Doppler transducers) with the presence and severity of stenosis. Techniques used for this purpose were discussed in Chapter 1. One of the aims of this work was to perform some basic measurements with a commercial Doppler system in order to verify the viability of applying these techniques in clinical practice.

To estimate flow velocities in the coronary circulation, a versatile microcomputer based system was developed to sample, process and store Doppler signals, ECG and pressure waveforms. It also allows parameters currently discussed in the literature to be calculated (Chapter 9). Sonograms and waveforms obtained with this system during angioplasty were presented in the previous chapters. The application of some digital signal processing techniques to obtain better velocity estimations and time-frequency resolution was also investigated.

The theoretical and experimental results presented in Chapters 6, 8 and 9 have shown that the presence of the catheter in a coronary artery and the small diameter of the ultrasound beam produced by the transducer, insufficient to insonate the whole lumen of the blood vessel, introduce artefacts into the velocity estimates. These artefacts may affect the measurements of coronary blood flow reserve and the application of the continuity equation. Technical improvements in the design of the catheter should be achieved to increase the accuracy of these measurements.

The developed system (Chapter 3) was also tested in clinical practice. It proved to be suitable for sampling, processing and storing the necessary data, constituting a flexible and powerful tool to carry out further researches in this field.

The compensation of phase and gain imbalance (Chapter 4), and the maximum frequency envelope detector proposed (Chapter 5) contribute to a better

performance of the system. Better time resolution can be achieved by processing Doppler signals off line (Chapter 7).

Doppler catheters provide further information on coronary circulation, but the poor accuracy of the blood flow velocity measurements preclude a reliable quantitative analysis of the data.

There is another type of Doppler transducer for coronary studies available in the market, known as Doppler guidewire, which has a smaller diameter and perhaps a wider sample volume (Doucette et al. 1992). A natural step in these studies would be to repeat the measurements described in this text for the Doppler guidewire. Such an investigation would verify if the guidewire is suitable for the current studies or if further technical improvements are required in order to obtain accurate measurements.

At this moment, it is difficult to predict whether the use of Doppler catheters may become a standard technique to assess the severity of stenosis. Currently, imaging systems based on ultrasound are being developed and becoming increasingly popular (Intracoronary Ultrasonic Imaging - ICUS). ICUS has been successfully used to characterise stenosis and outcome of angioplasty, overcoming problems present in angiography (Violaris et al. 1992; Fitzgerald and Yock 1993; Tobis et al. 1993). In view of this new technique, Doppler catheters may only be used in the future to assess the coronary microcirculation (White 1993) and as a research tool to characterise the coronary circulation under several clinical conditions.

Further investigation should be carried out to improve the blood flow velocity estimates and evaluate the clinical potentialities of this technique.

Appendix A - User Guide for the Developed Software

This appendix introduces the software developed, describing the options provided to process and store the waveforms discussed in Chapter 2, as well as those that allow files to be retrieved and examined.

The main menu of the software is presented in Fig. A-1. The options given by this menu are described below[1].

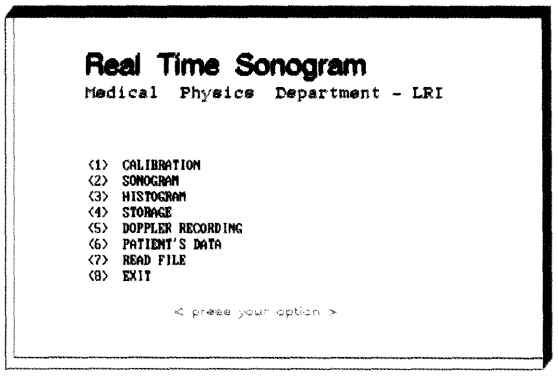

Fig. A.1 - Main menu of the developed software

<1> Calibration

Before sampling data, this option should be called to optimise the presentation of the ECG and blood pressure waveforms on the screen. When this option is selected, the software automatically calculates constants to divide the sampled values by in order to display the waveforms on an appropriate scale during the execution of the other routines. Fig. A.2 shows the screen for the calibration option and illustrates its mode of operation. The software tracks the maximum value of both curves and

[1]In the remainder of this appendix, the character between the symbols < > should be pressed to select the required option. If none is presented, any key other than those specified by the current menu may be used.

sets new constants to scale the waveforms. When the signals have their maximum values within the edges (broken lines), the procedure is finished. The user should then press any key to return to the main menu.

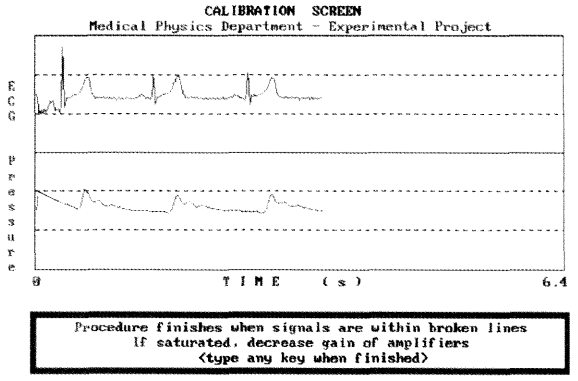

Fig. A.2 - Example of screen shown by the option <calibration>. In this mode, ECG and pressure waveforms are scaled to achieve their best presentation on the screen.

<2> Sonogram

Fig. A.3 presents the default acquisition screen for this option. The menu shown at the bottom of the screen specifies the present settings and the keys which should be used by the operator to change them.

The operator may choose to observe the ECG and pressure waveforms instead of the sonogram of the reverse flow, switching the mode of presentation (</>). Fig. A.4 illustrates this optional mode. The ECG and pressure signals are also sampled in the default mode, though not shown. They are printed and stored with the sonogram as described later.

The sampling frequency may be set to the following rates: 20.48, 40.96, 54.62 and 81.92 kHz.

To eliminate artefacts due to wall movements, the operator can adjust the cut-off frequency of the 'wall thump' filters using lateral arrows.

The gain of the input amplifiers of the A/D board, which sample the quadrature Doppler signals, can be increased if the quality of the sonogram is poor. In case of excessive gain, an overload message appears in the top right hand corner of the screen. In this situation, the gain must be decreased to assure correct results.

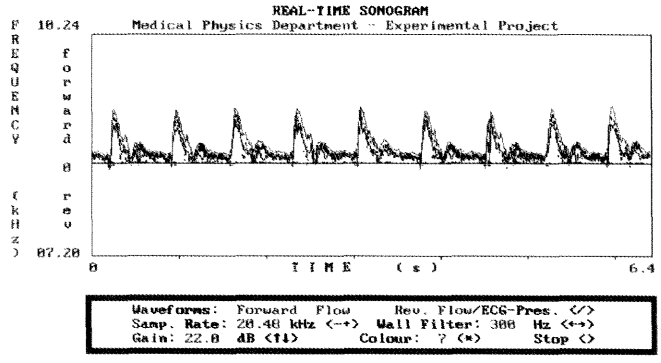

Fig. A.3 - Default screen for the <sonogram> option. It presents the sonogram of the forward and reverse flow and a menu with the present settings.

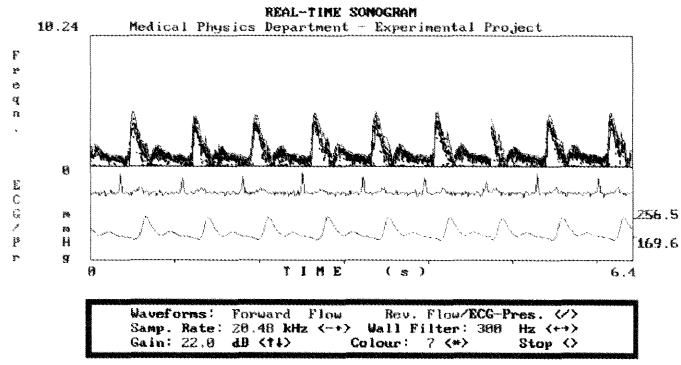

Fig. A.4 - Example of screen for the <sonogram> option where the operator has chosen to observe the sonogram of the forward flow, ECG and pressure waveforms.

The last option (Colour <*>) allows the operator to change the threshold used to set the colour scale in order to improve the sonogram presentation.

The acquisition procedure, for both modes of presentation, is interrupted by pressing any other key. The menu is then replaced by a new one (Fig. A.5). The averaged mean and maximum velocities are also given based on the curves shown on the screen. These values are calculated for an angle of 0° between the ultrasound transducer and the vessel wall, and an emitted frequency of 20 MHz. If other angles or carrier frequencies are used, the velocity values should be corrected according to the Doppler equation (Eq. 2.1)[2].

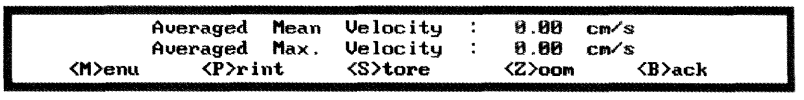

Fig. A.5 - Menu presented by the <sonogram> option when the procedure is stopped.

The option <Back> reinitialises the sampling procedure. The option <Menu> returns the software to the main menu. The option <Print> prints the patient data (these should have been previously inserted by choosing the option <6> of the main menu as described below) together with the content of the screen. An example of the print out is given in Fig. A.6. As can be seen, the ECG and pressure waveforms are printed, even if the presentation mode does not show them on the screen. If the printer is not ready, the messages below may appear on the screen, specifying the problem:

"Printer off - <C>ancel <P>rint",

[2]The examples presented in this appendix were obtained from healthy volunteers through a non-invasive Doppler system (Vasoflo - Sonicaid) and a non-invasive pressure monitor (Finapres - Ohmeda). Note that the values of pressure and velocity presented in the examples do not correspond to the actual values since the constants used to calculate them were set, considering the use of the equipment described in Chapter 2.

REAL TIME SONOGRAM

MEDICAL PHYSICS DEPARTMENT - LRI

Patient's Data

Surname : *Moraes* **First name :** *Raimes*

Sex : *M* **Age :** *30* **Weight :** *70 Kg*

Born : *28/08/64* **Date :** *06/02/95*

Notes :

Fig. A.6.a - Example of print out of patient data.

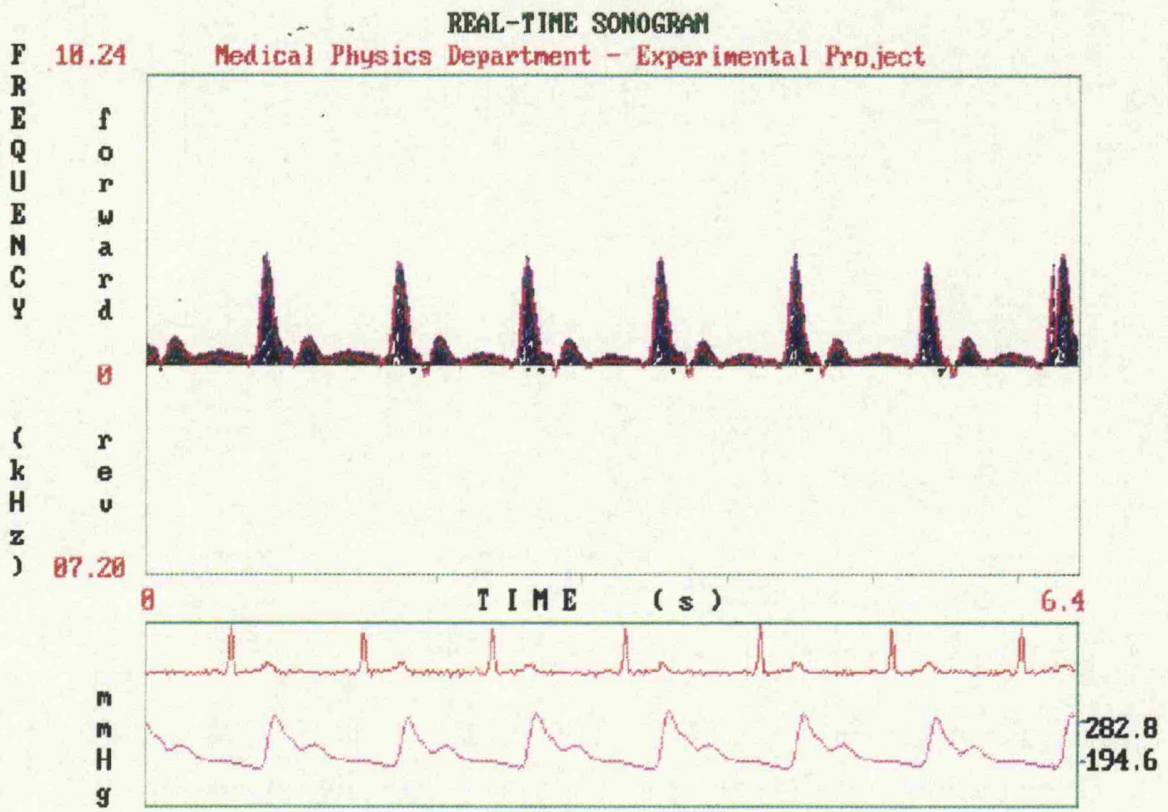

Fig. A.6.b - Example of print out of sonogram, ECG and pressure waveforms.

"Out of paper - <C>ancel <P>rint",
"Printer off line - <C>ancel <P>rint".

For any of these cases, the user should check the printer and press a key according to his/her choice.

When the option <Store> is selected, the software asks for the name of the file. The name should not have more than 8 characters. The extension *.DOC is automatically inserted by the software. The data stored contain information on the system settings, patient data, copy of the screen, ECG and pressure waveforms (More information on the organisation of these files, and others described in this appendix, can be obtained in Appendix B). After inserting the file name, the following messages may appear:

"File already present: <R>ename <C>ontinue <>Abort"
"Disk full - <A>bort <N>ew disk"
"Write protected disk - change <>"
"Drive not ready or bad disk - <A>bort <R>etry"

The messages point out the action to be taken in order to store the files if any problem has occurred. Messages indicating file writing and completion are presented when the file is being stored.

The option <Zoom> shows a bar under the main frame (Fig. A.7) that can be displaced in order to select a region of the sonogram to be displayed on a different time scale. This was implemented to allow a better visualisation of a particular segment. Fig. A.8 shows the magnified segment. The menu given by this option

allows the screen to be printed (<Print>), return to the main menu (<>exit) and re-initialisation of the sampling procedure (<Continue>).

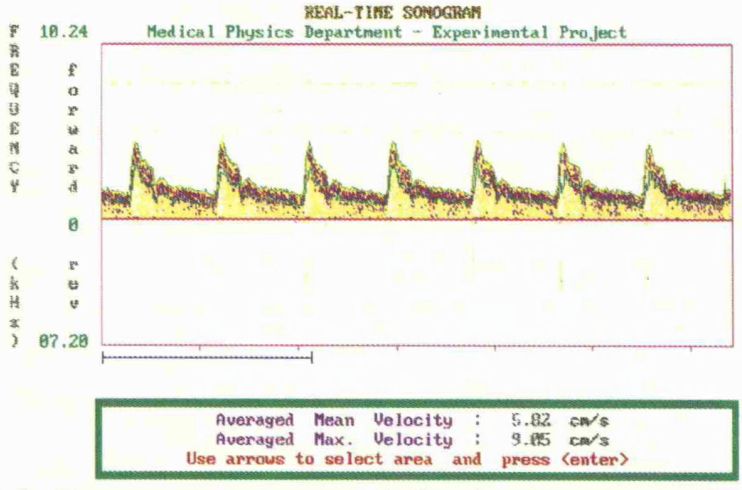

Fig. A.7 - Example of screen presented when the option <zoom> is selected.

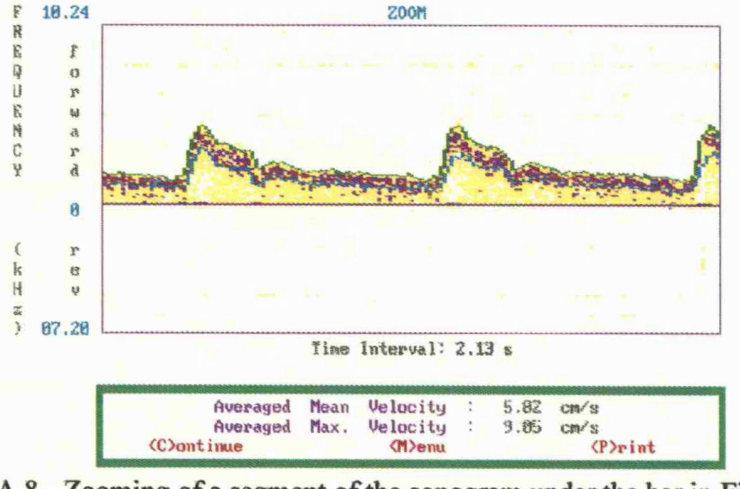

Fig. A.8 - Zooming of a segment of the sonogram under the bar in Fig. A.7.

<3> Histogram

When this option is selected, a screen presenting the sonogram of forward and reverse flow (similar to Fig. A.2) is shown. When the user stops the acquisition procedure, a window replaces the menu, displaying the sampled signals of pressure

and ECG. The R wave detections are also shown (Fig. A.9). The algorithm used to detect the R wave is the same as that described in Chapter 9.

Three new options allow the user to reinitialise the signal acquisition (<Back>) or return to the main menu (<Menu>) or calculate the histogram (<Go>). For this last option, all recorded cycles, limited by two consecutive detections of the R wave, are summed in a matrix whose number of columns is made equal to the number of columns of the longest cycle. The number of lines of this matrix is equal to the number of lines of the data shown on the screen: 216. The averaged power of each column is found, dividing their resultant value by the number of summed columns (it may be different for the last resultant columns of the matrix since the period of each cycle should differ slightly). The neighbour columns are summed to reduce their number to 20 arrays of data, producing 20 lines of histogram. Their magnitudes are normalised to the highest value obtained and are plotted perpendicular to the time-frequency plane. This histogram provides an idea of the distribution of the scattered ultrasound power along a cardiac cycle. An example of the histogram obtained is shown in Fig. A.10.

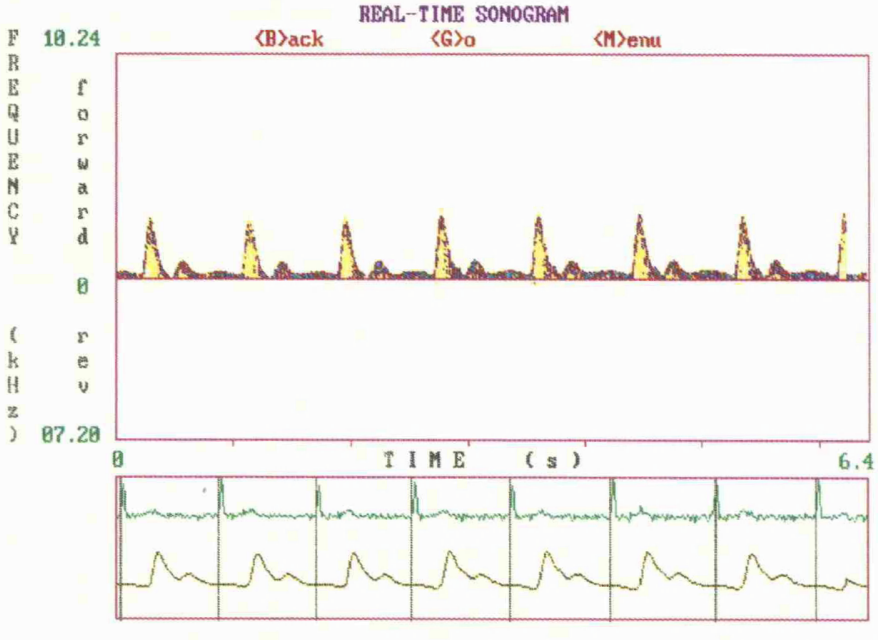

Fig. A.9 - Example of screen presented for the <histogram> option. The sonogram for forward and reverse flow, ECG and pressure waveforms are presented. The detection of the R wave is shown by vertical lines in the bottom window.

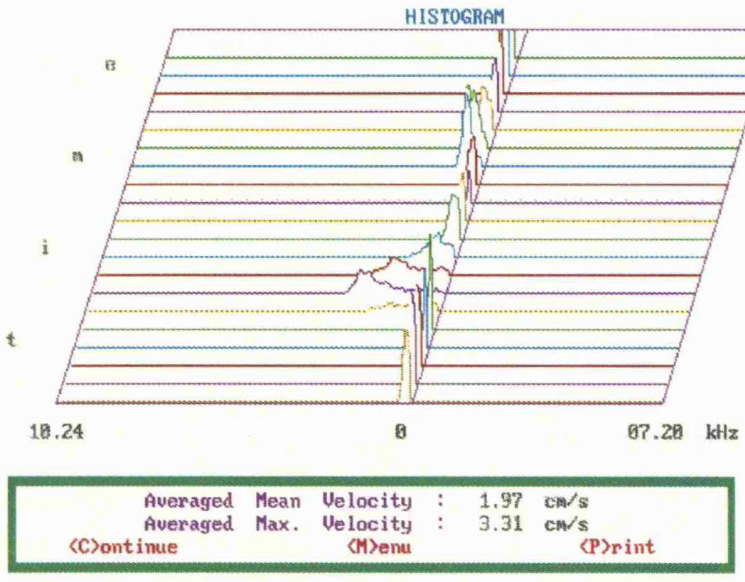

Fig. A.10 - Example of histogram obtained by averaging the scattered ultrasound power of the cardiac cycles shown in Fig. A.9.

<4> Storage

In this option, up to 6 minutes of the envelopes of the sonogram, ECG and pressure curves are stored in the PC memory. When the buffer is full, the software automatically stops their acquisition and their presentation on the screen. These data, together with the system settings and patient data, can be saved in disk files to be processed by another program (Chapter 9). The screen shown by this option is the same as that presented in Fig. A.4; the sonogram for the reverse flow is not displayed. If the sampling rate is changed, the previously stored information in the memory is discarded. This happens because the velocity estimations are based on the sampling rate and it would increase the software complexity and memory requirements to register changes of sampling rate. Before changing the sampling rate, previously stored data in the memory should be saved on disk if they are of interest. When the acquisition is automatically stopped, a menu is shown (Fig. A.11). The acquisition procedure can also be terminated by the user through the keyboard and the new menu will be presented.

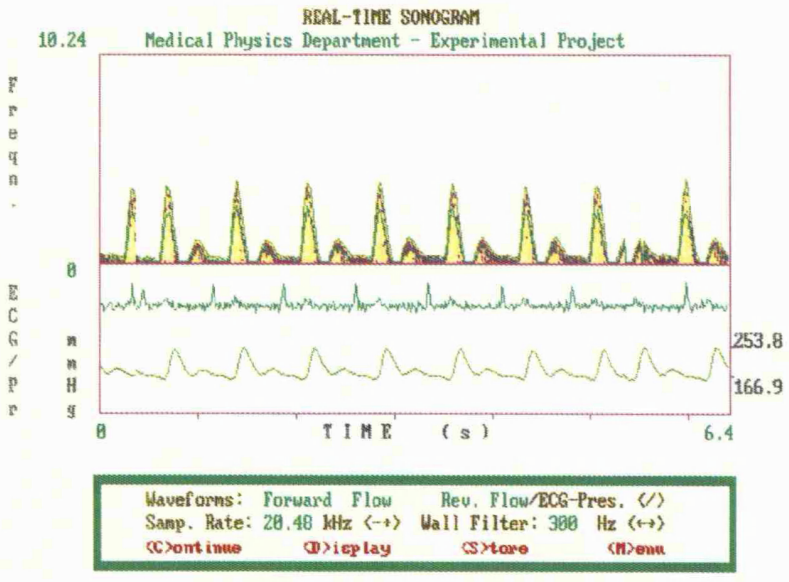

Fig. A.11 - An example of the screen presented by the option <Storage> when the acquisition is terminated by the user.

The option <Menu> returns the software to the main menu. The option <Continue> reinitialises the acquisition procedure (the previously stored data in the PC memory are discarded). The option <Store> behaves like that of the same name described above. For this mode, the files are saved with the extension *.STR. The option <Display> allows the user to verify the curves stored in the memory before loading them onto disk. The sonogram envelopes are presented on a smaller scale to allow the presentation of both forward and reverse curves together with the other waveforms (Fig. A.12). The waveforms are successively shown, by pressing the option <Display>, from the first screen to the last one, and then, back to the first in a circular way. In the top right hand corner of the display, an index of the screen being shown is presented.

<5> Doppler Recording

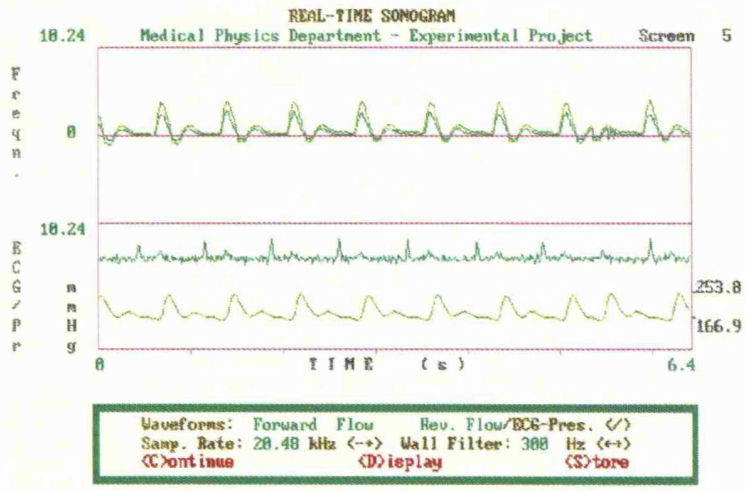

Fig. A.12 - An example of the screen for displaying the waveforms kept in the memory during execution of <Storage> option.

In this mode, 640 kbytes of sampled quadrature Doppler signals are stored in the PC memory. The sonogram for forward and reverse flow, corresponding to the stored data, is shown on the screen at the time of their acquisition. The time interval stored will depend on the sampling rate used. When the buffer is full, the acquisition procedure finishes and a menu is presented (Fig. A.13). Optionally, the user can stop the acquisition at any time by pressing any key. In this mode, the envelopes, ECG and pressure waveforms are not shown. The transport of data from the DSP board memory to the PC memory takes much of the PC's processing power and does not allow other tasks to be performed simultaneously.

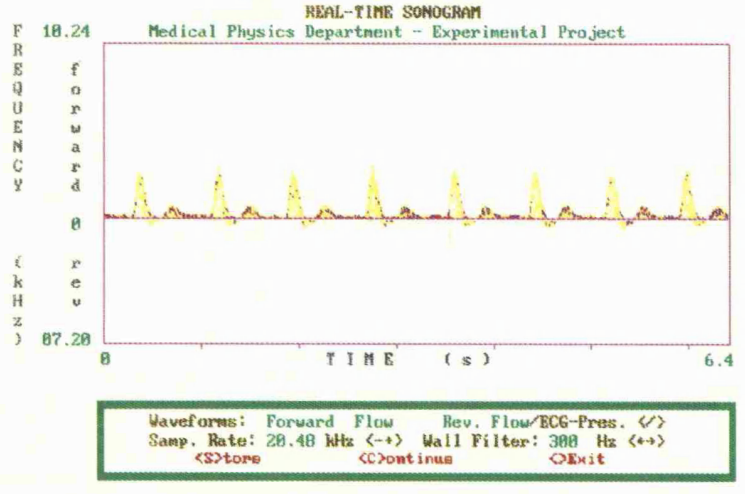

Fig. A.13 - Example of screen presented by the option <Doppler recording> when the acquisition procedure is automatically stopped.

The new menu allows the user to reinitialise the procedure (<Continue>), discarding the data already stored in the memory, and return to the main menu (<>Exit). The option <Store> transfers the data from the memory to a disk file, saving also the system settings and patient data. This option works in a similar way to the store functions described above. The files are stored with the extension *.DOP.

<6> Patient's Data

This option allow the user to insert patient data that will be printed (as described above) or stored in the three different types of files generated. The screen presented by this option is shown in Fig. A.14. The routine developed to allow the insertion of the data is very simple, since the amount of information is small. A cursor will appear in the first field of the screen. After typing the data, the user has to use the key *Backspace* to introduce any modification in the inserted information. By pressing *Enter*, the user moves the cursor to the next field. It is not possible to return to the previous field. The user can cancel the insertion of data by pressing the key *ESC*. After inserting the last field and pressing *Enter*, the software returns to the main menu.

After inserting the data, these can be consulted by choosing the same option <6> in the main menu. For this case, a screen with the data inserted is shown (Fig. A.15) presenting two options which allow the user to return to the main menu or introduce the data of another patient.

The patient data is kept in the memory to be printed and saved in all files stored from then on, since several files are usually stored for each patient.

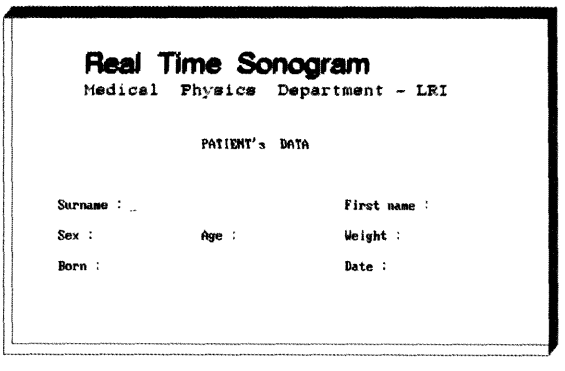

Fig. A.14 - Screen presented by the option <Patient's data> to allow the insertion of patient data by the user.

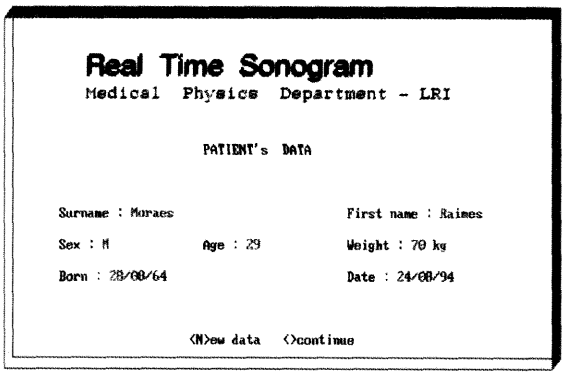

Fig. A.15 - Example of screen presented by the option <Patient's data> when data were previously inserted.

<7> Read File

This option allows two kind of files to be retrieved from disk files and presented on the screen. When this option is activated, the next screen asks the user to choose between two type of files: sonograms (extension *.DOC) and waveforms

(extension *.STR). Software to process the files *.DOP is described in Chapter 7. After this choice, the files of the specified type, present in the directory, are listed on the screen and the name of the file to be retrieved is requested (Fig. A.16).

The data read are shown on a screen similar to that used for their acquisition. After their presentation the software returns to the main menu following the pressing of any key. The retrieved patient data may be consulted using option <6> of the main menu. The data is presented as shown in Fig. A.15.

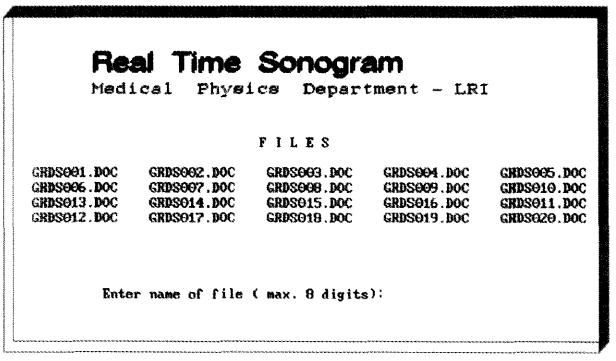

Fig. A.16 - Example of the screen presented by the option <Read file>. The name of the files of the type selected are listed.

<8> Exit

By using this option, the operator can return to the operating system.

Appendix B - File Organisation

The aim of this appendix is to describe how the three kinds of files stored by the system developed are organised. This gives the necessary information for the development of other software able to process the content of these data files.

***.DOC Files**

This sort of file keeps a hardcopy of the PC screen which is very useful to allow a qualitative assessment of the processed data. Since the signals are updated on the screen from left to right during their acquisition, they are usually not time ordered On storing the information, the storage routine orders the sonogram from the first to the last acquired column of those shown on the screen. This avoids the presence of discontinuities in the data read from the stored files, simplifying their interpretation. These files store 512 columns of the sonogram (one screen), and the last 512 samples of the ECG and pressure signals. The ECG and pressure waveforms are also arranged on the same timebase to keep their correspondence to the events of the sonogram.

These data files have their contents organised in the following order:

1 - Byte (8 bits) containing information on the kind of sonogram storage:

value 1 = reverse flow was stored,
value 0 = reverse flow was not stored.

2 - Byte containing information on the sampling frequency:

value 0 = sampling frequency equal to 81.92 kHz,
value 1 = sampling frequency equal to 54.62 kHz,
value 2 = sampling frequency equal to 40.96 kHz,
value 3 = sampling frequency equal to 20.48 kHz.

3 - Word (16 bits) containing the number by which the amplitude of the ECG samples are divided in order to allow the presentation of the waveform on the screen within a vertical spacing of 36 pixels (refer to Appendix A).

4- Word containing number by which the digital pressure samples are divided in order to allow the presentation of the curve on the screen within a vertical spacing of 36 pixels (refer to Appendix A).

5 - Word containing the mean value of the blood pressure curve sampled. This value is the result of the analog to digital conversion. To obtain the pressure value in mmHg, the stored word should be divided by 54.72 (constant obtained by applying a known pressure to the transducer and reading the result of the conversion).

6 - Sequence of 7 strings containing patient data: surname, first name, sex, age, weight, date of birth, date of examination. All strings have a maximum of 30 characters. The end of each string is indicated by the presence of a newline character ('/n').

7 - Bytes containing information on the colour of each pixel of the sonogram. As the sonogram has a maximum of 16 colours, it is possible to store the information of two consecutive pixels in one byte saving disk space. The columns of the sonogram are stored consecutively from the top to the bottom having 216 (0-215) colour coded pixels if reverse flow is stored or 126 (0-125) otherwise. The stored bytes keep information on the even pixels in the four most significant bits and on the odds in the four least significant bits.

8 - Words containing the ECG and pressure waveforms. 512 samples of each signal are stored. These samples are interleaved in 1024 bytes. The even words (0, 2,.., 1022) keep the ECG samples and the odd words (1, 3,.., 1023), the blood pressure samples.

***.STR Files**

These files contain the detected maximum frequency envelope (MFE) and the calculated IWMF curve of the sonogram; the sampled ECG and blood pressure waveforms. These curves are used to calculate parameters (Chapter 9) that may be correlated with the clinical case analysed. These files usually have different sizes, therefore their retrieval should be completed when *end of file* [EOF] is found.

The first 5 fields of this kind of file are identical to fields 2 to 6 of the *.DOC files. The remaining field is described below.

6 - This field stores the curves mentioned above. The data are interleaved in the following order:

- byte containing MFE detection (bin number),
- byte containing calculated IWMF (bin number),
- word containing ECG sample,
- word containing pulsatile blood pressure sample,
- word containing mean blood pressure sample.

The bin numbers may be converted to velocity values using the Doppler equation (Eq. 2.1) and knowing the FFT resolution. The pressure samples contain the results of the analog to digital conversion. Mean pressure values in mmHg can be obtained by dividing the sampled values by 54.72. Pulsatile pressure values in mmHg can be obtained by summing their sampled values to the mean values and dividing the result by the same constant.

***.DOP Files**

These files contain samples of the quadrature Doppler signals allowing their off-line analysis.

The first 5 fields of this kind of file are identical to fields 2 to 6 of the *.DOC files. The last field keeps the sampled data:

6 - 640 kbytes of sampled Doppler signals. The samples of the two channels are interleaved. The even words contain the in-phase samples and the odd words, the quadrature ones.

Appendix C - Circuit of Amplifier

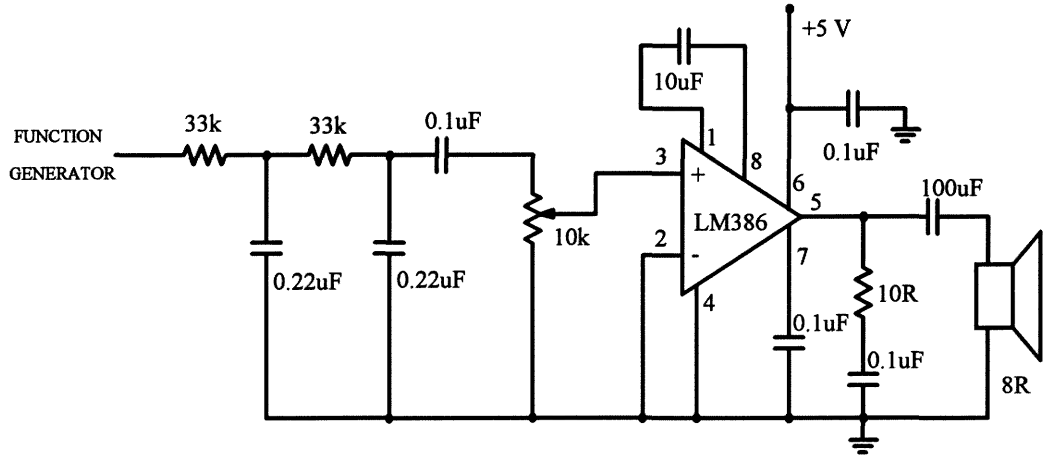

Fig. C.1 - Diagram of amplifier used to drive the speaker of the set-up utilised in the sample volume measurements described in Chapter 6.

References

Ahlstrom ML, Tompkins WJ (1985): 'Digital filters for real-time ECG signal processing using microprocessors', IEEE Trans. Biomed. Eng., BME 32, 708-713.

Arnett EN, Isner JM, Redwood DR et al. (1979): 'Coronary artery narrowing in coronary heart disease: comparison of cineangiographic and necropsy findings', Ann. Inter. Med., 91, 350-356.

Arts MGJ, Roevros JMJG (1972): 'On the instantaneous measurement of blood flow by ultrasonic means', Med. Biol. Eng. Comput., 10, 23-34.

Atkinson P, Woodcodk JP (1982): 'Doppler ultrasound and its use in clinical measurement', Academic Press, London.

Aydin N, Evans DH (1994): 'Implementation of directional Doppler techniques using a digital signal processor', Med. Biol. Eng. Comput., 32, S157-S164.

Baraniuk RG, Jones DL (1993): 'A signal-dependent time-frequency representation: optimal kernel design', IEEE Trans. Signal Processing, 41, 1589-1601.

Beaver WL (1974): 'Sonic nearfields of a pulsed piston radiator', J. Acoust. Soc. Am., 56, 1043-1048.

Bendat JS, Piersol AG (1986): 'Random data: analysis and measurement procedures', John Wiley & Sons, New York.

Bierman EL (1991): 'Atherosclerosis and other forms of arteriosclerosis' in Harrison's principles of internal medicine, Wilson JD, Braunswald E, Isselbacher KJ, Peterssdorf RG, Martin JB, Fauci AS, Root RD (Eds.), McGrawn Hill, New York.

Block PC (1986): 'Balloon angioplasty' in Intracoronary interventions: balloon and laser angioplasty, The Upjohn Company, Michigan, USA.

Brigham EO (1974): 'The fast Fourier transform', Prentice-Hall, Englewood Cliffs, New Jersey.

Burton AC (1977): 'Fisiologia e Biofísica da Circulação', Guanabara-Koogan Editora, Rio de Janeiro.

Bush G, Evans DH (1993): 'Digital audio tape as a method of storing Doppler ultrasound signals', Physiol. Meas., 14, 381-386.

Carlson BA (1986): 'Communication systems', McGraw-Hill Inc., New York.

Caro CG, Pedley TJ, Schrother RC, Seed WA (1978): 'The mechanics of circulation', Oxford University Press, Oxford.

Choi H, Williams JW (1989): 'Improved time-frequency representation of multicomponent signals using exponential kernels', IEEE Trans. Acoust., Speech, Signal Processing, ASSP-37, 862-871.

Claasen TACM, Mecklenbrauker WFG (1980): 'The Wigner-distribution - a tool for time-frequency signal analysis - Part I', Phillips J. Res., 35, 217-250.

Cobbold RSC (1974): 'Transducers for biomedical measurements', John Wiley & Sons, New York.

Cobbold RSC, Veltink PH, Johnston KW (1983): 'Influence of beam profile and degree of insonation on the CW Doppler ultrasound spectrum and mean velocity', IEEE Trans. Sonics Ultrasonics, SU-30, 364-370.

Coghlan BA, Taylor MG (1976): 'Directional Doppler techniques for detection of blood flow velocities', Ultrasound Med. Biol., 2, 181-188.

Cohen L (1966): 'Generalized phase-space distribution functions', Math. Phys., 7, 781-787.

D'Alessio T (1985): 'Objective algorithm for maximum frequency estimation in Doppler spectral analysers', Med. Biol. Eng. Comput., 23, 63-68.

Darlington S (1950): 'Realization of a constant phase difference', Bell Sys. Tech. J., 29, 94-104.

Denardo SJ, Talbot L, Hargrave VK, Fitzgerald PJ, Selfridge AB, Yock PG (1994): 'Analysis of pulsed wave Doppler ultrasound spectra obtained from a model intracoronary catheter', IEEE Trans. Biomed. Eng., 41, 635-648.

DiMario C, Roelandt JRTC, Jaegere P, Linker DT, Oomen J, Serruys PW (1993): 'Limitations of the zero crossing detector in the analysis of intracoronary Doppler', Cath. Card. Diag., 28, 56-64.

Doucette JW, Corl PD, Payne HM, Flynn AE, Goto M, Nassi M, Segal J (1992): 'Validation of a Doppler guide wire for intravascular measurement of coronary artery flow velocity', Circulation, 85, 1899-1911.

Dvinsky AS, Ojha M (1994): 'Simulation of three-dimensional pulsatile flow trough an asymmetric stenosis', Med. Biol. Eng. Comput., 32, 138-142.

Evans DH (1982): 'Some aspects of the relationship between instantaneous volumetric blood flow and CW Doppler ultrasound recordings - III', Ultrasound Med. Biol., 11, 735-741.

Evans DH, McDicken WN, Skidmore R, Woodcock JP (1989): 'Doppler ultrasound: instrumentation and clinical applications', John Wiley & Sons; Chichester.

Factor SM, Bach RJ (1994): 'Pathophysiology of Myocardial Ischemia', in The heart, Schlant RC and Alexander RW (Eds.), McGraw-Hill Inc., New York.

Fitzgerald PJ, Yock PG (1993): 'Mechanisms and outcomes of angioplasty and atherectomy assessed by intravascular ultrasound imaging', J. Clin. Ultrasound, 21, 579-588.

Flandrim P (1984): 'Some features of time-frequency representations of multicomponent signals', Proc. IEEE Int. Conf. ASSP, 3, 41B.4.1-41B.4.4.

Folts JD, Kahn DR, Bittar N, Rowe GG (1975): 'Effects of partial obstruction on phasic in aortocoronary grafts', Circulation, 51/52(suppl I), I-148.

Franch RH, King III SB, Douglas Jr JS (1986): 'Techniques of cardiac catheterization including coronary arteriography', in The heart, Hurst JW Editor-in-chief, McGraw-Hill Inc, New York.

Gibbons DT, Evans DH, Barrie WW, Cosgriff PS (1981): 'Real time calculation of Ultrasonic pulsatility index', Ultrasound Med. Biol., 19, 28-34.

Gosling RG, Dunbar G, King DH, Newman DL, Side CS, Woodcock JP, Fitzgerald DE, Keates JS, MacMillan D (1971): 'The quantitative analysis of occlusive peripheral arterial disease by a non-intrusive ultrasonic technique', Angiology, 22, 52-55.

Gosling RG, King DH, Newman DL, Woodcook JP (1969): 'Transcutaneous measurement of arterial blood velocity by ultrasound', Ultrasonic for industry 1969, conference papers, 16-23.

Goss SA, Johnston RL, Dunn F (1978): 'Comprehensive compilation of empirical ultrasonic properties of mammalian tissues', J. Acoust. Soc. Am., 64, 423-457.

Gould KL, Lipscomb K, Hamilton GW (1974): 'Physiological basis for assessing critical coronary stenosis: Instantaneous flow response and regional distribution during coronary hyperaemia as measures of coronary flow reserve', Am. J. Cardiol., 33, 87-94.

Guo Z, Durand LG, Allard L, Cloutier G, Lee HC, Langlois YE (1993): 'Cardiac blood flow analysis-part 1', Med. Biol. Eng. Comput., 31, 237-241.

Hall DP, Gruentizig AR (1986): 'Technique of percutaneous transluminal angioplasty of the coronary, renal, mesenteric and peripheral arteries', in The heart, Hurst JW Editor-in-chief, McGraw-Hill Inc., New York.

Harris FJ (1978): 'On the use of windows for harmonic analysis with discrete Fourier transform', Proc. IEEE, 66, 51-83.

Hoeks APG, Ruissen CJ, Hick P, Reneman RS (1984): 'Methods to evaluate the sample volume of pulsed Doppler systems', Ultrasound Med. Biol., 10, 427-434.

Hongo M, Nakatsuka T, Watanabe N et al. (1994): 'Effects of heart rate on phasic coronary blood flow pattern and flow reserve in patients with normal coronary arteries: A study with an intravascular Doppler catheter and spectral analysis', Am. Heart J., 127, 545-551.

Hoskins PR, Loupas T, McDicken WN (1990): 'A comparison of the Doppler spectra from human blood and artificial blood used in a flow phanton', Ultrasound Med. Biol., 16, 141-147.

Hurst JW, King III SB, Friesinger GC, Walter PF, Morris DC (1986): 'Atherosclerotic coronary heart disease: recognition, prognosis and treatment', in The heart, Hurst JW Editor-in-chief, McGraw-Hill Inc, New York.

Johnson EL, Yock PG, Hargrave VK, Srebro JP, Manubens SM, Seiz W, Ports TA (1989): 'Assessment of severity of coronary stenosis using a Doppler catheter: validation of a method based on the continuity equation', Circulation, 80, 625-635.

Johnston KW, Maruzzo BC, Cobbold RSC (1978): 'Doppler methods for quantitative measurement and localization of peripheral arterial occlusive disease by analysis of the blood flow velocity waveform', Ultrasound Med. Biol., 4, 209-223.

Jones DL, Parks TW (1990): 'A high resolution data-adaptative time frequency representation', IEEE Trans. Acoust., Speech, Signal Processing, 38, 2127-2135.

Jones EL, Hatcher CR (1986): 'Techniques for the surgical treatment of atherosclerotic coronary artery disease and its complications', in The heart, Hurst JW Editor-in-chief, McGraw-Hill Inc, New York.

Jorgensen JE, Campau DN, Baker DW (1973): 'Physical characteristics and mathematical modelling of the pulsed ultrasonic flowmeter', Med. Biol. Eng., 404-421.

Kagiyama M, Ogasawara Y, Tsujioka K, Kajiya F (1988): 'Estimation of the catheter induced flow disturbance in the blood velocity measurements by a

numerical simulation', Proceedings of the 11th Osaka University Biomedical Engineering Research Meeting, 25-30 (in Japanese - cited by Tadaoka et al. 1990).

Kajiya F, Ogasawara Y, Tsujioka K et al. (1986): 'Evaluation of human coronary blood flow with an 80 channel 20 MHz pulsed Doppler velocimeter and zero-cross and Fourier transform methods during cardiac surgery', Circulation, 74 (suppl. III), III53-III60.

Kannel WB, Thom TJ (1986): 'Incidence, prevalence and mortality of cardiovascular diseases', in The heart, Hurst JW Editor-in-chief, McGraw-Hill Inc, New York.

Kassam M, Johnston KW, Cobbold RSC (1985): 'Quantitative estimation of spectral broadening for the diagnosis of carotid arterial disease: method and *in vitro* results', Ultrasound Med. Biol., 11, 425-433.

Keegan J, Firmin D, Gatehouse P, Longmore D (1994): 'The aplication of breath hold phase velocity mapping techniques to the measurement of coronary artery blood flow velocity: phantom data and initia *in vivo* results', MRM, 31, 526-536.

Kern MJ, Donohue TJ, Bach RG, Aguirre FV, Caracciolo EA (1993): 'Quantitating coronary collateral flow velocity in patients during coronary angioplasty using a Doppler guidewire', Am. J. Cardiol., 71, 34D-40D.

Kikuchi S, Okuyama D, Kasai C, Yoshida Y (1972): 'Measurements in the sound velocity and absorption of human blood in 1-10 MHz frequency range', Rec. Eletct. Commun. Eng. Convers., Tohoku Univ., 41, 152-159.

Kinsler LE, Frey AR, Coppens AB, Sanders JV (1982): 'Fundamentals of acoustics', John Wiley & Sons, New York.

Kitney RL, Talhami H (1987): 'The zoom Wigner transform and its application to the analysis of blood velocity waveforms', J. Theor. Biol., 129, 395-409.

Ku DN, Giddens DP, Phillips DJ, Strandness Jr DE (1985): 'Hemodynamics of the normal human carotid bifurcation: *in vitro* and *in vivo* studies', Ultrasound Med. Biol., 11, 13-26.

Kuo IY, Shung KK (1994): 'High frequency ultrasonic backscatter from erythrocyte suspension', Ultrasound Med. Biol., 41, 29-34.

Law YF, Bascom PAJ, Johnston KW, Vaitkus P, Cobbold RSC (1991): 'Experimental study of the effects of pulsed Doppler sample volume size and position on the Doppler spectrum', Ultrasonics, 29, 404-410.

Law YF, Johnston KW, Routh HF, Cobbold RSC (1989): 'On the design and evaluation of a steady flow model for Doppler ultrasound studies', Ultrasound Med. Biol., 15, 505-516.

Lee BB, Furgason ES (1980): 'Beam profiling using correlation systems', Ultrasonics, 18, 249-254.

Liepsch D, Moravec S (1984): 'Pulsatile flow of non-Newtonian fluid in distensible models of humans arteries', Biorheology, 21, 571-.576.

Lima CEG, Gandra ST, Caprihan A, Nobre F, Schilindwein F (1983): 'Algorítmo para a detecção de QRS em microcomputadores', Caderno de Eng. Biomédica-RBE, 1, N. 2, 5-16.

Lockwood GR, Ryan LK, Junt JW, Foster FS (1991): 'Measurement of the ultrasonic properties of vascular tissues and blood from 35-65 MHz', Ultrasound Med. Biol., 653-666.

Lunt MJ (1975): 'Accuracy and limitations of the ultrasonic Doppler blood velocimeter and zero crossing detector', Ultrasound Med. Biol., 2, 1-10.

Mancini GBJ, McGillem MJ, DeBoe SF, Gallagher KP (1989): 'The diastolic hyperemic flow versus pressure relation: a new index of coronary stenosis severity and flow reserve', Circulation, 80, 941-950.

Marasek K, Novicki A (1994): 'Comparison of the performance of three maximum Doppler frequency estimators coupled with different spectral estimation methods', Ultrasound Med. Biol., 20, 629-638.

Marcus ML (1983): 'Coronary circulation in health and disease', McGraw-Hill, New York.

Marple Jr. SL (1987): 'Digital spectral analysis with applications', Prentice-Hall Inc., Englewood Cliffs, New Jersey.

Martin W, Flandrim P (1985): 'Wigner-Ville spectral analysis of non-stationary processes', IEEE Trans. Acoust., Speech, Signal Processing, ASSP-33, 1461-1470.

McGinn AL, White CW, Wilson RF (1990): 'Interstudy variability in coronary flow reserve: the importance of heart rate, arterial pressure, and ventricular preload', Circulation, 81, 1319-1330.

Millman J (1979): 'Micro-electronics', McGraw-Hill, New York.

Milnor WR (1980): 'Properties of cardiac tissues' in Medical Physiology, Mountcastle VB (Ed.), The CV Mosby Company, St. Louis, Missouri.

Milnor WR (1980): 'The heart as a pump', in Medical Physiology, Mountcastle VB (Ed.), The C.V. Mosby Company, St. Louis, Missouri.

Mo LYL, Cobbold RSC (1986): 'A stochastic model of the backscattered Doppler ultrasound from blood', IEEE Trans. Biomed. Eng., BME 33, 20-27.

Mo LYL, Yun LC, Cobbold RSC (1988): 'Comparison of four digital maximum frequency estimators for Doppler ultrasound', Ultrasound Med. Biol., 14, 355-363.

Nakatani S, Yamnagishi M, Tamai J, Takaki H, Haze K, Miyatake K (1992): 'Quantitative assessment of coronary artery stenosis by intravascular Doppler catheter technique: application of the continuity equation', Circulation, 85, 1786-1791.

Neuman MR (1978): 'Biopotential amplifiers' in Medical instrumentation: application and design, Webster JG (Ed.), Houghton Mifflin Company, Boston.

Nichols WN, O'Rourke MF (1990): 'McDonald's blood flow in arteries', Edward Arnold, Melbourne.

O'Rourke RA (1986): 'Physical examination of the arteries and veins (including blood pressure determination)', in The heart, Hurst JG Editor-in-chief, McGrawn-Hill, New York.

Oates CP (1991): 'Towards an ideal blood analog for Doppler ultrasound phantoms', Physics in Medicine and Biology, 36, 1433-1442.

Ofili EO, Kern MJ, Labovitz AJ, Vrain JAS, Segal J, Aguirre FV, Castello R (1993): 'Analysis of coronary blood flow velocity dynamics in angiographically normal and stenosed arteries before and after endolumen enlargement by angioplasty', JACC, 21, 308-316.

Ojha M, Cobbold RSC, Johnston KW, Hummel RL (1990): 'Detailed visualization of the pulsatile flow fields produced by modelled arterial stenoses', J. Biomed. Eng., 12, 463-469.

Olson WH (1978): 'Basic concepts of instrumentation', in Medical instrumentation: application and design, Webster JG (Ed.), Houghton Mifflin Company, Boston.

Oppenheim AV, Schafer RW (1975): 'Digital signal processing', Prentice-Hall Inc., Englewood Cliffs, New Jersey.

Orlov VN (1988): 'Electrocardiography for the practicing physician', Mir Publishers, Moscow.

Perktold K, Florian H, Hilbert D (1987): 'Analysis of pulsatile blood flow: a carotid siphon model', J. Biomed. Eng., 9, 46-53.

Perktold K, Resch M (1990): 'Numerical flow studies in human carotid artery bifurcations: basic discussion of the geometric factor in atherogenesis', J. Biomed. Eng., 12, 111-123.

Peura RA, Webster JG (1978): 'Basic transducers and principles', in Medical instrumentation: application and design', Webster JG (Ed.), Houghton Mifflin Company, Boston.

Prives M, Lisenkov N, Bushkovich V (1985): 'Anatomia Humana III', Editorial Mir, Moscow.

Redwood M (1964): 'Experiments with the electrical analog of a piezoelectric transducer', J. Acoust. Soc. Am., 36, 1872-1880.

Reid JM, Sigelmann RA, Nasser MG, Baker DW (1969): 'Scattering of ultrasound by human blood', in Proc. 8th Int. Conf. Med. Biol. Eng., 10-7.

Rossen JD, Winniford MD (1993): 'Effect of increases in heart rate and arterial pressure on coronary flow reserve in humans', JACC, 21, 343-348.

Sainz A, Roberts VC, Pinardi G (1976): 'Phase-locked loop techniques applied to ultrasonic Doppler signal processing', Ultrasonics, 14, 128-132.

Schlindwein FS, Smith MJ, Evans DH (1988): 'Spectral analysis of Doppler signals and computation of the normalised first moment in real time using a digital signal processor', Med. Biol. Eng. Comput., 26, 228-232.

Segal J, Kern JM, Scott NA, King III SB, Doucette JW, Heuser RR, Ofili E, Siegel R (1992): 'Alterations of phasic coronary artery flow velocity in humans during percutaneous coronary angioplasty', JACC, 20, 276-286.

Shung KK, Sigelmann RA, Reid JM (1976): 'Scattering of ultrasound by blood', IEEE Trans. Biomed. Eng., BME-23, 460-467.

Shung KK, Yuan YW, Fei DY, Tarbell JM (1984): 'Effect of flow disturbance on ultrasonic backscatter from blood', J. Acous. Soc. Am., 75, 1265-1272.

Smedby O (1992): 'Angiographic methods for the study of fluid mechanical factors in atherogenesis', Acta Radiologica, 33, S380, 5-38.

Steingart RM, Scheuer J (1986): 'Assessment of myocardial ischemia', in The heart, Hurst JW Editor-in-chief, McGraw-Hill Inc, New York.

Stone HL; Stegall HF, Bishop VS (1967): 'Continuous measurement of blood flow velocity with an intravascular Doppler flowmeter', Digest of Tech Papers, 7th Int. Conf. Med. Biol. Eng., Stockholm, 215.

Tadaoka S, Kagiyama M, Hiramatsu O, Ogasawara Y, Tsujioka K (1990): 'Accuracy of 20 MHz Doppler catheter coronary artery velocimetry for measurements of coronary blood flow velocity', Cathet. Cardiovasc. Diagn., 19, 205-213.

Taylor MG (1984): 'Processing Doppler-shifted ultrasound signals from insonated blood vessel', University of London, PhD thesis.

Tobis JM, Mahon DJ, Goldberg SL, Nakamura S, Colombo A (1993): 'Lessons from intravascular ultrasonography: observations during interventional angioplasty procedures', J. Clin. Ultrasound, 21, 589-607.

Tortora GJ, Anagnostakos NP (1990): 'Principles of Anatomy and Physiology', Harper & Row, New York.

Vaitkus PJ, Cobbold RSC, Johnston KW (1988): 'A comparative study and Assessment of Doppler Ultrasound Spectral Estimation Techniques - Part II', Ultrasound Med. Biol., 14, 673-688.

Van Alste JA, Schilder TS (1985): 'Removal of base-line wander and power-line interference from the ECG by an efficient FIR filter with a reduced number of taps', IEEE Trans. Biom. Eng., BME-32, 1052-1060.

Violaris AG, Linnemeier TJ, Campbell S, Rothbaum DA, Cumberland DC (1992): 'Intravascular ultrasound imaging combined with coronary angioplasty', Lancet, 339, 1571-1572.

Webster JG (1988): 'Encyclopaedia of medical devices and instrumentation', John Wiley & Sons, New York.

Welch PD (1967): 'The use of fast Fourier transform for the estimation of power spectra: a method based on time averaging over short modified periodograms', IEEE Trans., AU-15, 70-73.

White CW (1993): 'Clinical applications of Doppler coronary flow reserve measurements', Am. J. Cardiology, 71, 10D-16D.

Wilson RF (1991): 'Assessment of the human coronary circulation using a Doppler Catheter', Am. J. Cardiol., 67, 44D-56D.

Wilson RF, Johnson MR, Marcus ML et al. (1988): 'The effect of coronary angioplasty on coronary flow reserve', Circulation, 77, 873-885.

Wilson RF, Marcus ML, White CW (1987): 'Prediction of the physiologic significance of coronary arterial lesions by quantitative lesion geometry in patients with limited coronary artery disease', Circulation, 75, 723-732.

Yamagishi M, Hotta D, Tamai J, Nakatani S, Miyatake K (1991): 'Validity of catheter-tip Doppler techniques in assessment of coronary flow velocity and application of spectrum analysis method', Am. J. Cardiol., 67, 758-762.

Yuan Y, Shung KK (1989): 'Echoicity of whole blood', J. Ultrasound Med., 8, 425-434.